Investigations on carbonaceous materials as electrodes for the next generation electrochemical energy storage device applications

Thesis submitted to

Cochin University of Science and Technology

in partial fulfillment of the requirements

for the award of the degree of

Doctor of Philosophy

By

Manoj M

Reg No: 4308

Department of Physics
Cochin University of Science and Technology
Cochin-682 022, Kerala, India

November 2018

Investigations on carbonaceous materials as electrodes for the next generation electrochemical energy storage device applications

Ph.D. thesis in the field of Material Science

Author

Manoj M
Division for Research in Advanced Materials
Department of Physics
Cochin University of Science and Technology
Cochin-682 022, Kerala, India
E-mail: manojm.ply@gmail.com

Supervising Guide

Dr. S. Jayalekshmi
Emeritus Professor
Division for Research in Advanced Materials
Department of Physics
Cochin University of Science and Technology
Cochin-682 022, Kerala, India
E-mail: jayalekshmi@cusat.ac.in

November 2018

Cover page design: Midhun P Sathyan

DEPARTMENT OF PHYSICS
COCHIN UNIVERSITY OF SCIENCE AND TECHNOLOGY
KOCHI - 682022, INDIA

Dr. S. Jayalekshmi
Emeritus Professor

Certificate

Certified that the thesis entitled **"Investigations on carbonaceous materials as electrodes for the next generation electrochemical energy storage device applications"** submitted by **Mr. Manoj M.** in partial fulfilment of the requirements for the award of degree of Doctor of Philosophy in Physics to Cochin University of Science and Technology, is an authentic and bonafide record of the original research work carried out by him under my supervision at the Department of Physics. Further, the results embodied in this thesis, in full or part, have not been submitted previously for the award of any other degree. All the relevant corrections and modifications suggested by the audience during the pre-synopsis seminar and recommended by the Doctoral committee have been incorporated in the thesis.

Cochin - 22
Date:

Dr. S. Jayalekshmi
(Supervising Guide)

Declaration

I hereby declare that the work presented in the thesis entitled "**Investigations on carbonaceous materials as electrodes for the next generation electrochemical energy storage device applications**" is based on the original research work done by me under the guidance of Dr. S. Jayalekshmi, Emeritus Professor, Department of Physics, Cochin University of Science and Technology, Cochin-22, India and no part has been included in any other thesis submitted previously for the award of any degree.

Cochin - 22
November 2018

Manoj M.

Words of gratitude...

The successful completion of the doctoral thesis would not have been possible without the help and support of many ideal people and words are inadequate to express my sincere cheers to each of them.

At this moment I express my heartfelt gratitude to my supervising guide Dr. S. Jayalekshmi, Emeritus Professor, Department of Physics, CUSAT for her motivation and unparalleled guidance and support throughout my research period. She has been a continuous source of inspiration since my post graduate classes and after the completion of my master's thesis under her guidance she gave me the opportunity to join her research group. Despite being an eminent scientist, her down to earth nature and the genuine affection and caring towards students make her the most loved one around.

I am extremely grateful to Prof. M Junaid Bushiri, Head of the Department of Physics, CUSAT and all former Heads of the Department of Physics for allowing me to access the facilities for carrying out the research work and for their support and co-operation.

I am intensely indebted to Prof. M. K. Jayaraj, Doctoral committee member of the Ph.D. programme, for his co-operation and limitless support. I sincerely extend my gratitude towards Prof. M. R. Anantharaman for his valuable comments during my pre-synopsis presentation and drafting the thesis. I am thankful to my M. Sc. co-ordinator, Prof. Titus K. Mathew and to all other teachers of the Department for their generous help and support. I am also grateful to the office, library and the laboratory staff of the Department of Physics for the co-operation extended all through my research career.

Words fail to express my gratitude towards Dr. Anilkumar. K. M., Assistant Professor, MSM College, Kayamkulam. He inspired me to work in the area of energy storage devices and offered me constant support and advices whenever I faced roadblocks in my research work. His ability to read the situation, quick response to resolve issues and his instrumentation skills are exceptional. Each and every member of my research group has become a beneficiary to his expertise.

I am extremely thankful to Mr. Abhilash. A. and Dr. Pradeep V. S., my own lab mates, for the unparalleled assistance rendered by them in overcoming the

obstacles by providing the most useful instructions and helping in the satisfactory completion of my research work.

I am truly grateful to Miss Jasna M., Research Scholar, OED laboratory of the Physics Department. Most of the results of the research work outlined in this thesis would not have been achieved without her contributions and enormous support. She has been an inevitable part of my research work, by providing research assistantship for almost three years. Her willingness and ready availability to offer help and her helping hand in writing the thesis are worth mentioning.

I express my gratitude towards Dr. Sreekanth Varma, Assistant Professor, SD College, Alappuzha who familiarized me with the synthesis of polymers and to my other lab mates~ Dr. Anand, Jinisha, Joseph John, Dr. Saheeda, Sabira, Renjini, Merin and Soumya.

I would also like to take this opportunity to thank my M.Sc. classmates, senior and junior research scholars for the memorable years that we spent together and making life at CUSAT more enjoyable and unforgettable, especially to Abhilash, Dr. Santhosh, Dr. Deepu, Dr. Navaneeth, Dr. Sajan, Dr. Shijeesh, Rishad, Anshad, Prasad, Jubeesh, Titu, Aravind, Aswathy, Dinto, Sreejith, Rajesh C S, Dr. Rajesh Menon, Geethu, Gincy, Rijeesh, Dr. Tharanath, Dr. Priyesh, Dr. Rajeeshmon, Ashefas, Dr. Jishnu, Dr. Sudheep, Sagar, Hari, Satheesan, Sreeram, Jisha, Jubimol, Abhay, Manu, Kurias, Jerin, Jibin, Nirmal, Jubna, Midhun, Sarath, Frenson and Subin.

The evening sports sessions in the Department of Physics are worth mentioning. The fun filled environment and refreshment have boosted the spirit in me and will be cherished for many years.

Words cannot express the feelings I have for my family for their constant and unconditional love, support and encouragement.

Above all, I thank the Almighty for giving me the strength and patience to work through all these years.

Manoj M.

Preface

Modern civilization is built around the central concept of energy utilization and we have been depending excessively on conventional energy sources to meet the energy demands, for the past many decades. The conventional sources of energy, composed of hydrocarbons are not environmentally benign and are getting depleted at an alarmingly faster rate. As the unappeasable need for energy to meet the daily demands of the modern society is increasing at a startling rate, novel solutions are vital to maintain the current living standards of the society. Recent years have witnessed the generation of energy from renewable and pollution free natural sources such as the sun and the wind. However, the intermittent nature of these natural sources limits their utilization in the preferred way. Through the development of advanced energy storage technologies, the problem of intermittency can be overcome by storing the energy when available and making accessible on demand. The growth of novel energy storage methodologies is of prior importance in the present context of energy consumption.

Among the various types of energy storage devices, batteries and supercapacitors constitute the most promising ones in terms of energy density, power density and cycling stability. Batteries have better energy density suitable for high energy demands, while supercapacitors, on the other hand, can be charged and discharged very quickly providing very high power density. A reliable and efficient energy storage system demands the synchronization of high power and high energy densities. A harmonious integration can bring forth the best features of battery and supercapacitor technologies, revolutionizing the present day energy needs.

Carbonaceous materials have a significant role in the development of sustainable energy storage systems due to their availability in required quantities at affordable prices, the accessibility of established technologies to tune their physical as well as electrochemical properties and their environmentally benign nature. The thesis entitled "**Investigations on carbonaceous materials as electrodes for the next generation**

electrochemical energy storage device applications" is a comprehensive report of the experiments conducted on the development of carbonaceous materials which include, carbon nanostructures like carbon nanotubes and graphene oxide, mesoporous carbon materials and steam activated carbons, as promising electrodes for the next generation lithium ion and lithium–sulfur rechargeable cells and supercapacitors.

The thesis begins with the **"Introduction"** chapter, by reviewing the present situation of global energy consumption and the classification of various energy storage systems and then evolves into portraying the complete outlook of the specific storage systems investigated in the present work. The later sections of the introduction chapter are devoted for discussions about the role of various carbonaceous materials and conducting polymers in the field of energy storage devices. The chapters two to six are highlighted as the core chapters, as they deal with the experimental studies conducted on the various composites of the carbonaceous materials as suitable electrodes for developing rechargeable cells and supercapacitors with desirable performance characteristics.

The **second chapter** highlights the studies conducted on the composite of nanostructured Mn_3O_4 and mesoporous carbon (MC) as a prospective anode material to replace the conventional graphite anode and boost the performance of Li-ion cells. The nanostructured Mn_3O_4, obtained in the form of nanoflakes, using hydrothermal synthesis technique and the commercial product, MC are used to make the Mn_3O_4-MC nanocomposite by physical mixing of the components. This novel and eco-friendly anode configuration is found to improve significantly, the output characteristics of the Li-ion half cells, compared to the conventional ones, using graphite based anodes.

The **third chapter** deals with the studies conducted on the composite of the bio-mass derived, steam activated and acid washed carbon (AC) with sulfur to serve as the modified sulfur cathode (ACS) in rechargeable Li-S cells. The ACS composite, synthesized by solvo-thermal technique and the flexible film of acid functionalized, multi walled carbon nanotubes, termed as the CNTF interlayer, obtained by

solution casting method, form the modified cathode assembly. The pure sulfur cathode is thus modified to overcome its inherent limitations, which mainly include the poor electrical conductivity of sulfur, the adverse effects of the polysulfide shuttling phenomenon and the enormous volume expansion of sulfur during lithium intake. The cathode assembly developed emphasizes the green approach involved in its design. The detailed electrochemical studies highlight the improvement in cell performance in terms of capacity and cycling stability, with key emphasis given to the role of the CNTF interlayer in boosting the cell functioning.

The **fourth chapter** of the thesis portrays the detailed discussion on another modification effected on the sulfur cathode with a view to lift the electrochemical parameters of the assembled Li-S cells more towards commercial standards. The role of highly conducting polyaniline (PANI) coated mesoporous carbon (MC), called as the PMC composite, synthesized by in-situ polymerization method, in effectively overcoming the inherent limitations of the sulfur cathode is assessed. The modified cathode assembly consists of the composite of sulfur with the PMC, termed as the SPMC together with the flexible CNT interlayer. The porous nature of the carbon offers wider pathways for Li ion transport even at higher C rates and thereby brings about commendable improvement in the cell parameters, compared to the previous work, in realizing high performance Li-S cells for the next generation energy storage applications.

A comprehensive overview of polyaniline (PANI)-graphene oxide (GO) based nanocomposite electrodes for developing high performance supercapacitors, forms the prime theme of the work presented in **chapter five**. The role of GO during the in-situ polymerization for the synthesis of the PANI-GO composite and the structural and the electrochemical characterization studies carried out on the composite are described. The device level performance of the hybrid supercapacitor is evaluated by carrying out electrochemical studies on the assembled supercapacitor test cells.

The practical realization of the Li-ion full cells with the pre-lithiated Mn_3O_4-MC composite as the anode and $LiFePO_4$, synthesized using sol-gel technique as the cathode, forms the focal theme of **chapter six**. The possibility of developing this unique full cell configuration as a cost-effective, eco-friendly and reliable Li-ion technology is detailed in this chapter.

In the **last chapter**, which forms the concluding chapter of the thesis, the work presented in the thesis is summarized and the conclusions drawn from the present investigations are highlighted. The current relevance of the present work in the design of the next generation energy storage systems with desired performance characteristics is emphasized and the future research prospects are envisioned. The next mission is to optimize the key parameters of electrode material synthesis to achieve the required structural features to realize Li-ion full cells, meeting commercial standards, using the eco-friendly electrode materials developed in the present work and to accomplish the development of the next generation Li-S full cells using suitable anode materials.

Contents

List of Tables

List of Figures

List of Publications

Publications related to the work presented in the thesis

Journal publications

1. Biomass-derived, activated carbon-sulfur composite cathode with a bifunctional interlayer of functionalized carbon nanotubes for lithium-sulfur cells, **M. Manoj**, C. Muhamed Ashraf, M. Jasna, K. M. Anilkumar, B. Jinisha, V. S .Pradeep, S. Jayalekshmi, *Journal of Colloid and Interface Science* 535 (2019), 287-299.
2. Sulfur-polyaniline coated mesoporous carbon composite in combination with carbon nanotubes interlayer as a superior cathode assembly for high capacity lithium-sulfur cells, **M. Manoj**, M. Jasna, K. M. Anilkumar, A. Abhilash, B. Jinisha, V. S. Pradeep, S. Jayalekshmi, *Applied Surface Science* 458 (2018), 751–761.
3. Polyaniline–Graphene Oxide based ordered nanocomposite electrodes for high-performance supercapacitor applications, **M. Manoj**, K. M. Anilkumar, B. Jinisha, S. Jayalekshmi, *J Mater Sci: Mater Electron* 28 (2017), 14323.

Other publications to which author has contributed

1. Layered sulfur/PEDOT:PSS nano composite electrodes for lithium sulfur cell applications, K. M. Anilkumar, B. Jinisha, **M. Manoj,** V. S. Pradeep, S. Jayalekshmi *Applied Surface Science* 442 (2018), 556–564.
2. Acid Washed, Steam Activated, Coconut Shell Derived Carbon for High Power Supercapacitor Applications C. Muhamed Ashraf, K. M. Anilkumar, B. Jinisha, **M. Manoj**, V. S. Pradeep and S. Jayalekshmi, *Journal of The Electrochemical Society*, 165 (2018), A900-A909.
3. Poly (ethylene oxide) (PEO)-based, sodium ion-conducting, solid polymer electrolyte films, dispersed with Al_2O_3 filler, for applications in sodium ion cells, B. Jinisha, K. M. Anilkumar, **M. Manoj**, n S. Jayalekshmi. *Ionics* 24 (2018), 1675-1683.

4. Lithium-enriched polypyrrole as a prospective cathode material for Li-ion cells, Joseph John, **M. Manoj**, K. M. Anilkumar, V. S. Pradeep, S. Jayalekshmi, *Ionics* 24 (2018), 2565-2574.

5. Mn_3O_4/reduced graphene oxide nanocomposite electrodes with tailored morphology for high power supercapacitor applications, K. M. Anilkumar, **M. Manoj**, B. Jinisha, V. S. Pradeep, S. Jayalekshmi, *Electrochimica Acta* 236 (2017), 424–433.

6. Development of a novel type of solid polymer electrolyte for solid state lithium battery applications based on lithium enriched poly (ethylene oxide) (PEO)/poly (vinyl pyrrolidone) (PVP) blend polymer, B. Jinisha, K. M. Anilkumar, **M**. **Manoj**, V. S. Pradeep, S. Jayalekshmi**,** *Electrochimica Acta* 235 (2017), 210–222.

7. Transparent flexible lithium ion conducting solid polymer electrolyte. Anand B. Puthirath, Sudeshna Patra, Shubhadeep Pal, **M. Manoj**., Aravind Puthirath Balan, S. Jayalekshmi, Narayanan Tharangattu N, *J. Mater. Chem. A* 5 (2017), 11152.

8. Poly (ethylene oxide) (PEO) – Poly (vinyl pyrrolidone) (PVP) blend polymer based solid electrolyte membranes for developing solid state magnesium ion cells, K. M. Anilkumar, B. Jinisha, **M. Manoj**, S. Jayalekshmi, *European Polymer Journal* 89 (2017), 249–262.

Conference presentations

1. On the structural and electrical properties of Polyaniline-graphene nanocomposite films, **M. Manoj**, S. Jayalekshmi, 2nd International Conference on Advanced Functional Materials (ICAFM 2014), Trivandrum, India.

2. Polyaniline graphene oxide composite electrode materials for supercapacitor applications, **M. Manoj**, K. M. Anilkumar, B. Jinisha, S. Jayalekshmi, National conference on Carbon Materials (NCCM 2015) Conducted by NPL, New Delhi, India.

3. Polyaniline zinc oxide composite electrode materials for supercapacitor applications, **M. Manoj**, K. M. Anilkumar, B. Jinisha, S. Jayalekshmi, 28th Kerala Science Congress, Calicut University Campus, Thenhippalam.

4. Polyaniline coated CNT-Sulfur composite as cathode material for lithium-sulfur batteries, International Conference on Advances in Functional Materials, **M. Manoj**, V. S. Pradeep, K. M. Anilkumar, B. Jinisha, S. Jayalekshmi, ICAFM-2017, January, 6-8, 2017, Anna University, Chennai, India.

5. PANI/MWCNT composite electrode for supercapacitor applications, M. Jasna., **M. Manoj**, S. Jayalekshmi, M. K. Jayaraj, Proc. SPIE 10725, 2018, 107250Q.

6. Activated carbon-sulfur composite with PEDOT:PSS-CNT interlayer as cathode material for lithium-sulfur batteries, **M. Manoj**, M. Jasna, S. Jayalekshmi, Proc. SPIE 10725, 2018, 1072511.

7. Flexible Solid Electrolyte Sheets for Lithium ion cells, K. M. Anil Kumar, B. Jinisha, **M. Manoj**, S. Jayalekshmi, International conference on energy harvesting storage and conversion (ICEEE-2015), Cochin University of Science & Technology (CUSAT). Kochi, India.

8. Will Mg-ion cells serve as substitute for Li-ion cells? K. M. Anil Kumar, B. Jinisha, **M. Manoj**, S. Jayalekshmi, International conference on Contemporary Advances of Science & Technology (IC-CAST 2015), Banaras Hindu University, Varanasi, India

9. Lithium enriched solid polymer blend electrolytes based on poly (vinyl pyrrolidone) using different lithium salts for energy storage applications, B. Jinisha, K. M. Anil Kumar, **M. Manoj**, S. Jayalekshmi, International Conference on Materials for the Millennium (MATCON 2016), Cochin University of Science and Technology, Kerala, India.

10. Polyethylene oxide (PEO) / polyvinyl alcohol (PVA) complexed with lithium perchlorate ($LiClO_4$) as a prospective material for making solid polymer electrolyte films, B. Jinisha, K. M. Anil Kumar, **M. Manoj**, S. Jayalekshmi, International Conference on Smart Engineering Materials ICSEM-2016, RV college of Engineering, Bangalore, India.

1

Introduction

The first chapter of the Ph.D. thesis deals with the fundamental aspects of the research work carried out with emphasis on the motivation behind the present line of investigations. The objectives of the studies are also specifically defined. The brief description of the various carbonaceous materials investigated to assess their suitability as the electrode materials for energy storage device applications also forms a prime session of this chapter.

1.1 Motivation

About eighty-six percentage of the current global energy comes from burning of fossil fuels and the rest is the contribution from hydroelectric and nuclear plants and the renewable energy sources. The burning of fossil fuels and the resultant emission of greenhouse gases badly affect the atmosphere by altering the chemistry of air and oceans. An estimated quantity of 150 billion tons of carbon dioxide has already been pumped into the atmosphere since 1750 and around 9.9 billion tons of it, recently in 2016 alone. Around 6 million people die each year as a result of air pollution which is higher than the mortality due to alcohol abuse and drug abuse combined. Scientists have established that with the greenhouse gases trapped in the atmosphere the earth is getting warmer

and as a result, the ice caps are melting and sea levels are rising, giving the warnings of possible mass extinctions.[1–4] A schematic representation of the present-day fuel consumption is shown in figure 1.1.

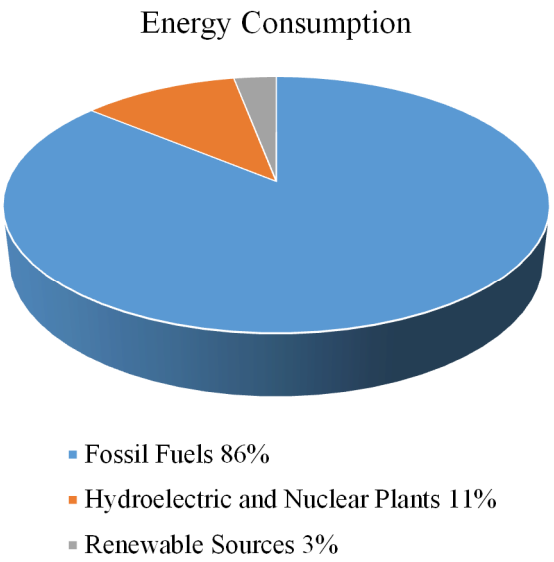

Figure 1.1. Schematic representation of fuel consumption.

The global energy demand has already escalated in tune with the continuous population growth and it is not feasible to depend solely on fossil fuels to meet the energy requirements, considering the major environmental threats generated. Also, the conventional energy sources will soon be totally exhausted as the population increases at an alarmingly faster rate.[5,6] Recent studies reveal that oil fields have already reached their peak output limits and now started declining at the rate of 6% per year.[7] The energy reserves of coal, gas, and oil are illustrated in figure 1.2.

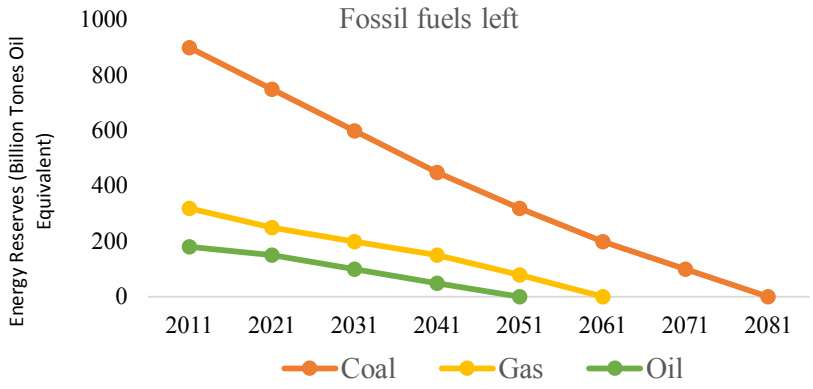

Figure 1.2. Remaining reserves of coal, gas and oil.

1.2 The future is bright

It is high time one should focus on renewable energy sources to meet the growing energy demands and preserve the mother earth for future generations. The good news is that around the world, during the past decade, renewable energy use has increased to a significant extent. In 2016, world has consumed three times more wind energy than in 2010 and ten times more solar energy and almost two-thirds of the net power capacity around the world has come from renewable energy.[1] It is assumed that by 2022, renewable electricity capacity should increase by 43%. India is also in the forefront in renewable energy production. The ministry of new and renewable energy (MNRE), Government of India, plans to target a totally renewable energy capacity of 175 GW by 2022 from 3 GW in 2016.[8,9] India has the fourth largest installed wind power capacity of 32.17 GW and also has quadrupled its solar power generation capacity from 2650 MW in 2014 to 12,298 MW by 2017.[10] Along with the numerous advantages of renewable energy sources, one has to be aware of their limitations as well. These energy sources mainly

consisting of solar and wind power sources do not generate power on the same large scale as fossil fuels do. Also, these renewable sources are intermittent and the solar panels and wind turbines can generate power only when the sun is shining and the wind is blowing.

1.3 Emerging needs of energy storage systems (ESS)

The unpredictable and intermittent nature of renewable energy sources makes them unreliable and variable. In order to facilitate the growth of renewable sources effectively and to cut-down the gap between supply and demand, the energy generated needs to be stored. Energy storage systems (ESS) are ideal to overcome the challenges posed by renewable energy sources and they play a crucial role by storing the excess energy and releasing it back to the grid on demand and thereby maintaining a constant power supply.[11,12]

Thus, ESS help in

- Attenuating the discrepancy of renewable energy sources
- Maintaining the delicate balance between supply and demand
- Reducing the cost of power and maintaining its quality.

1.4 Classification of ESS

Energy storage systems can be generally classified based on the response time and storage durations. The most widely used approach for categorization of various ESS is based on the form of energy stored in the system[13,14] and is shown in figure 1.3.

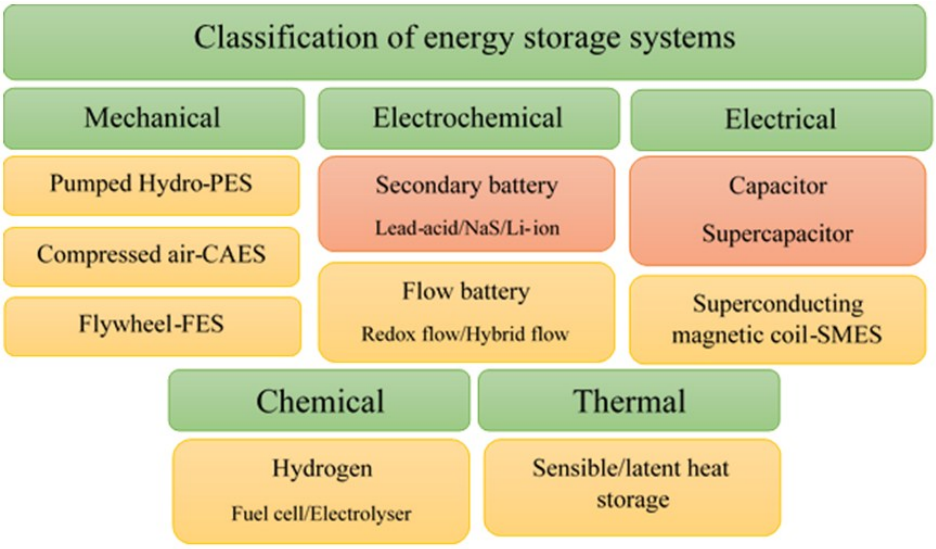

Figure 1.3. Classification of energy storage systems.

Among the various energy storage systems listed above, batteries and supercapacitors are the most frequently and widely used systems.[15–17] Batteries transform chemical energy via redox reactions at the cathode and anode to electrical energy. In supercapacitors, energy storage occurs either by ion adsorption (electrochemical double layer capacitor) at the electrode-electrolyte interface or by redox reactions (pseudo-capacitor).[18] Batteries are more widely used due to their high energy density while supercapacitors with high power density can be charged and discharged very quickly. Batteries can be broadly classified into primary and secondary batteries. A primary battery (non-rechargeable) is a disposable type of battery. Secondary batteries are rechargeable and can be charged over and again after use. Alkaline batteries, mercury batteries, and zinc-carbon batteries are examples of primary batteries and lead-acid and lithium batteries belong to the secondary batteries.[19] The lithium-ion

battery (Li-ion) commercialized by Sony corporation in 1991 is the most advanced rechargeable battery. These batteries have revolutionized the portable electronics industry and form the powerhouse of electronic revolution with high energy density and power density. Many of the cellphones and laptops are powered by Li-ion batteries as they are smaller, cheaper and more efficient.[20,21] The table 1.1 given below shows the performance comparison between supercapacitor and Li-ion battery.[22]

Table 1.1. Performance comparison between supercapacitor and Li-ion battery

Function	Supercapacitor	Battery (Li-ion)
Charging time	1-10 seconds	10-60 minutes
Cycle life	30000 hours	500 hours or higher
Cell Voltage	2.3 to 2.75 V	3.6 V
Specific energy (Wh kg^{-1})	5	120-240
Specific power (W kg^{-1})	10000	1000-3000
Cost per kWh	$10000	$250-$1000
Service life	10-15 years	5-10 years
Charge temperature	-40 to 65℃	0 to 45℃
Discharge temperature	-40 to 65℃	-20 to 60℃

1.5 Battery terms and definitions

The international union of pure and applied chemistry (IUPAC) has coined a set of terms to represent various aspects of electrochemical technology as shown in table 1.2.

Table 1.2. Battery terminology

Active material	The material in the electrode of a cell which involves in electrochemical reactions during charging and discharging.
C-rate	C-rate is the rate at which a cell is discharged relative to its maximum capacity. The rate 1 C means that the cell will transfer all of its stored energy in 1 hour.
Capacity	The electrical charge stored in a cell which is available for transfer during discharge, expressed in ampere-hours (Ah) or milliampere-hours (mA h).
Coulombic efficiency	The ratio of energy output on discharging to the energy input upon charging of a cell and is expressed in %.
Charge retention	The capacity retained by the cell after the completion of charge-discharge process.
Cycle	A single charge-discharge sequence of a cell.
Cycle life	The maximum number of cycles a cell can perform before its capacity falls significantly.
Energy density	It is the measure of energy available from a cell. Energy density can be measured gravimetrically, expressed in watt-hour per kilogram (Wh kg^{-1}) or volumetrically, expressed in watt-hour per liter (Wh L^{-1}).
Impedance	Impedance refers to the resistance offered by a cell to the flow of an alternating current (AC). It includes DC resistance as well as capacitance and inductance.
Internal resistance	The resistance exhibited by a cell to the flow of direct current (DC) and is the sum of ionic and electronic resistances of the cell components.
Open circuit voltage	The voltage measured between the cell terminals when no load is connected.
Power density	The ratio of power available from a cell to its mass is the gravimetric power density (W kg^{-1}) and to its volume is the volumetric power density (W L^{-1}).
Self-discharge	The loss of useful capacity of a cell due to internal chemical action. Self-discharge is highly dependent on temperature.

1.6 Lithium-ion battery (Li-ion)

Similar to any other battery, rechargeable Li-ion battery holds power generating units called cells. Each Li-ion cell consists of a positive electrode (cathode), a negative electrode (anode) and the electrolyte in between them. The two electrodes are isolated by a porous membrane named separator which prevents electric contact between the electrodes and at the same time promotes the movement of ions from anode and cathode during charging and discharging. Conventionally, graphite has been the central source of anode material in Li-ion cells. The cathode materials are usually oxides of transition metals. The layered oxide $LiCoO_2$ is the most widely used cathode material in Li-ion cells. Other promising cathode materials include $LiNiO_2$, $LiMn_2O_4$, and $LiFePO_4$.[22] The crystal structures of different cathode materials employed in Li-ion cells are shown in figure 1.4. The electrolyte in Li-ion cells consists of lithium salts and $LiPF_6$ is considered as a most suitable electrolyte.[23]

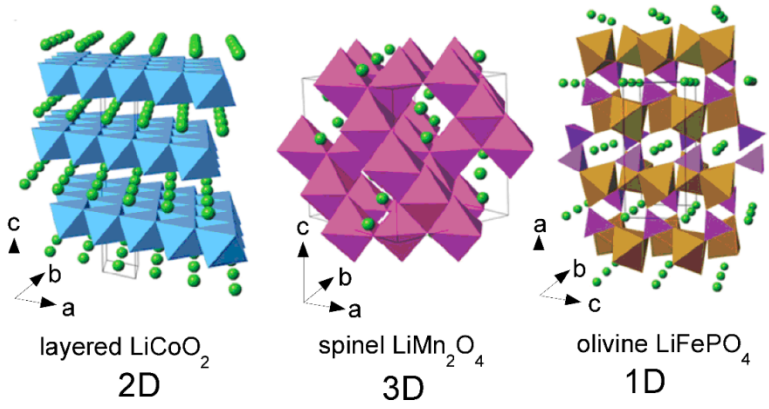

Figure 1.4. Crystal structures of various cathode materials for Li-ion cells.

1.6.1 Working of Li-ion cells

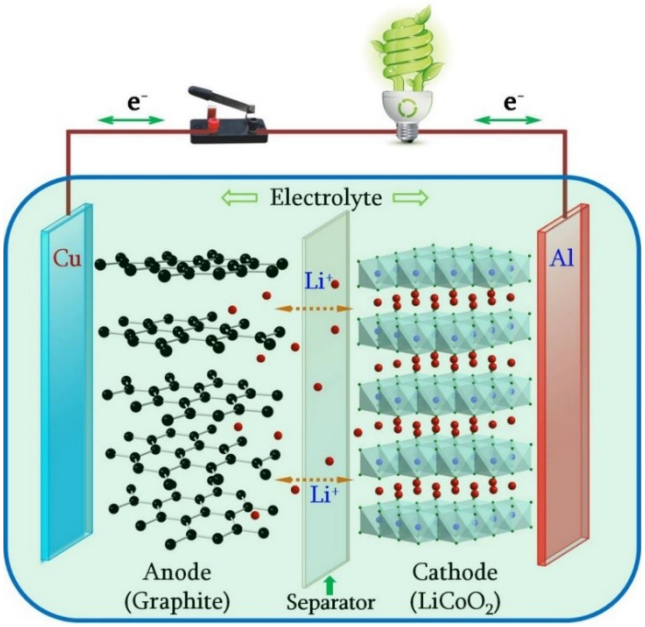

Figure 1.5. Schematic representation of working of Li-ion cell.

The working principle of Li-ion cell is displayed in figure 1.5. These cells operate based on the interlacation of lithium ions into the electrode materials. During the charging process of the cell, termed as the intercalation, the positively charged lithium ions pass from the cathode ($LiCoO_2$) through the porous separator into the layered structure of the anode (Graphite). When the cell is discharged, or during the deintercalation, the lithium-ions travel from the anode through the separator back to the cathode. The capacity, energy density and power density of the Li-ion cells are determined by the nature of the electrode materials used.[24–26] The charging and discharging process of Li-ion cell can be expressed as equation (1)-(4).

During charging,

Cathode: $LiCoO_2 \rightarrow Li^+ + e^- + CoO_2$ (1)

Anode: $C_6 + Li^+ + e^- \rightarrow LiC_6$ (2)

During discharging,

Cathode: $Li^+ + e^- + CoO_2 \rightarrow LiCoO_2$ (3)

Anode: $LiC_6 \rightarrow C_6 + Li^+ + e^-$ (4)

1.6.2 Anode materials for Li-ion cells

In practical Li-ion full cells, carbonaceous materials, oxides and alloys are used as anodes, instead of lithium metal, due to safety concerns. Coke was used as the anode material by SONY during the intial phase of commercialization of lithium-ion cells and later mesophase microbeads of carbon became more popular.[27] Graphite continues to be the leading anode material in Li-ion cells due to its benefits of low working potential, low-cost, availability of material and eco-friendly nature. Graphite anode offers a theoretical capacity of 372 mA h g^{-1} and provides excellent cycling stability.[28] But it fails to satisfy the energy demands of emerging applications in electronic industry as the theoretical capacity is quite low. The immediate need is to develop high energy density and low-cost electrode materials to serve as anodes for Li-ion cells to meet the challenging requirements. Based on the reaction mechanisms of intercalation, conversion and alloying, the anode materials of Li-ion cells can be broadly classified into three different categories. As mentioned earlier, for the anode materials involved in interlacation reaction mechanism, the Li ions are intercalated into the layered structure of the anode. The theoretical energy density is typically low as the lithium ions can only be intercalated topotatctically

into the d-spacing lattices of the anode. The intercalation reaction mechanism does not cause any volume change to the anode. Conversion reaction mechanism occurs in anode materials made from transition metal oxides. The anode materials like Fe_3O_4, Mn_3O_4, and NiO undergo reversible oxidation/reduction process in the presence of Li ions. Anode materials undergoing conversion reaction mechanism display relatively high energy density and specific capacity compared to conventional graphite anode. Anodes made from alloy materials such as Si, Sn, Ge and Al undergo alloying reaction during electrochemical process and the Li ions inserted during lithiation form compound phases. The alloy anode materials are well known for their extremely high capacities, compared to the other two groups of anodes. The poor electrical conductivity and huge volume expansion occurring at the time of lithiation process limit their application prospects in Li-ion cells. A comparative study of various anode materials is given in the table 1.3 below.[29–31]

Table 1.3. A comparative study of various anode materials

Reaction mechanism	**Anode materials**	**Specific capacity (mA h g^{-1})**
Insertion	C	372
	$Li_4Ti_5O_{12}$	175
Conversion	Fe_3O_4	924
	Co_3O_4	890
	FeO	744
Alloying	Si	4200
	Ge	1600
	Sn	994

1.7 Lithium-Sulfur cells (Li-S)

Although Li-ion cells dominate the portable electronic industry, their competence fails for applications involving electric vehicles and smart utility grids which demand much higher energy density and power density. This has necessitated the exploration of new materials and novel electrochemical approaches to go beyond the horizon of Li-ion cells to solve the energy crisis and the environmental issues.[32]

The Li-S cell concept is widely recognized as the next generation energy storage approach among the various emerging battery technologies. The theoretical specific energy density of Li-S cells is almost five times greater than that of traditional Li-ion cells. Moreover, the active cathode material- sulfur, used in Li-S cell is also non-toxic, cheap and abundant in nature. Sulfur offers a high theoretical capacity of 1672 mA h g^{-1} and theoretical specific energy density of 2500 Wh kg^{-1}.[33,34] The high capacity is based on the conversion reaction of elemental sulfur to lithium sulfide, Li_2S. Li-S cell allows higher lithium storage capacity as each sulfur atom can host two lithium ions. Typical Li-ion cells accommodate only 0.5-0.7 lithium ions per host atom. Sulfur is the fifth richest element on earth and forms polyatomic molecules with different structures and the most stable allotrope at room temperature is octasulfur, cyclo-S_8. The above features make Li-S cell technology a particularly efficient and low-cost energy storage approach. Comparison of the volumetric and gravimetric energy density of Li-ion and Li-S cells is shown below in figure 1.6.[35]

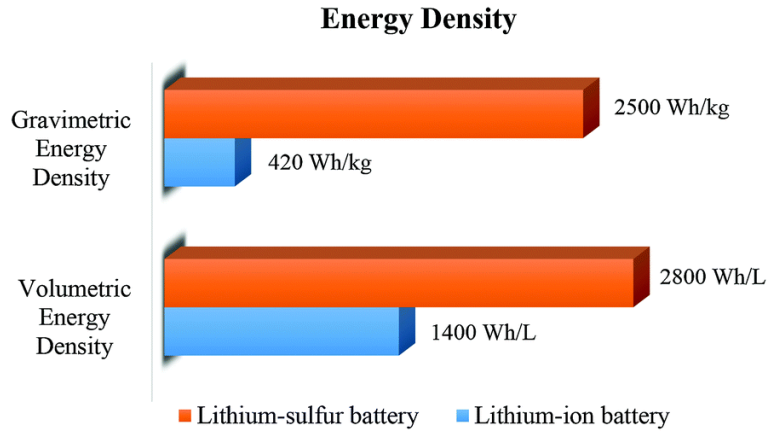

Figure 1.6. Energy density profiles of Li-ion cells and Li-S cells.

1.7.1 Electrochemistry of Li-S cells

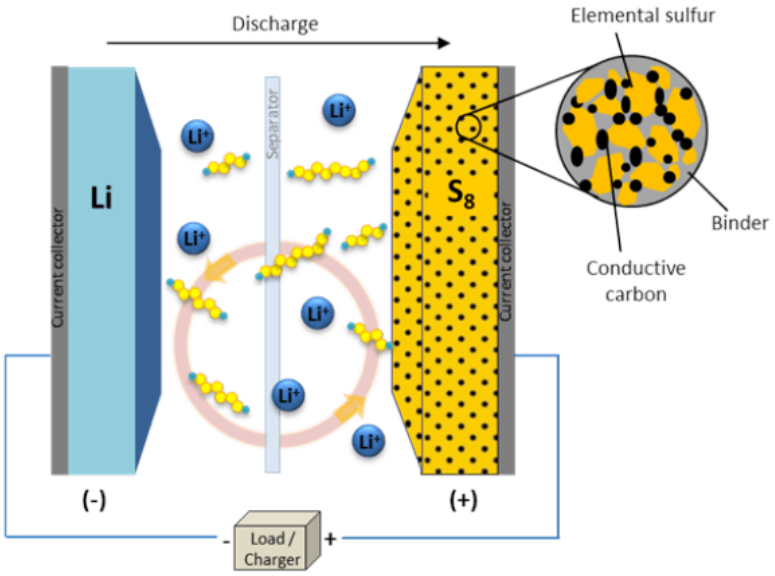

Figure 1.7. Schematic representation of working of Li-S cell.

Li-S cell (figure.1.7) consists of a lithium metal as anode, sulfur composite as cathode and an organic electrolyte. The anode and cathode are physically separated using a separator membrane which permits the

movement of ions. The energy storage mechanism in Li-S cell is entirely different from that of conventional Li-ion cells. During the charge-discharge process, sulfur composite cathode undergoes a series of structural changes leading to the formation of intermediate polysulfides. The anode lithium (negative electrode) gets oxidized to form lithium ions and electrons during the discharge process. The lithium ions move through the electrolyte while the electrons travel through the external circuit to reach the sulfur composite cathode (positive electrode). At the cathode, sulfur reacts with the lithium ions and electrons resulting in the formation of different polysulfides such as Li_2S_8, Li_2S_6, Li_2S_4, Li_2S_2 and finally Li_2S, at the end of the discharge process.[36,37] The conversion reaction of the sulfur cathode during discharge is detailed below.[32] The redox reaction in the Li-S cell can be expressed as equations (5)-(9).

$$S_8 + 2Li^+ + 2e^- \rightarrow Li_2S_8 \quad (5)$$

$$3Li_2S_8 + 2Li^+ + 2e^- \rightarrow 4Li_2S_6 \quad (6)$$

$$2Li_2S_6 + 2Li^+ + 2e^- \rightarrow 3Li_2S_4 \quad (7)$$

$$Li_2S_4 + 2Li^+ + 2e^- \rightarrow 2Li_2S_2 \quad (8)$$

$$Li_2S_2 + 2Li^+ + 2e^- \rightarrow 2Li_2S \quad (9)$$

During the charging process, opposite reaction occurs and Li_2S is converted back to S_8, although the intermediate polysulfide species might be different.

The overall cell reaction can be expressed as equation (10),

$$16Li^+ + S_8 \leftrightarrow 8Li_2S \quad (10)$$

The charge-discharge voltage profile of Li-S cell is shown in figure 1.8.[35]

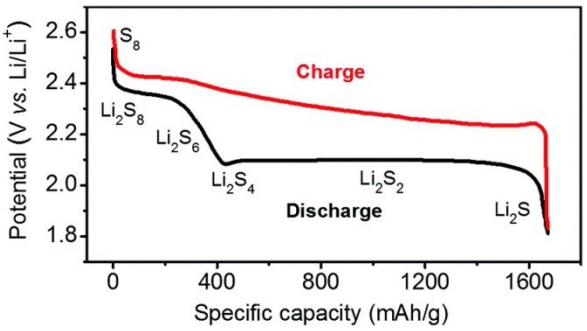

Figure 1.8. Charge-discharge voltage profile of a Li-S cell.

1.7.2 Electrolytes for Li-S cells

The electrolyte plays a crucial role in determining the cycling stability of Li-S cells. Liquid electrolytes are usually used in Li-S cells which act as Li-ion transport pathways between anode and cathode. As the higher order polysulfides can dissolve in the electrolyte and ultimately leads to polysulfide shuttling phenomenon, the selection of electrolyte for Li-S cells is critical. Presently, lithium salts such as LiTFSI, $LiCF_3SO_3$, $LiClO_4$ in combination of solvents including 1,3-dioxolane (DOL), 1,2-dimethoxyethane (DME), tetrahydrofuran (THF) and tetra ethylene glycol dimethyl ether (TEGDME) are widely used as electrolytes in Li-S cells.[38] Also, lithium nitrate is often used as an electrolyte additive to passivate the lithium anode and to achieve improved cell performance.[39] The reduction of intermediate polysulfide species at the lithium anode surface can be effectively reduced by the passivation layer and consequently achieve high charge/discharge efficiency.

1.7.3 Challenges of Li-S cells

Despite the Li-S technology being a high energy density and low-cost battery technology, there are many key issues that hinder its practical implementation. The foremost challenge is to overcome the low electrical conductivity (10^{-30} S cm^{-1}) of sulfur followed by handling the intermediate polysulfides formed during the charge-discharge cycling. The insulating nature of sulfur retards electron transfer and ion transport, resulting in poor utilization of the sulfur cathode. Another prominent challenge for Li-S cells is the unwanted reactions of intermediate polysulfides with the electrolyte. While S and Li_2S are relatively insoluble in most electrolytes the higher order lithium polysulfides Li_2S_x ($4 \leq x \leq 8$) dissolve in the electrolyte, diffuse to the anode and get reduced chemically to lower order polysulfides, migrate back to the cathode, form higher order polysulfides again and so on. This migration of polysulfides between the anode and cathode, known as the "polysulfide shuttle effect" leads to (i) a continuous loss of active cathode material resulting in poor cycling life (ii) self-discharge behavior and (iii) low Coulombic efficiency. The large volume expansion of sulfur during electrochemical conversion between sulfur and Li_2S is another concern of Li-S cells. The sulfur cathode undergoes a volume expansion of about 80% upon full lithiation of sulfur.[35–37]

Immense efforts have been proposed to overcome the above issues and improve the electrochemical performance of the sulfur cathode in Li-S cells. Encapsulation of sulfur with conductive host materials like carbonaceous materials and conducting polymers helps in enhancing the electrical conductivity of the sulfur cathode. As the porous polymeric separator cannot halt the polysulfide migration to the

anode, the introduction of multi-functional separators helps in realizing Li-S cells with high rate performance and long cycle life.[40] The modified separator suppresses the shuttle effect and protects the lithium metal anode from the dendrite growth. Various polymers with ion selective properties, carbon materials and oxide materials have been extensively used to modify the separator for enhanced battery performance. A novel Li-S cell configuration by inserting a bi-functional interlayer of carbon nanotubes between the separator and the cathode material has been suggested to improve the electrochemical performance of Li-S cells. The interlayer ensures better utilization of sulfur and impedes the polysulfide shuttle phenomenon by localizing the migrating polysulfides within the cathode region. The interlayer also significantly reduces the internal charge transfer resistance at the cathode interface to achieve high specific capacity, prolonged cycle life, and high Coulombic efficiency without the need of any elaborate synthesis technique and complex surface modification of sulfur cathode.[40,41] Interlayers based on biomass derived materials[42,43], conducting polymers[44] and metal foils[45] have also been proposed.

1.8 Supercapacitors

Supercapacitor, as the name implies differs from a regular capacitor since it provides high capacitance in a small package. Supercapacitors can offer high power delivery and also can be charged and discharged quickly and have long cycle life than conventional batteries.[46,47] They can complement batteries in energy storage applications such as hybrid vehicles and electric utilities. The plot of power density against energy density, called Ragone plot, for different energy storage devices is shown in figure 1.9 and supercapacitors fill the gap between dielectric capacitors and batteries.[48]

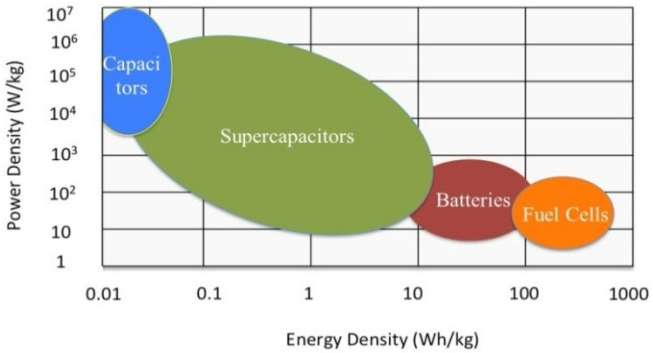

Figure 1.9. Ragone plot for various energy storage devices.

Depending upon the active electrode materials used and the charge storage mechanisms involved supercapacitors can be classified into electrochemical double layer capacitors, pseudo-capacitors and hybrid capacitors [49] as shown in figure 1.10.

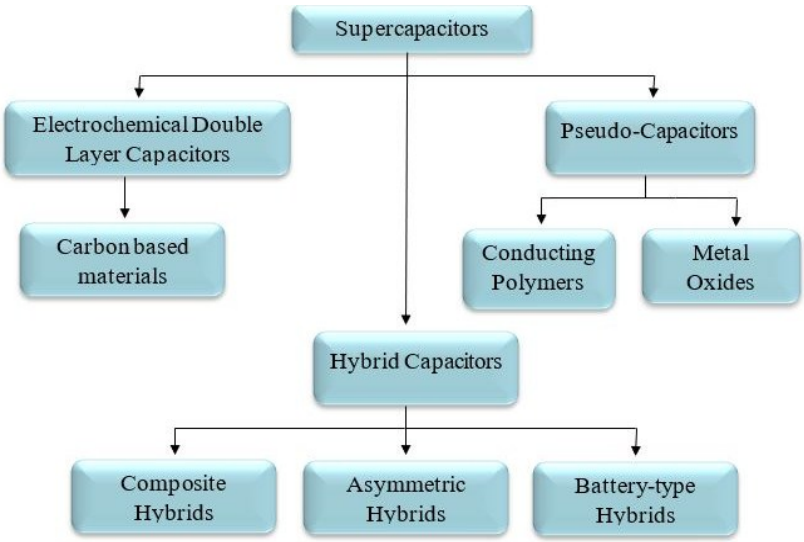

Figure 1.10. Classification of supercapacitors.

1.8.1 Electrochemical double capacitors (EDLC)

In electrochemical double layer capacitors (EDLC), the energy storage process is via reversible ion adsorption at the electrode-electrolyte

interface[49] as shown in figure 1.11. Since no chemical reaction or charge transfer occurs across the electrode, a non-faradic process is involved in charge storage mechanism. During charging, the applied voltage creates an electric field between the electrodes and the electrically charged ions in the electrolyte migrate towards the opposite polarity electrodes creating two separate charged layers having a thickness of only a few molecular diameters. Materials with large surface area and high porosity are quite important to gain high capacitance as they can hold the migrating ions. The two factors, large electrode surface area and minimal thickness of double layer provide supercapacitors with high capacitance and energy density than conventional capacitors. The large surface area of electrodes in EDLC supercapacitors provides them with high current delivering capability which inturn gives extremely high power density of a few orders higher than that can be attained with batteries.[50,51] Carbon materials are considered as potential electrode materials in EDLC capacitors owing to their numerous advantages, including easy availability, low cost, non-toxic nature, easy processing techniques, good electronic conductivity and large surface area for charge storage.[52]

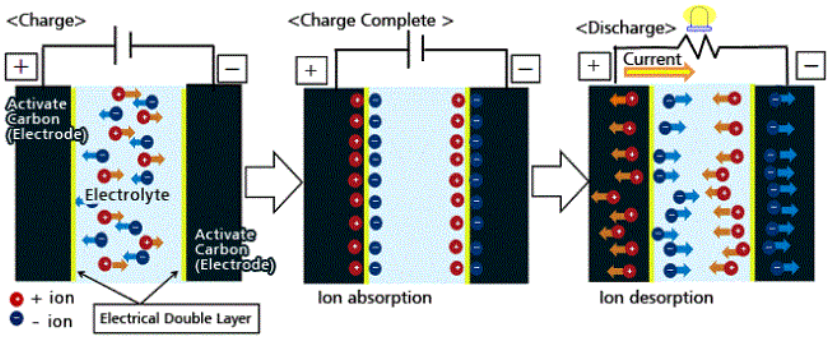

Figure 1.11. Working of EDLC supercapacitor.

If E_A and E_B represent two electrode surfaces, A^- an anion, C^+ a cation and the electrode-electrolyte interface is represented as ‖, the non-faradic process for charging and discharging can be expressed as equation (11)-(14).[53]

At the positive electrode,

$$\text{During charging: } E_A + A^- \rightarrow E_A^+ \| A^- + e^- \quad (11)$$

$$\text{During discharging: } E_A^+ \| A^- + e^- \rightarrow E_A + A^- \quad (12)$$

At the negative electrode,

$$\text{During charging: } E_B + C^+ + e^- \rightarrow E_B^- \| C^+ \quad (13)$$

$$\text{During discharging: } E_B^- \| C^+ \rightarrow E_B + C^+ + e^- \quad (14)$$

Overall charging and discharging process can be expressed as equation (15) and (16):

$$\text{During charging: } E_A + A^- + E_B + C^+ \rightarrow E_A^+ \| A^- + E_B^- \| C^+ \quad (15)$$

$$\text{During discharging: } E_A^+ \| A^- + E_B^- \| C^+ \rightarrow E_A + A^- + E_B + C^+ \quad (16)$$

From the figure the entire capacitor cell can be considered as two capacitors connected in series. If C_A and C_B represent the capacitance of the two electrodes, the overall capacitance C_T can be expressed as equation (17).

$$\frac{1}{C_T} = \frac{1}{C_A} + \frac{1}{C_B} \quad (17)$$

If both the electrodes have the same capacitance, $C_A = C_B$, the total capcitance would be half of either one's capacitance and the supercapacitor is termed as symmertic supercapacitor and if $C_A \neq C_B$ and both electrodes offer different capacitance values, the supercapacitor is termed as asymmertic supercapacitor.

Upon charging, a voltage V will develop across the electrodes and the energy density and power density can be expressed as equation (18) and (19)

$$E = {}^{1}/_{2}\, CV^2 \tag{18}$$

$$P = {}^{V^2}/_{4R_S} \tag{19}$$

where R_S is the equivalent series resistance of the supercapacitor.

The specific capacitance C_S, a generally used term for a supercapacitor cell can be expressed as equation (20),

$$C_S(F\, g^{-1}) = {}^{C}/_{m} \tag{20}$$

The specific capacitance of a single electrode in a supercapacitor cell can be expressed as equation (21),

$$C_S = {}^{4C}/_{m} \tag{21}$$

where C stands for the total capacitance of the cell, and m is the total mass of the active materials in both the electrodes combined.[54]

1.8.2 Pseudo-capacitors

In pseudo-capacitors, the charge storage mechanism is different from that of EDLC. Here, when a voltage is applied, reversible faradic (oxidation and reduction) reactions take place on the active electrode materials similar to those occuring in batteries and electron charge transfer occurs between the electrode and the electrolyte.[48] But unlike in batteries, the charging and discharging processes occur on the orders of seconds and minutes in pseudocapacitive materials. Metal oxides such as

RuO_2, Fe_3O_4, MnO_2 and conducting polymers undergo redox reactions and are used as electrode materials in pseudo-capacitors. They offer higher specific capacitance and energy density than EDLC due to the faradic reaction mechanism. However, pseudo-capacitors exhibit relatively lower power density than EDLC as the faradic process is normally slower than non-faradic process and also suffer from lack of cycling stability similar to batteries because of the redox reactions occurring at the electrode.[55,56]

1.8.3 Hybrid capacitors

Hybrid capacitor, as the name implies has an asymmetrical electrode configuration, like a combination of a carbon electrode and a pseudo-capacitive electrode material. In a hybrid capacitor, both faradic and non-faradic reaction mechanisms occur simultaneously, and one of them displays a dominant role.[57]

The major setback of supercapacitors compared to batteries is their insufficient energy density. As the energy density is given by $E = {}^{1}/_{2}\, CV^2$, by increasing either or both the capacitance and cell voltage, the energy density can be enhanced. Higher capacitance can be achieved by developing novel carbon materials with higher surface area for EDLC and transition metal oxides and conducting polymers for pseudo-capacitors. As the energy density is proportional to the square of cell volatge, increasing cell volatge would be more effective for the improvement of energy density. The cell voltage can be enhanced by widening the volatge window of the electrolyte solution used in supercapacitors. Thus the proper choice of electrolyte is of prime importance in determining the performance of any type of supercapacitor.

Beyond having wider voltage window, the electrolyte used in supercapacitors should have requirements such as high purity, high electrochemical stability, low resistivity, low viscosity, and low toxicity.[58]

Mainly three different types of electrolytes are used in supercapacitors, namely (i) aqueous electrolytes (ii) organic electrolyte and (iii) ionic liquids.[53] Supercapacitors using aqueous electrolytes deliver higher capacitance and power density as the ionic concentration is higher and the aqueous electrolytes have high conductivity. The main drawback of aqueous electrolytes is the very small voltage window of about 1.2 V, which makes them a low choice among various electrolytes, since the small voltage window is a huge constraint in improving the energy density of supercapacitors. The most regularly used aqueous electrolytes include H_2SO_4, KOH, and Na_2SO_4. Organic electrolytes provide typically higher voltage window in the range 2.5 to 2.8 V compared to aqueous electrolytes and thus dominate the supercapacitor market. The most commonly used solvents in organic electrolytes are acetonitrile and propylene carbonate. Compared to aqueous electrolytes, organic electrolytes have lower conductivity, lower specific capacitance and they suffer from enviromental issues and safety concerns. An ionic liquid is a salt in the liquid state with melting point below 100 ℃. They posses unique properties such as wide voltage window in the range 2 to 6 V and high thermal and chemical stability which make them promising alternatives for supercapacitor electrolytes.

1.9 Conducting polymers for advanced energy storage systems

1.9.1 Rise of conducting polymers

Polymers are giant and complex molecules with molecular weight as high as several hundred thousand. It is the size of the polymer that gives it unique properties different from those of low molecular weight compounds. A polymer is made up of many small molecules which combine to form a single large molecule. The individual small molecules from which the polymer is formed are known as monomers and the process to form a big polymer molecule is called polymerization. The size of the polymer chain is determined by the number of monomer units present in it and this number denotes the degree of polymerization.[59]

The evolution of conducting polymers (CPs), also known as "Synthetic Metals" began in 1977, with the discovery of insulating polyacetylene (PA) becoming conducting when doped with iodine.[60] This breakthrough was exemplified when the Nobel prize in chemistry for the year 2000 was awarded to Alan J. Heeger, Alan G. MacDiarmid and Hideki Shirakawa "for the discovery and development of conductive polymers".[61] Conducting polymers hold a significant position in the field of materials science because of their tunable electrical and optical properties and reversible doping-de-doping procedure. They are endowed with an overlap of delocalized π-electrons along the polymer chain. Typical conductive polymers include polyacetylene (PA), polyaniline (PANI), polypyrrole (PPY), poly(3,4-ethylene dioxythiophene) (PEDOT) and poly(p-phenylenevinylene) (PPV).[62] They find profound applications in field effect transistors, sensors, light emitting diodes and solar cells.

They are extensively used as electrode materials for energy storage devices owing to their high electrical conductivity, tunable electrical properties and excellent thermal and environmental stability. Among the various conducting polymers, polyaniline (PANI) has gained extensive attention because of the availability of simple synthesis routes, high electrical conductivity and thermal stability, and environmental friendliness.[63] Polyaniline and its composites with carbon materials and metal compounds have shown great potential in energy storage and conversion applications.[64]

1.10 Carbonaceous materials for energy storage device applications

1.10.1 Carbon-The essence of everything

Carbon-the sixth element of the periodic table, is one of the most abundant elements in earth's crust and the second most abundant element in the human body by mass. Carbon is the basic building material of life for all living systems and life cannot exist without this element. It is more than the builder of life. Human civilization is built on carbon as its different forms have been the source of energy for humans for thousands of years.[65,66]

Carbon is known to exist in three different forms as diamond, graphite and amorphous carbon. These carbon allotropes take different chemical structures and exhibit different properties depending on how the atoms are bonded. Diamond is the hardest naturally occurring material known. In diamond, each carbon atom is linked to four other carbon atoms through covalent bonds. As the valence electrons are not free to move, it is a poor electrical conductor compared to other carbons like

amorphous carbon or graphite. Graphite is the softest form of carbon with each carbon atom linked to only three other carbon atoms to form sheets of carbon atoms, making it a good conductor of electricity.[67]

With the Nobel prize winning discovery of buckminsterfullerene C60 in 1985[68,69] and the subsequent discovery of new forms of carbon ranging from 0 D to 3 D such as the carbon nanotubes in 1991[70] and graphene in 2004[71], opened up a new era in materials science and nanotechnology. Graphene is a one-atom-thick planar sheet of carbon atoms, densely packed together into a honeycomb shaped crystal lattice. The cylindrical nanostructures are known as carbon nanotubes and the hollow sphere form presents a fullerene.[72] The different carbon nanostructures are illustrated in figure 1.15.

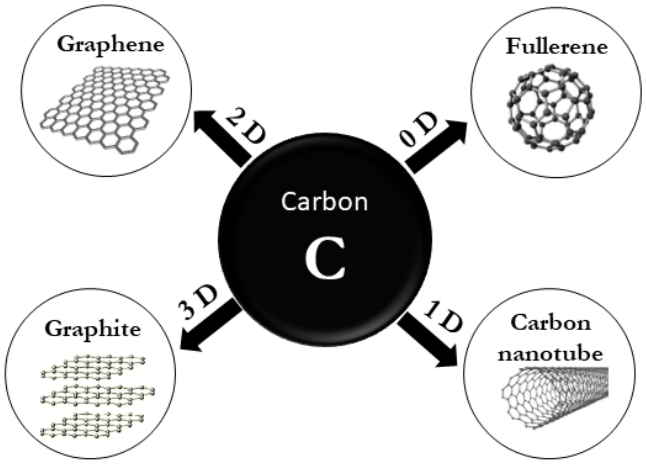

Figure 1.15. Overview of different carbon materials.

"Carbon has this genius of making a chemically stable, two-dimensional, one-atom-thick membrane in a three-dimensional world. And that, I believe, is going to be very important in the future of chemistry and technology in general." writes Nobel laureate Richard Smalley.[73]

Carbon materials are considered as prospective electrodes in novel energy storage devices due to their tunable surface properties and well-established, cost effective production technologies. Their electrochemical performance mainly depends on the electrical conductivity, specific surface area, surface functionality and pore-size distribution.[74,75] The carbon materials investigated in the present work for various energy storage device applications include activated carbon, mesoporous carbon, carbon nanotubes and graphene oxide.

1.10.2 Activated Carbon

Activated carbons are perhaps the most explored class of active materials for applications as electrodes in various energy storage devices due to their high surface area, excellent chemical and thermal stability, low-cost and availability in large quantities.[51,76] They are derived by thermal decomposition of carbon-rich organic precursors like wood, rice husk, watermelon and coconut shells under an inert atmosphere, a procedure known as carbonization.[65,77–80] The resulting carbon materials are subjected to activation process to gain control over the physical structure and surface chemistry.[81] Carbonization leads to the formation of amorphous carbon, while the activation process increases the surface area of the carbon material and results in pore formation.[82]

The carbon materials can be activated using either physical methods or chemical methods.[83] Physical activation is done under an oxidizing atmosphere of air, oxygen, carbon dioxide or steam at high temperature.[48] Studies reveal that the pore volume and surface area of carbon materials activated by physical methods are very much dependent on the time and temperature of activation and the gas flow

rate.[84] The above methods of activation yield activated carbons with moderate to high porosity, as well as with varying surface chemistry. The higher the activation temperature and activation time, the larger the pores developed.[85,86] In contrast, the chemical activation is carried out by mixing carbon materials with chemicals like KOH, NaOH and K_2CO_3,followed by pyrolysis in an inert atmosphere at temperatures of 450–900 °C.[82] Concerns about environmental issues limit the use of chemicals for activation.[87] As mentioned earlier, the activation process results in the formation of pores in the carbon materials with high specific surface area (SSA). According to IUPAC the porous materials are classified based on the pore size, as microporous with pore size less than 2 nm, mesoporous, with pore size in the range of 2-50 nm and macroporous, having pores with size greater than 50 nm.[88] The SSA of activated carbon materials typically comes in the range of 1000-2000 $m^2 g^{-1}$.[51]

1.10.3 Mesoporous Carbon

Ordered mesoporous carbon materials with high surface area are of interest in energy storage applications due to their high-power rating capability with little capacity fading. The different synthesis routes of mesoporous carbon include activation of carbon precursors using metal-containing species as catalyst, carbonization of organic aerogels or cryogels and carbonization of precursors composed of one thermosetting component and one thermally unstable component.[89,90] The mesoporous carbon synthesized employing the above procedures generally has a broad pore size distribution including a lot of micropores. The template assisted route of synthesis makes it possible to get control over the pore size and pore size distribution and has gained more attention.[91] The power capability of the electrode based on mesoporous carbon can be tuned

through ion mobility and even at high current densities mesopores can maintain capacitance as they provide wider paths that facilitate ion transport.

1.10.4 Graphene oxide

The ease of processability together with their excellent electrical and thermal properties make graphene-based materials, highly promising candidates for applications in energy generation and storage, optical devices, sensors, electronic and photonic devices and as transparent electrodes.[92] The presence of oxygen functional groups like epoxy and hydroxyl on the basal plane and smaller amounts of carboxyl and carbonyl groups at the sheet edges are recognized as the major functionalities attached on graphene oxide (GO).[93] The mechanical and electrochemical properties of GO are strongly affected by the presence of oxygenated groups in GO and this accounts for the major difference between pristine graphene and GO. The oxygen functional groups of GO are responsible for its strong hydrophilic nature and provide good dispersibility in many solvents, especially, water.[94]

It is generally synthesized by the oxidation of natural graphite powder and the well-known methods are Brodie method, Staudenmaier method, Hofmann method and Hummers method and their modified forms.[95] All the methods involve the chemical treatment of natural graphite powder with acids like H_2SO_4, HCl and HNO_3, followed by the breaking of graphitic layers into small pieces by the intercalation of alkali metal compounds like $KClO_3$ and $KMnO_4$.[95]

1.10.5 Carbon nanotubes

Carbon nanotubes (CNTs) are widely used in the electrode fabrication for rechargeable batteries and supercapacitors due to their meritorious characteristics of high electrical conductivity, unique structural features, fast charge transport and high tensile strength.[96,97] They are categorized into single-walled nanotubes (SWNTs) and multi-walled nanotubes (MWNTs).[98] The former ones are composed of individual graphene sheets rolled to form hollow cylinders with a tube diameter of 0.4-2 nm. The MWNTs consist of multiple rolled layers of graphene with interlayer distance of approximately 0.36 nm with diameter in the range of 2-100 nm.[99] Due to the multi layered sidewalls, MWNTs show excellent electrical conductivity and ultrafast ion transport.[100,101] Chemical vapor deposition, arc-discharge and laser ablation techniques are usually employed for the generation of CNTs.[102] Despite the numerous merits of CNTs, their pristine form usually contains impurities including amorphous carbon and catalyst nanoparticles. The hydrophobic nature of CNTs makes them insoluble in water and it is not easy to disperse them in aqueous media in their pristine form.[103,104] To overcome these practical limitations of CNTs, they need to be purified and the most commonly used methods involve oxidative acid treatment, in a concentrated H_2SO_4/HNO_3 mixture, for the removal of residual metal catalyst impurities. The acid purification increases their dispersion and also reduces their toxic effects.[105,106] The acid functionalization technique leads to the opening of tube caps and the formation of holes at sidewalls, resulting in the generation of CNTs with tips and sidewalls decorated with oxygenated functionalities and modified surface features.[107,108]

1.11 Objectives of the present investigations

The Ph.D. work is focused on assessing the prospective applications of various carbonaceous materials namely activated carbon, mesoporous carbon, graphene oxide and carbon nanotubes in the design and development of the next generation energy storage systems constituted by Li-ion cells, Li-S cells and supercapacitors. The prime objectives of the research work can be highlighted as follows:

- Assess the suitability of the novel and eco-friendly, nanostructured Mn_3O_4-mesoporous carbon (MC) composite as the anode material in Li-ion cells to improve the electrochemical performance and thereby overcome the limitations of conventional graphitic anode.
- Rectify the inherent limitations of the Li-S cell technology by using the composite of sulfur with the bio-mass derived, steam activated and acid washed carbon (AC) as the cathode, supported by the interlayer of functionalized carbon nanotubes.
- Develop Li-S cells of high discharge capacity, admirable cycling stability and high Coulombic efficiency by effecting surface modification of the sulfur cathode using polyaniline coated mesoporous carbon and employing the flexible interlayer of carbon nanotubes between the sulfur cathode and the separator.
- Evaluate the suitability of polyaniline (PANI)-graphene oxide (GO) based nanocomposite electrodes for developing supercapacitors with excellent performance characteristics.

- Realize Li-ion full cells with the pre-lithiated Mn_3O_4-MC composite as the anode and $LiFePO_4$ as the cathode and develop this eco-friendly full cell configuration into viable and practical Li-ion cell technology, meeting commercial standards.

References

[1] Quick, M. How will we source clean energy for all?, 2017 http://www.bbc.com/future/story/20170711-how-will-we-source-clean-energy-for-all.

[2] Dudley, B. *BP Statistical Review of World Energy 67th Edition*; 2018.

[3] TEAM, G. E. Harmful Effects of Non-Renewable Resources on the Environment https://greentumble.com/harmful-effects-of-non-renewable-resources-on-the-environment/.

[4] WHO. *An Estimated 12.6 Million Deaths Each Year Are Attributable to Unhealthy Environments*; 2016.

[5] Murray, J.; King, D. Oil's Tipping Point Has Passed. *Nature* **2012**, *481*, 433.

[6] Stratfor. When Renewables Replace Fossil Fuels https://worldview. stratfor.com/ article/when-renewables-replace-fossil-fuels.

[7] Agency, C. intelligence. The world factbook https://www.cia.gov/ library/publications/the-world-factbook/geos/xx.html.

[8] MNRE. The Government Is Promoting Development of Solar Energy in the Country by Providing Various Fiscal and Promotional Incentives. 2018.

[9] IBEF. *Renewable Energy*; 2018.

[10] India's Solar Power Capacity Crosses 12 GW. *The economic times*. 2017.

[11] Dunn, B.; Kamath, H.; Tarascon, J. Electrical Energy Storage for the Grid : A Battery of Choices. *Mater. grid energy* **2011**, *334*, 928.

[12] Chen, H.; Ngoc, T.; Yang, W.; Tan, C.; Li, Y. Progress in Electrical Energy Storage System : A Critical Review. *Prog. Nat. Sci.* **2009**, *19*, 291.

[13] Luo, X.; Wang, J.; Dooner, M.; Clarke, J. Overview of Current Development in Electrical Energy Storage Technologies and the Application Potential in Power System Operation. *Appl. Energy* **2015**, *137*, 511.

[14] Smith, S. C.; Sen, P. K.; Ieee, S. M.; Kroposki, B.; Ieee, S. M. Advancement of Energy Storage Devices and Applications in Electrical Power System. *IEEE* **2008**.

[15] Dubal, D. P.; Ayyad, O.; Ruiz, V. Hybrid Energy Storage: The Merging of Battery and Supercapacitor Chemistries. *Chem. Soc. Rev.* **2015**, *44*, 1777.

[16] Yang, S. Q. Towards Superior Volumetric Performance : Design and Preparation of Novel Carbon Materials for Energy Storage. *Energy Environ. Sci.* **2015**, *8*, 1390.

[17] Xu, G.; Nie, P.; Dou, H.; Ding, B.; Li, L.; Zhang, X. Exploring Metal Organic Frameworks for Energy Storage in Batteries and Supercapacitors. *Mater. Today* **2017**, *20*, 191.

[18] Martin Winter, R. J. B. What Are Batteries, Fuel Cells, and Supercapacitors ? *Chem. Rev.* **2004**, *104*, 4245.

[19] Linden, D. *Handbook of Batteries and Fuel Cells*; New York, McGraw-Hill Book Co., 1984.

[20] Tarascon, J. M.; Armand, M. Issues and Challenges Facing Rechargeable Lithium Batteries. *Nature* **2001**, *414*, 359.

[21] Armand, M.; Tarascon, J.-M. Building Better Batteries. *Nature* **2008**, *451*, 652.

[22] How does a Supercapacitor Work? https://batteryuniversity.com/learn/article/whats_the_role_of_the_supercapacitor.

[23] Xu, K. Nonaqueous Liquid Electrolytes for Lithium-Based Rechargeable Batteries. *Chem. Rev.* **2004**, *104*, 4303.

[24] Liu, C.; Neale, Z. G.; Cao, G. Understanding Electrochemical Potentials of Cathode Materials in Rechargeable Batteries. *Mater. Today* **2016**, *19*, 109.

[25] Balogun, M.; Qiu, W.; Luo, Y.; Meng, H.; Mai, W.; Onasanya, A. A Review of the Development of Full Cell Lithium-Ion Batteries : The Impact of Nanostructured Anode Materials. *Nano Res.* **2016**, *9*, 2823.

[26] Goodenough, J. B.; Park, K.-S. The Li-Ion Rechargeable Battery: A Perspective. *J. Am. Chem. Soc.* **2013**, *135*, 1167.

[27] Li, B. H.; Wang, Z.; Chen, L.; Huang, X. Research on Advanced Materials for Li-Ion Batteries. *Adv. Mater.* **2009**, *21*, 4593.

[28] Cao, K.; Jin, T.; Jiao, L. Recent Progress in Conversion Reaction Metal Oxide Anodes for Li-Ion Batteries. *Mater. Chem. Front.* **2017**, *1*, 2213.

[29] Xu, Z. L.; Liu, X.; Luo, Y.; Zhou, L.; Kim, J. K. Nanosilicon Anodes for High Performance Rechargeable Batteries. *Prog. Mater. Sci.* **2017**, *90*, 1.

[30] Yoo, H. D.; Markevich, E.; Salitra, G.; Sharon, D.; Aurbach, D. On the Challenge of Developing Advanced Technologies for Electrochemical Energy Storage and Conversion. *Mater. Today* **2014**, *17*, 110.

[31] Nitta, N.; Wu, F.; Lee, J. T.; Yushin, G. Li-Ion Battery Materials : Present and Future. *Mater. Today* **2015**, *18*, 252.

[32] Wang, J.; Xie, K.; Wei, B. Advanced Engineering of Nanostructured Carbons for Lithium – Sulfur Batteries. *Nano Energy* **2015**, *15*, 738.

[33] Chen, L.; Shaw, L. L. Recent Advances in Lithium- Sulfur Batteries. *J. Power Sources* **2014**, *267*, 770.

[34] Bruce, P. G.; Freunberger, S. A.; Hardwick, L. J.; Tarascon, J.-M. Li–O_2 and Li–S Batteries with High Energy Storage. *Nat. Mater.* **2011**, *11*, 172.

[35] Seh, Z. W.; Sun, Y.; Zhang, Q.; Cui, Y. Designing High-Energy Lithium–sulfur Batteries. *Chem. Soc. Rev.* **2016**, *45*, 5605.

[36] Manthiram, A.; Fu, Y.; Chung, S.; Zu, C.; Su, Y. Rechargeable Lithium − Sulfur Batteries. *Chem. Rev.* **2014**, *114*, 11751.

[37] Manthiram, A.; Fu, Y.; Su, Y.-S. Challenges and Prospects of Lithium–Sulfur Batteries. *Acc. Chem. Res.* **2013**, *46*, 1125.

[38] Yuan Yang, G. Z. and Y. C. Nanostructured Sulfur Cathodes. *Chem. Soc. Rev.* **2013**, *42*, 3018.

[39] Liang, X.; Wen, Z.; Liu, Y.; Wu, M.; Jin, J.; Zhang, H.; Wu, X. Improved Cycling Performances of Lithium Sulfur Batteries with $LiNO_3$ -Modified Electrolyte. *J. Power Sources* **2011**, *196*, 9839.

[40] Huang, J. Q.; Zhang, Q.; Wei, F. Multi-Functional Separator/Interlayer System for High-Stable Lithium-Sulfur Batteries: Progress and Prospects. *Energy Storage Mater.* **2015**, *1*, 127.

[41] Carbone, L.; Greenbaum, G.; Hassoun, J. Lithium Sulfur and Lithium Oxygen Batteries : New Frontiers of Sustainable Energy Storage. *Sustain. Energy Fuels* **2017**, *1*, 228.

[42] Gu, X.; Lai, C.; Liu, F.; Yang, W. A Conductive Interwoven Bamboo Carbon Fi Ber Membrane for Li–S Batteries †. *J. Mater. Chem. A* **2015**, *3*, 9502.

[43] Chung, S.; Manthiram, A. Carbonized Eggshell Membrane as a Natural Polysulfide Reservoir for Highly Reversible Li-S Batteries. *Adv. Mater.* **2014**, *26*, 1360.

[44] Wang, A.; Xu, G.; Ding, B.; Chang, Z.; Wang, Y.; Dou, H.; Zhang, X. Highly Conductive and Lightweight Composite Film as Polysulfide Reservoir for High-Performance Lithium – Sulfur Batteries. *ChemElectroChem* **2017**, *4*, 362.

[45] Zhang, K.; Qin, F.; Fang, J.; Li, Q. Nickel Foam as Interlayer to Improve the Performance of Lithium – Sulfur Battery. *J. solid state Electrochem.* **2014**, *18*, 1025.

[46] Kandalkar, S. G.; Dhawale, D. S.; Kim, C.; Lokhande, C. D. Chemical Synthesis of Cobalt Oxide Thin Film Electrode for Supercapacitor Application. *Synth. Met.* **2010**, *160*, 1299.

[47] Largeot, C.; Portet, C.; Chmiola, J.; Taberna, P.; Gogotsi, Y.; Simon, P. Relation between the Ion Size and Pore Size for an Electric Double-Layer Capacitor. *J. Am. Chem. Soc* **2008**, *130*, 2730.

[48] Simon, P.; Gogotsi, Y. Materials for Electrochemical Capacitors. *Nat. Mater.* **2008**, *7*, 845.

[49] Hadjipaschalis, I.; Poullikkas, A.; Efthimiou, V. Overview of Current and Future Energy Storage Technologies for Electric Power Applications. *Renew. Sustain. Energy Rev.* **2009**, *13*, 1513.

[50] Huang, J.; Sumpter, B. G.; Meunier, V. Theoretical Model for Nanoporous Carbon Supercapacitors **. *Angew. Chemie Int. Ed.* **2008**, *47*, 520.

[51] Simon, P.; Burke, A. Nanostructured Carbons: Double-Layer Capacitance and More. *Electrochem. Soc. Interface* **2008**, *17*, 38.

[52] Iro, Z. S.; Subramani, C.; Dash, S. S. A Brief Review on Electrode Materials for Supercapacitor. *Int. J. Electrochem. Sci.* **2016**, *11*, 10628.

[53] Wang, G.; Zhang, J. A Review of Electrode Materials for Electrochemical Supercapacitors. *Chem Soc Rev* **2012**, *41*, 797.

[54] Chen, T.; Dai, L. Carbon Nanomaterials for High- Performance Supercapacitors. *Mater. Today* **2013**, *16*, 272.

[55] Augustyn, V.; Dunn, B. Pseudocapacitive Oxide Materials for High-Rate Electrochemical Energy Storage. *Energy Environ. Sci.* **2014**, *7*, 1597.

[56] Yu, X.; Yun, S.; Yeon, J. S.; Bhattacharya, P.; Wang, L.; Lee, S. W.; Hu, X.; Park, H. S. Emergent Pseudocapacitance of 2D Nanomaterials. *Adv. energy Mater.* **2018**, *1702930*, 1.

[57] Burke, A. R & D Considerations for the Performance and Application of Electrochemical Capacitors. *Electrochim. Acta* **2007**, *53*, 1083.

[58] Zhong, C.; Deng, Y.; Hu, W.; Qiao, J.; Zhang, L.; Zhang, J. A Review of Electrolyte Materials and Compositions for Electrochemical Supercapacitors. *Chem. Soc. Rev.* **2015**, *44*, 7484.

[59] Dinesan, A. A. S. and M. K. Review : Polyaniline-A novel polymeric material. *Talanta* **1991**, *38*, 815.

[60] Hideki Shirakawa, Edwin J. Louis, Alan G. MacDiarmid, C. K. C. and A. J. H. Synthesis of Electrically Conducting Organic Polymers: Halogen Derivatives of Polyacetylene, (CH)X. *J. Chem. Soc. Chem. Commun.* **1977**, 578.

[61] Letheby, H. On the Production of a Blue Substance by the Electrolysis of Sulphate of Aniline. *J. Chem. Soc. 15*, 161.

[62] Huang, W.; Humphrey, B. D.; Macdiarmid, A. G. Polyaniline , a Novel Conducting Polymer Morphology and Chemistry of Its Oxidation and Reduction in Aqueous Electrolytes. *J. Chem. Soc. Faraday Trans. 1 Phys. Chem. Condens. Phases* **1986**, *82*, 2385.

[63] G. MacDiarmid, J.-C. 'Polyaniline': Protonic Acid Doping of the Emeraldine Form to the Metallic Regime. *Synth. Met.* **1986**, *13*, 193.

[64] Wang, H.; Lin, J.; Xiang, Z. Polyaniline (PANi) Based Electrode Materials for Energy Storage and Conversion. *J. Sci. Adv. Mater. Devices* **2016**, *1*, 225.

[65] Candelaria, S. L.; Shao, Y.; Zhou, W.; Li, X.; Xiao, J.; Zhang, J.; Wang, Y.; Liu, J.; Li, J.; Cao, G. Nanostructured Carbon for Energy Storage and Conversion. *Nano Energy* **2012**, *1*, 195.

[66] Roston, E. The Carbon Age: How Life's Core Element Has Become Civilization's Greatest Threat. In *The Carbon Age: How Life's Core Element Has Become Civilization's Greatest Threat*; Walker & Company; pp 1–26.

[67] B.Rand, A.J.Hosty, S. W. Introduction to Carbon Science. In *Introduction to Carbon Science*; Elsevier, 1989; pp 75–106.

[68] The Nobel Prize in Chemistry 1996 The Royal Swedish Academy of Sciences. **1996**.

[69] C60: Buckminsterfullerene. *Nature* **1985**, *318*, 162.

[70] Sumio Iijima. Helical Microtubules of Graphitic Carbon. *Nature* **1991**, *354*, 56.

[71] K. S. Novoselov, A. K. Geim, S. V. Morozov, D. Jiang, Y. Zhang, S. V. Dubonos, I. V. Grigorieva, A. A. F. Electric Field Effect in Atomically Thin Carbon Films. *Science (80-.).* **2004**, *306*, 666.

[72] Gogotsi, Y. and V. P. *Carbon Nanomaterials*; CRC Press, 2013.

[73] Zhang, L. Photofunctional Layered Materials; Springer; pp 213–238.

[74] Bo, Z.; Wen, Z.; Kim, H.; Lu, G.; Yu, K.; Chen, J. One-Step Fabrication and Capacitive Behavior of Electrochemical Double Layer Capacitor Electrodes Using Vertically-Oriented Graphene Directly Grown on Metal. *Carbon N. Y.* **2012**, *50*, 4379.

[75] Karandikar, P. B.; Tiwari, N. K. Effect of Electrode Shape on the Parameters of Supercapacitor. *IEEE* **2015**, 669.

[76] Zhang, L. L.; Zhao, X. S. Carbon-Based Materials as Supercapacitor Electrodes. *Chem. Soc. Rev.* **2009**, *38*, 2520.

[77] Banerjee, K.; Ramesh, S. T.; Gandhimathi, R.; Nidheesh, P. V; Bharathi, K. S. A Novel Agricultural Waste Adsorbent , Watermelon Shell for the Removal of Copper from Aqueous Solutions. *Iran. J. Energy Environ.* **2012**, *3*, 143.

[78] A. Ayguun, S. Yenisoy-Karakas, I. D. Production of Granular Activated Carbon from Fruit Stones and Nutshells and Evaluation of Their Physical , Chemical and Adsorption Properties. *Microporous Mesoporous Mater.* **2003**, *66*, 189.

[79] Yang, J.; Qiu, K. Preparation of Activated Carbons from Walnut Shells via Vacuum Chemical Activation and Their Application for Methylene Blue Removal. *Chem. Eng. J.* **2010**, *165*, 209.

[80] Yang, K.; Peng, J.; Srinivasakannan, C.; Zhang, L.; Xia, H.; Duan, X. Preparation of High Surface Area Activated Carbon from Coconut Shells Using Microwave Heating. *Bioresour. Technol.* **2010**, *101*, 6163.

[81] A. Ahamdpour, and D. D. Do. The Preparation of Active Carbons from Coal by Chemical and Physical Activation. *Carbon N. Y.* **1996**, *34*, 471.

[82] Jie Wang, Ping Nie, Bing Ding, Shengyang Dong, Xiaodong Hao, H. D. and X. Z. Biomass Derived Carbon for Energy Storage Devices. *J. Mater. Chem. A* **2017**, *5*, 2411.

[83] Kazehaya, A.; Muroyama, K.; Watkinson, A. P. Preparation of Activated Carbon from Lignin by Chemical Activation. *Carbon N. Y.* **2000**, *38*, 1873.

[84] Yang, K.; Peng, J.; Xia, H.; Zhang, L.; Srinivasakannan, C.; Guo, S. Textural Characteristics of Activated Carbon by Single Step CO_2 Activation from Coconut Shells. *J. Taiwan Inst. Chem. Eng.* **2010**, *41*, 367.

[85] Mohd, W.; Wan, A.; Shabuddin, W.; Ali, W.; Sulaiman, M. Z. Effect of Activation Temperature on Pore Development in Activated Carbon Produced from Palm Shell. *J. Chem. Technol. Biotechnol.* **2003**, *5*, 1.

[86] Khanh, N.; Quach, N.; Yang, W.; Chung, Z.; Tran, H. L. The Influence of the Activation Temperature on the Structural Properties of the Activated Carbon Xerogels and Their Electrochemical Performance. *Adv. Mater. Sci. Eng.* **2017**, *2017*, 8308612.

[87] Tadda, M. A.; Ahsan, A.; Shitu, A.; Elsergany, M. A Review on Activated Carbon : Process , Application and Prospects. *J. Adv. Civ. Eng. Pract. Res.* **2016**, *2*, 7.

[88] Borislav D. Zdravkov, JirıJ. Cermak, Martin Sefara, J. J. Pore Classification in the Characterization of Porous Materials : A Perspective. *Cent. Eur. J. Chem.* **2007**, *5*, 385.

[89] Eftekhari, A.; Fan, Z. Ordered Mesoporous Carbon and Its Applications for Electrochemical Energy Storage and Conversion. *Mater. Chem. Front.* **2017**, *1*, 1001.

[90] Ajayan, S.; Ramadass, K.; Singh, G.; Scaranto, J.; Ravon, U. Recent Advances in Functionalized Micro and Mesoporous Carbon Materials : Synthesis and Applications. *Chem. Soc. Rev.* **2018**, *47*, 2680.

[91] Liang, C.; Li, Z.; Dai, S. Mesoporous Carbon Materials : Synthesis and Modification. *Angew. Chemie* **2008**, *47*, 3696.

[92] Chen, D.; Feng, H.; Li, J. Graphene Oxide : Preparation , Functionalization, and Electrochemical Applications. *Chem. Rev.* **2012**, *112*, 6027.

[93] Dreyer, D. R.; Park, S.; Bielawski, W.; Ruoff, R. S. The Chemistry of Graphene Oxide. *Chem Soc Rev* **2010**, *39*, 228.

[94] Sharma, D.; Kanchi, S.; Sabela, M. I.; Bisetty, K. Insight into the Biosensing of Graphene Oxide : Present and Future Prospects. *Arab. J. Chem.* **2016**, *9*, 238.

[95] Singh, R. K.; Kumar, R.; Singh, D. P. Graphene Oxide: Strategies for Synthesis, Reduction and Frontier Applications. *RSC Adv.* **2016**, *6*, 64993.

[96] Notarianni, M.; Liu, J.; Vernon, K.; Motta, N. Synthesis and Applications of Carbon Nanomaterials for Energy Generation and Storage. *J. Nanotechnol.* **2016**, *7*, 149.

[97] Sun, L.; Wang, X.; Wang, Y.; Zhang, Q. Roles of Carbon Nanotubes in Novel Energy Storage Devices. *Carbon N. Y.* **2017**, *122*, 462.

[98] Dai, H. Carbon Nanotubes : Opportunities and Challenges. *Surf. Sci.* **2002**, *500*, 218.

[99] Tan, J. M.; Arulselvan, P.; Fakurazi, S.; Ithnin, H.; Hussein, M. Z. A Review on Characterizations and Biocompatibility of Functionalized Carbon Nanotubes in Drug Delivery Design. *J. Nanomater.* **2014**, *2014*, 917024.

[100] Sun, L.; Wang, X.; Zhang, K. Metal-Free SWNT/Carbon/MnO_2 Hybrid Electrode for High Performance Coplanar. *Nano Energy* **2016**, *22*, 11.

[101] Sun, L.; Wang, X.; Liu, W.; Zhang, K.; Zou, J.; Zhang, Q. Optimization of Coplanar High Rate Supercapacitors. *J. Power Sources* **2016**, *315*, 1.

[102] Andrea Szabó, Caterina Perri, Anita Csató, Girolamo Giordano, D. V. and J. B. N. Synthesis Methods of Carbon Nanotubes and Related Materials. *Materials (Basel).* **2010**, *3*, 3092.

[103] Cui, H.; Yan, X.; Monasterio, M.; Xing, F. Effects of Various Surfactants on the Dispersion of MWCNTs–OH in Aqueous Solution. *Nanomaterials* **2017**, *7*, 262.

[104] Adenuga, A. A.; Truong, L.; Tanguay, R. L.; Remcho, V. T.; Initiative, N. N.; Nanoscience, O.; Health, E. Preparation of Water Soluble Carbon Nanotubes and Assessment of Their Biological Activity in Embryonic Zebrafish. *Int. J. Biomed. Nanosci. Nanotechnol* **2015**, *3*, 38.

[105] Dong, C.; Campell, A. S.; Eldawud, R.; Perhinschi, G.; Rojanasakul, Y.; Zoica, C. Effects of Acid Treatment on Structure , Properties and Biocompatibility of Carbon Nanotubes. *Appl. Surf. Sci.* **2013**, *264*, 261.

[106] Tian, Z.; Shi, Y.; Yin, M.; Shen, H.; Jia, N. Functionalized Multiwalled Carbon Nanotubes- Anticancer Drug Carriers : Synthesis , Target- Ing Ability and Antitumor Activity. *Nano. Biomed. Eng.* **2011**, *3*, 157.

[107] Le, V. T.; Ngo, C. L.; Le, Q. T.; Ngo, T. T. Surface Modification and Functionalization of Carbon Nanotube with Some Organic Compounds. *Adv. Nat. Sci. Nanosci. Nanotechnol.* **2013**, *4*, 035017.

[108] Geng, H.-Z.; Kim, K. K.; So, K. P.; Lee, Y. S.; Chang, Y.; Lee, Y. H. Effect of Acid Treatment on Carbon Nanotube-Based Flexible Transparent Conducting Films. *J. Am. Chem. Soc.* **2007**, *129*, 7758.

2

Manganese oxide-mesoporous carbon nanocomposite as a promising anode material for lithium-ion cells

This chapter deals with the attempts carried out to develop a promising anode material for applications in Li-on cells, based on the composite of manganese oxide (Mn_3O_4) nanoflakes and mesoporous carbon (MC), obtained by simple physical mixing method. Hydrothermal method is used to synthesize Mn_3O_4 nanoflakes with a length of 40-50 nm. The structural and morphological studies reveal the uniform dispersion of Mn_3O_4 nanoflakes on the surface of MC, providing good electrical conductivity and structural stability during Li-ion diffusion and ultimately resulting in improved electrochemical performance. The composite electrode delivers an initial discharge capacity of 1601 mA h g^{-1} at a current density of 100 mA g^{-1} and after 100 cycles a discharge capacity of 730 mA h g^{-1} is maintained. The anode also exhibits excellent rate capability performance and even at a current density of 2000 mA g^{-1} a discharge capacity of 378 mA h g^{-1} has been observed. The impressive electrochemical performance exhibited by the nanocomposite offers high application prospects as the anode material in the designing of the next generation lithium-ion cells.

2.1 Introduction

Growing environmental concerns due to the uncurbed use of conventional energy sources and the startling developments in the field of portable electronic devices and automobiles have motivated the research community to develop clean, efficient and environmentally friendly high energy density batteries.[1–3] The lithium-ion battery (LIB) commercialized in 1991 by Sony is the prime energy storage source of most of the available electronic gadgets due to its high gravimetric and volumetric energy and long cycle life.[4–7] With the development of hybrid electric vehicles the role of LIBs has broadened as it is mandatory to develop LIBs with two to five times more energy density to power the vehicles.[8,9] The current lithium ion cell technology has to be suitably modified to achieve much higher energy density through developing cathode and anode materials with high capacity and good cycling stability.

Lithium metal shows the highest capacity of 3860 mA h g^{-1} among various anode materials, but safety concerns avert its usage in secondary batteries.[10,11] Graphite dominates as the conventional anode material in commercialized Li-ion cells due to its excellent cycling performance, low cost, unconcerned safety issues and eco-friendly nature.[12–14] The major drawback of graphite anode is its lower theoretical capacity around 372 mA h g^{-1}.[15,16] The development of novel types of anode materials with high capacity is the key to realize high energy density Li-ion cells. Investigations on carbonaceous materials such as graphene,[17,18] carbon nanotubes[19] and porous carbon[20] and non-carbonaceous materials like silicon,[13] germanium,[21] tin,[22] and metal oxides[23–25] have been carried out to find suitable alternatives to the conventional graphite anode for developing Li-ion cells with higher energy density.

Among the various prospective anode materials, transition metal oxides which undergo conversion type reaction with Li have been widely investigated, owing to the high specific capacity offered by them. The transition metal oxide, Mn_3O_4 is one of the most promising materials to be considered as the anode for Li-ion cells, as it has several advantages like earth abundance, low toxicity and high theoretical capacity of 936 mA h g^{-1}.[26–28] However, the practical application of Mn_3O_4 is limited by issues of its low electrical conductivity of about 10^{-7}-10^{-8} S cm^{-1}, large volume changes upon cycling and unstable solid electrolyte interface (SEI) formation, which ultimately lead to rapid capacity fading and poor rate performance.[29–31] To overcome the mentioned issues, the most commonly employed strategy is to combine Mn_3O_4 with carbon materials.[32–34] Carbon materials are earth abundant, comparatively cheaper and exhibit excellent electrical conductivity, which is vital for the rate performance and cyclability of the cells.

Several studies based on Mn_3O_4 as the anode material for Li-ion cells as well as the electrode material for supercapacitor applications have been reported. Anilkumar and co-workers have developed Mn_3O_4/rGO composite with tailored morphology, having high application prospects as the supercapacitor electrode with high power density and exceptional cycling stability.[35] Jian-Gan's group has synthesized flexible Graphene/Mn_3O_4 composite for application as anode material in Li-ion cells with high specific capacity and good capacity retention.[36] Luo and co-workers have synthesized Mn_3O_4/rGO composite by an ultrasound-assisted method, showing quite high capacity and rate capability.[37] Zhang's group has. synthesized Mn_3O_4/Zn_2SnO_4

composite with high specific capacity and good cycling stability with prospective application as the anode material for Li-ion cells.[38]

In the present study, Mn_3O_4-mesoporous carbon (MC) nanocomposite, composed of nanoflakes of Mn_3O_4 synthesized by hydrothermal method using a surfactant and mesoporous carbon, obtained by the simple physical mixing method has been investigated to assess its suitability as the anode material for high energy density Li-ion cells. The Mn_3O_4-MC nanocomposite is found to exhibit high specific capacity, excellent cycling stability and good rate capability suitable for the anode material of the next generation Li-ion cells.

2.2 Experimental

2.2.1 Materials

For the synthesis of Mn_3O_4, manganese acetate tetra hydrate (MATH), hexadecyltrimethylammonium bromide (CTAB), graphite flakes and hydrazine hydrate (HH) purchased from Sigma-Aldrich were used. Mesoporous carbon was used as received and chemical synthesis was carried out using distilled water.

2.2.2 Synthesis of Mn_3O_4 nanoflakes

Hydrothermal method was used for the synthesis of Mn_3O_4 nanoflakes. Synthesis involved the preparation of a saturated aqueous solution of MATH by dissolving 4.9 g of MATH in 10 ml of distilled water and stirring the solution for 1 hour. Subsequently, 1 M aqueous solution of CTAB was added dropwise to the above solution, and the stirring was continued for another 3 hours. After the stirring was completed, 10 ml of hydrazine hydrate was added to the solution. The

resulting brown coloured solution was transferred immediately to a Teflon lined autoclave and maintained at 150 ℃ for 12 hours in a furnace. Upon completion of the hydrothermal reaction, the solution was allowed to cool down to room temperature, and was washed several times with distilled water and ethanol. It was then filtered and dried overnight at 80 ℃ to get Mn_3O_4 nano flakes.

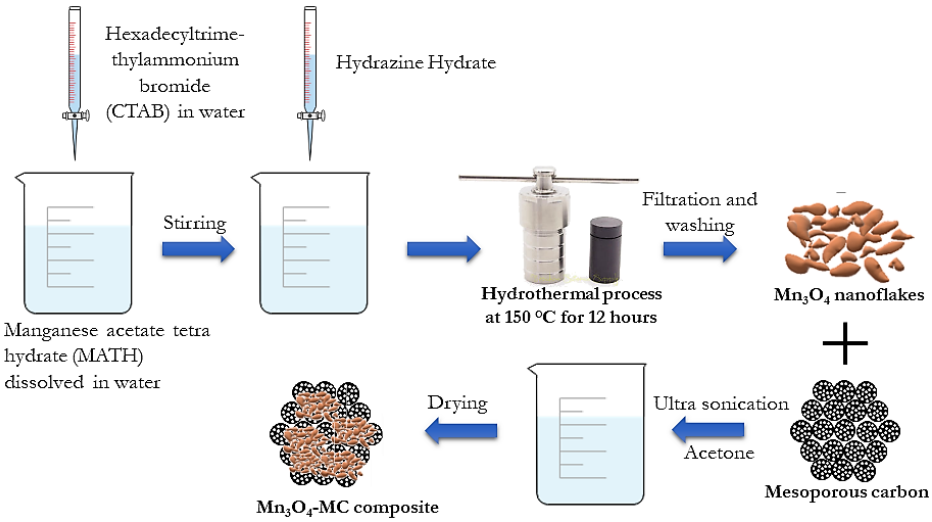

Figure 2.1. Schematic representation of the synthesis of Mn_3O_4-MC nanocomposite

2.2.3 Synthesis of Mn_3O_4-MC nanocomposite (MnMC)

The nanocomposite, Mn_3O_4-MC, short titled as MnMC was synthesized by mixing Mn_3O_4 and MC in the weight ratio of 1:1, dispersed in acetone, and sonicating for 3 hours followed by ultrasonication for another 3 hours. A physical mixture of Mn_3O_4 and MC was obtained by drying the resultant solution. The schematic representation of the synthesis of MnMC nanocomposite is shown figure 2.1.

2.2.4 Structural and morphological characterization

X-ray diffraction studies of Mn_3O_4, MC and the MnMC nanocomposite were carried out using PANalytical X'Pert PRO machine with Cu- Kα radiation of wavelength 1.54 Å. Carl-Zeiss Sigma scanning electron microscope was used to collect the FE-SEM images and the EDAX mapping was done using the Energy X-ray Dispersive Spectrometer Quantax 200 - EDS (Bruker Nano GmbH). Raman spectra were acquired using the Lab RAM HR Spectrophotometer (HORIBA Jobin Yvon) with Argon ion (514.5 nm) laser as the excitation source. The HR-TEM images were taken using Jeol/JEM 2100, transmission electron micrscope.

2.2.5 Electrochemical studies

The electrochemical analysis of the MnMC nanocomposite was carried out using the Swagelok cells assembled in an argon-filled glove box with lithium as the reference electrode, Celgard as the separator and 1 M $LiPF_6$ solution in a 1:1 mixture solvent of ethylene carbonate and dimethyl carbonate (1:1 volume ratio) as the electrolyte (70 μl). The working electrodes were prepared by mixing 80 wt.% MnMC nanocomposite, 10 wt.% acetylene black as conductive carbon and 10 wt.% polyvinylidene difluoride (PVDF) dissolved in N-methyl-2-pyrrolidone (NMP) solvent. The resultant slurry was then coated on copper foil, which acts as the current collector and dried in a vacuum oven at 70 ℃ for 12 hours. After drying, circular electrodes were punched out from the coated foil with mass loading of active material around 1.5 mg. The assembled Swagelok cells were galvanostatically cycled at various charge-discharge current densities within the potential between 0.01 V and 3 V on a 8 channel battery analyzer (MTI

Corporation-USA) at room temperature. The cyclic voltammetry (CV) studies were conducted using Bio-logic SP300 workstation at a scan rate of 0.1 mV s^{-1} in the potential range of 0.01-3 V.

2.3 Results and discussion

2.3.1 X-ray diffraction (XRD) analysis

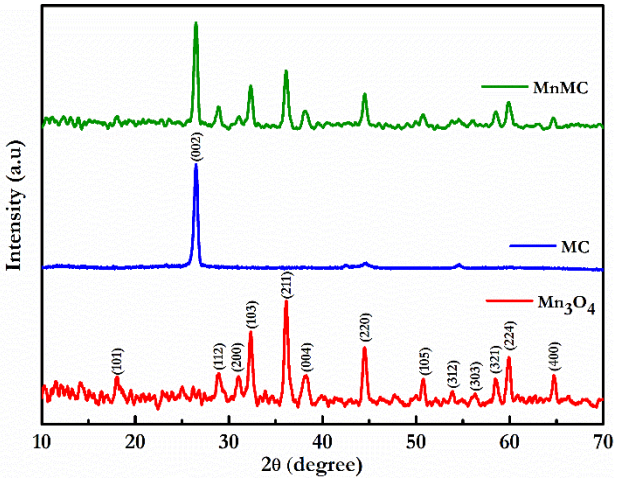

Figure 2.2. XRD patterns of Mn_3O_4, MC and the MnMC nanocomposite.

The XRD patterns of Mn_3O_4, MC and MnMC nanocomposite are shown in figure 2.2. The diffraction peaks of Mn_3O_4 observed at 2θ angles of 17.9°, 29°, 31°, 32.3°, 36.1°, 38.2°, 44.5°, 50.7°, 53.8°, 56.1°, 58.5°, 59.9° and 64.7° correspond to the (101), (112), (200), (103), (211), (004), (220), (105), (312), (303), (321), (224) and (400) planes of pure crystalline tetragonal phase of Mn_3O_4.[39] The pattern of MC shows a sharp peak at 26.4° corresponding to (002) diffraction from graphitic carbon.[40] The MnMC nanocomposite shows diffraction peaks corresponding to both Mn_3O_4 and MC phases, indicating that the Mn_3O_4 particles are incorporated well with the MC particles after the physical mixing.

2.3.2 Raman analysis

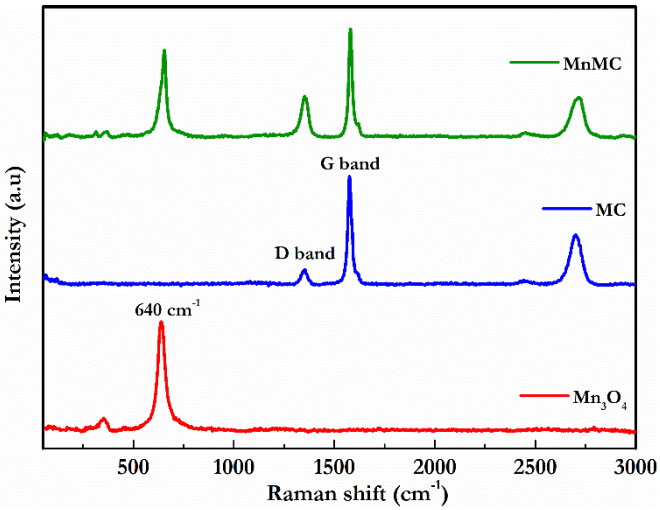

Figure 2.3. Raman spectra of Mn_3O_4, MC and the MnMC nanocomposite.

The Raman spectra of Mn_3O_4, MC and the MnMC nanocomposite are shown in figure 2.3. The spectrum of Mn_3O_4 shows a minor peak at 352 cm^{-1} and a dominant one at 640 cm^{-1}. The sharp peak is assigned to the A_{1g} mode, which corresponds to the Mn–O breathing vibrations of divalent manganese ions in tetrahedral coordination.[41,42] Two peaks are observed in the Raman spectrum of MC, one at 1351 cm^{-1}, corresponding to the D band and the other one at 1575 cm^{-1}, assigned to the G band. The D band is related to the carbon defects and the G band corresponds to the in-plane vibrations of the sp^2 hybridized carbon atoms. The intensity ratio I_D/I_G is observed to be 0.13. The peak observed at 2700 cm^{-1} is the overtone of the D band.[43,44] The Raman spectrum of the MnMC nanocomposite displays the significant peaks of Mn_3O_4 and MC and the intensity ratio I_D/I_G is found to increase to 0.37, suggesting that during the composite formation the graphite

surface may be partially destroyed and Mn_3O_4 particles may occupy some space of the crystalline graphite surface.[43]

2.3.3 FE-SEM, EDAX and HR-TEM analysis

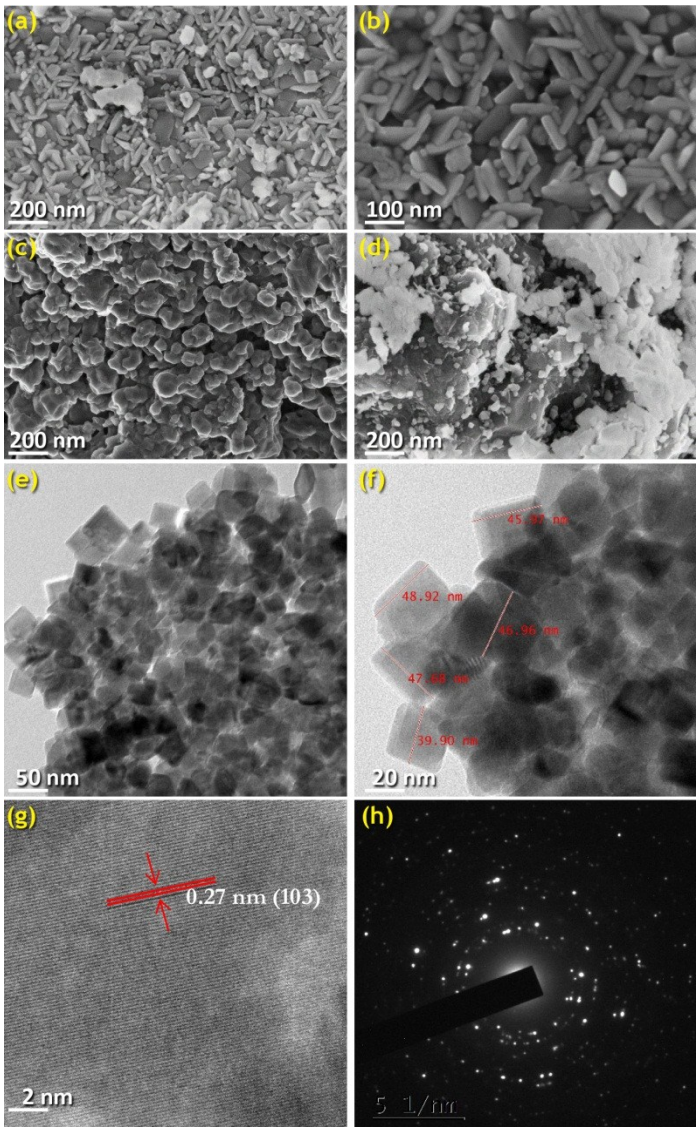

Figure 2.4. FE-SEM images of (a and b) Mn_3O_4 nano flakes, (c) MC, (d) MnMC composite, (e-g) TEM images of MnMC composite and (h) SAED pattern of MnMC composite.

The morphology and structure of the synthesized Mn_3O_4 and the MnMC nanocomposite were analyzed by employing the FE-SEM and TEM techniques and the corresponding images are depicted in figure 2.4. The FE-SEM images shown in figures 2.4a and 2.4b display the homogeneous arrangement of nanoflakes shaped Mn_3O_4 with least agglomeration of particles. For MC, micro-beads like structure is observed as seen from figure 2.4c. The Mn_3O_4 particles positioned on the MC surface is clearly visible form the FE-SEM image of the MnMC nanocomposite, shown in figure 2.4d. The TEM images of the MnMC nanocomposite, shown in figures 2.4(e-f), illustrate the presence of well-formed nanoflakes of Mn_3O_4 with a length of 40-50 nm, attached to the surface of MC. The HR-TEM image of the composite, depicted in figure 2.4g clearly shows lattice fringes of 0.27 nm, corresponding to the (103) plane of Mn_3O_4.[45] The diffraction rings with bright spots observed in the selected area electron diffraction (SAED) pattern shown in figure 2.4h of the MnMC nanocomposite is characteristic of crystalline nanomaterials, with the bright spots corresponding to the crystalline Mn_3O_4. The EDAX spectrum of the MnMC nanocomposite and the corresponding elemental mapping of MnMC, manganese, carbon and oxygen are displayed in figure 2.5.

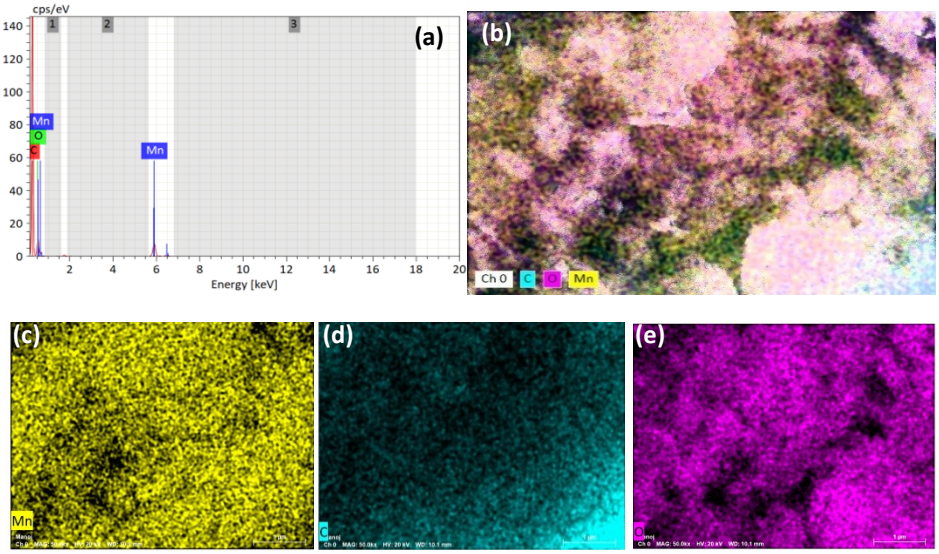

Figure 2.5. (a) EDAX spectrum of the MnMC composite and elemental mapping of (b) MnMC composite, (c) manganese, (d) carbon and (e) oxygen.

2.3.4 Electrochemical performance of MnMC nanocomposite

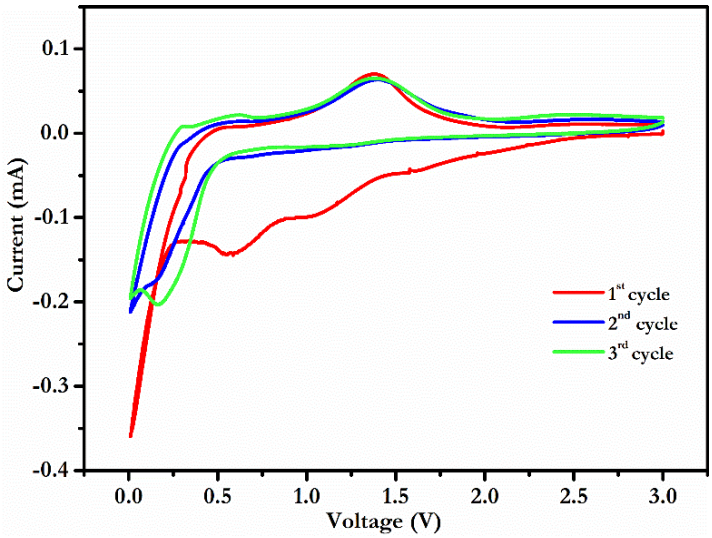

Figure 2.6. Cyclic voltammetry curves of MnMC composite at a scan rate of 0.1 mV s^{-1} in the range of 0.01-3 V.

The cyclic voltammetry (CV) studies of the MnMC nanocomposite anode material were carried out at a scan rate of 0.1 mV s^{-1}. The initial three CV curves in the voltage range of 0.01 V to 3 V are shown in figure 2.6. It is observed that in the first cathodic scan three peaks appear at 1.03 V, 0.6 V and 0.02 V. The peak at 1.03 V corresponds to the reduction of Mn_3O_4 to MnO and that at 0.6 V, to the formation of the solid electrolyte interphase (SEI) layer on the electrode surface due to the electrolyte decomposition. The first two peaks disappear in the subsequent cycles.[46] The sharp cathodic peak observed at 0.02 V is related to the reduction of MnO to metallic Mn and Li_2O.[47] In the following anodic scan, the peak at 1.3 V corresponds to the oxidation of metallic Mn to MnO.[39]

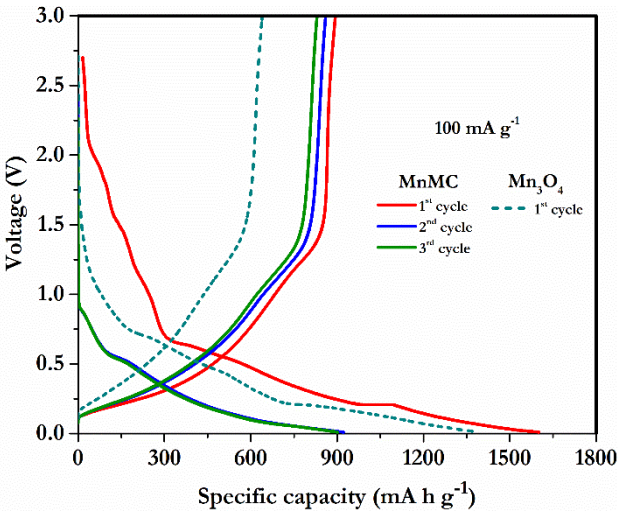

Figure 2.7. Charge-discharge profiles of MnMC nanocomposite (solid lines) and Mn_3O_4 (dotted lines) between 0.01 V and 3 V at a current density of 100 mA g^{-1}.

The slight shift observed in the reduction peak at 0.02 V, after the first cycle is mainly due to the formation of Mn and Li_2O which leads to

structural rearrangements.[48] Similar CV curve is observed after the second cycle and the oxidation peak remains unaltered, indicating good, reversible electrochemical behavior of the MnMC composite electrode.[49]

The galvanostatic charge-discharge curves of Mn_3O_4 and MnMC nanocomposite at a current density of 100 mA g^{-1} are displayed in figure 2.7. The first cycle discharge and charge capacities of MnMC nanocomposite are found to be 1601 mA h g^{-1} and 894 mA h g^{-1}, respectively and the second cycle discharge and charge capacities are around 920 mA h g^{-1} and 882 mA h g^{-1}, respectively. Meanwhile, at the same current density, the first cycle discharge and charge capacities observed for bare Mn_3O_4 are 1390 mA h g^{-1} and 640 mA h g^{-1} respectively. The discharge capacity observed in the first cycle is higher than the theoretical capacity of 937 mA h g^{-1} for Mn_3O_4. In the first cycle, the discharge capacity is contributed by the conversion reaction of Mn_3O_4 to Mn and also by the formation of SEI on the electrode surface, which is excluded from the theoretical capacity of Mn_3O_4.[50] Higher discharge capacity is usually shown by metal oxides used as anode materials for lithium storage.[34]

The lithiation and delithiation reactions occurring during the initial discharge-charge cycle can be described as follows: [51,52]

Initial discharge:

(a) $Mn_3O_4 + Li^+ + e^- \rightarrow LiMn_3O_4$ [1.5-0.5 V vs Li/Li^+]

(b) $LiMn_3O_4 + Li^+ + e^- \rightarrow Li_2O + 3MnO$ [1.5-0.5 V vs Li/Li^+]

(c) $MnO + 2Li^+ + 2e^- \rightarrow Li_2O + Mn$ [0.5-0.0 V vs Li/Li^+]

Initial charge:

(d) $Li_2O + Mn \rightarrow MnO + 2Li^+ + 2e^-$ [0.5-3.0 V vs Li/Li^+]

The first discharge curve differs from those of the succeeding cycles due to the occurrence of irreversible reactions represented by equations (a) and (b) which is in analogy with the CV test results. The reversible electrochemical reactions occurring from the second cycle onwards involve only MnO and metallic Mn as described below:

(e) $MnO + 2Li^+ + 2e^- \leftrightarrow Li_2O + Mn$

Thus, the conversion reaction causes the disintegration of Mn_3O_4 into fragments leading to the formation of MnO and consequently Mn. Also, Li_2O is the inevitable side product of the Mn_3O_4 conversion reaction which is thermodynamically stable.

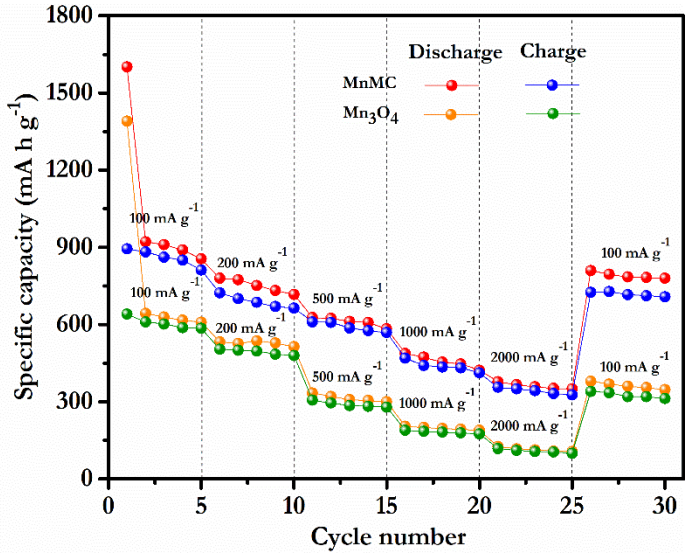

Figure 2.8. Rate capability of MnMC nanocomposite and bare Mn_3O_4 at various current densities.

The rate performance of pure Mn_3O_4 and MnMC nanocomposite at different current densities from 100 mA g^{-1} to 2000 mA g^{-1} is shown in figure 2.8. The MnMC nanocomposite delivers reversible capacity of 378 mA h g^{-1} at the current density of 2000 mA g^{-1}. Further, when the current density is reverted back to 100 mA g^{-1} the discharge capacity of the nanocomposite electrode is still as high as 810 mA h g^{-1}. Meanwhile, Mn_3O_4 shows a discharge capacity of 126 mA h g^{-1} at the current density of 2000 mA g^{-1} and on decreasing the current density to 100 mA g^{-1} the discharge capacity is only 380 mA h g^{-1}. The rate performance studies establish the superior behavior of the MnMC nanocomposite compared to pure Mn_3O_4 and also the excellent stability of the nanocomposite at high current densities. The improved rate performance of the MnMC nanocomposite can be credited to the enhancement in the electrical conductivity of the composite due to the presence of MC. The comparative assessment of the specific capacities of Mn_3O_4 and the MnMC nanocomposite at various current densities is illustrated in table 2.1.

Table 2.1. Comparison of the specific capacities of Mn_3O_4 and MnMC nanocomposite at various current densities.

Current density (mA g^{-1})	Specific Capacity (mA h g^{-1})			
	Mn_3O_4		MnMC nanocomposite	
	Discharge (mA h g^{-1})	Charge (mA h g^{-1})	Discharge (mA h g^{-1})	Charge (mA h g^{-1})
100	1390	640	1601	894
200	533	504	780	723
500	334	306	627	610
1000	204	189	488	469
2000	126	118	378	356
100	380	340	810	725

The cycling performance of the MnMC nanocomposite was analyzed at a current density of 100 mA g^{-1} in the voltage range of 0.01 V to 3 V and the results obtained are depicted in figure 2.9. The charge-discharge cycling process remains quite stable for 100 cycles and the MnMC nanocomposite delivers discharge and charge capacities of 730 mA h g^{-1} and 675 mA h g^{-1}, respectively after 100 cycles with a Coulombic efficiency of 92 %.

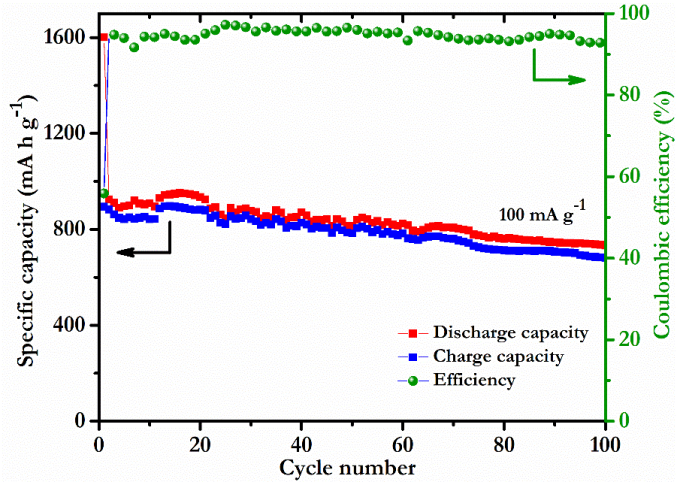

Figure 2.9. Cycling performance and Coulombic efficiency of MnMC composite at a current density of 100 mA g^{-1}.

The remarkable cycling performance and the excellent rate capability achieved for the MnMC nanocomposite of the present work constitute the best result among those from the various Mn_3O_4-carbonaceous materials-based composites, investigated as anodes for Li-ion cell applications (Table 2.2), especially considering the simple synthesis procedure employed in the present work.

Table 2.2. Comparison of previous results on Mn_3O_4-carbon materials-based anodes for lithium-ion cells.

Material	**Synthesis method**	**Rate performance (Discharge capacity)**	**Capacity retention**	**Ref**
Mn_3O_4-Graphene Hybrid	Two-step-solution phase reaction	1350 mA h g^{-1} at 40 mA g^{-1} 390 mA h g^{-1} at 1600 mA g^{-1}	730 mA h g^{-1} (40 cycles)	53
Nanostructured Mn_3O_4/C	One-step polyol-assisted pyro-synthesis	1580 mA h g^{-1} at 33 mA g^{-1} 202 mA h g^{-1} at 1056 mA g^{-1}	600 mA h g^{-1} (30 cycles)	46
Graphene/Mn_3O_4 nanocomposite	Vacuum filtration	1271 mA h g^{-1} at 100 mA g^{-1} 308 mA h g^{-1} at 2000 mA g^{-1}	830 mA h g^{-1} (50 cycles)	36
Porous Mn_3O_4 nanorod/reduced graphene oxide	Vacuum filtration + thermal treatment	1050 mA h g^{-1} at 50 mA g^{-1} 196 mA h g^{-1} at 2000 mA g^{-1}	752 mA h g^{-1} (25 cycles)	54
Mn_3O_4-Graphene nanocomposite	Microwave hydrothermal technique	1354 mA h g^{-1} at 40 mA g^{-1} 400 mA h g^{-1} at 1000 mA g^{-1}	900 mA h g^{-1} (50 cycles)	34
Mn_3O_4/MWCNT composite	Solvothermal route	1380 mA h g^{-1} at 100 mA g^{-1} 387 mA h g^{-1} at 1000 mA g^{-1}	592 mA h g^{-1} (50 cycles)	55
Mn_3O_4/ordered mesoporous carbon	Precipitation + annealing method	1843 mA h g^{-1} at 100 mA g^{-1} -	802 mA h g^{-1} (50 cycles)	56
Sponge network-shaped Mn_3O_4/C anode	One-pot metal organic framework-combustion technique	1186 mA h g^{-1} at 100 mA g^{-1} 155 mA h g^{-1} at 10000 mA g^{-1}	442 mA h g^{-1} (150 cycles)	39
Acid treated reduced graphene oxide /Mn_3O_4 nanorod	Mixing and heat treatment	1130 mA h g^{-1} at 100 mA g^{-1} 412 mA h g^{-1} at 2000 mA g^{-1}	802 mA h g^{-1} (25 cycles)	45
Mn_3O_4/mesoporous carbon composite	Physical mixing method	1601 mA h g^{-1} at 100 mA g^{-1} 378 mA h g^{-1} at 2000 mA g^{-1}	810 mA h g^{-1} (25 cycles)	Present work

The impressive electrochemical performance of the MnMC nanocomposite can be ascribed to the following factors.[56] The presence of MC in the composite improves the electrical contact between Mn_3O_4 particles and MC by providing conductive channels and ultimately leading to high capacity during cycling. The crystalline structure of MC offers large electrode-electrolyte contact area, increases accessible sites on electrode surface and reduces the transport path for Li ion diffusion. The superior structural stability of MnMC nanocomposite helps to secure control over the agglomeration and crumbling of Mn_3O_4 particles due to the volume expansion occurring during the cycling process. The MC promotes higher electrolyte diffusion into the electrode material and the mesopores benefits faster ion transport during the charge-discharge cycling and thus maintains high capacitance even at high current densities.

2.4 Conclusions

The nanocomposite electrode Mn_3O_4-MC is obtained by the simple physical mixing of the components, using nanoflakes of Mn_3O_4 obtained by hydrothermal method and the mesoporous carbon (MC). The structural and morphological studies confirm that the Mn_3O_4 nanoflakes are almost uniform in size and shape and in the nanocomposite, they are attached to the surface of MC. The presence of MC improves the overall electrical conductivity of the nanocomposite, offers short diffusion pathways for Li ions and provides structural stability to the composite electrode during lithiation/de-lithiation processes. The nanocomposite shows superior electrochemical performance by delivering an initial discharge capacity of 1601 mA h g^{-1} at a current density of 100 mA g^{-1} and

excellent rate performance at higher current density of 2000 mA g^{-1}. Furthermore, the nanocomposite electrode displays remarkable cycling stability and a capacity of 730 mA h g^{-1} is retained after 100 cycles at a current density of 100 mA g^{-1}. The simple and cost-effective synthesis procedure employed in the present study appears to be a viable route for developing carbon composites-based anode materials for the next generation Li-ion cells with much higher capacity and energy density suitable for applications in hybrid electric vehicles.

References

[1] Roy, P.; Kumar, S. Nanostructured Anode Materials for Lithium-Ion Batteries. *J. Mater. Chem. A* **2015**, *3*, 2454–2484.

[2] Qi, W.; Shapter, J. G. Nanostructured Anode Materials for Lithium-Ion Batteries: Principle, Recent Progress and Future Perspectives. *J. Mater. Chem. A* **2017**, *5*, 19521–19540.

[3] Deng, Y.; Wan, L.; Xie, Y.; Chen, G. Recent Advances in Mn-Based Oxides as Anode Materials for Lithium Ion Batteries. *RSC Adv.* **2014**, *4*, 23914–23935.

[4] Armand, M. Issues and Challenges Facing Rechargeable Lithium Batteries. *Nature* **2001**, *414*, 359–367.

[5] Jie Yue, Xin Gu,a Liang Chen, Nana Wang, Xiaolei Jiang, Huayun Xu, J. Y. and Y. Q. General Synthesis of Hollow MnO_2, Mn_3O_4 and MnO Nanospheres as Superior Anode Materials for Lithium Ion Batteries. *J. Mater. Chem.* **2014**, *2*, 17421–17426.

[6] M Ge, X Fang, J. R. and C. Z. Review of Porous Silicon Preparation and Its Application for Lithium-Ion Battery Anodes. *Nanotechnology* **2013**, *24*, 422001.

[7] Whittingham, M. S. Lithium Batteries and Cathode Materials. *Chem. Rev.* **2004**, *104*, 4271–4301.

[8] Michael M. Thackeray, C. W. and E. D. I. Electrical Energy Storage for Transportation—approaching the Limits of, and Going beyond, Lithium-Ion Batteries. *Energy Environ. Sci.* **2012**, *5*, 7854–7863.

[9] Tarascon, J.; Recham, N.; Armand, M.; Barpanda, P.; Walker, W.; Dupont, L.; Verne, D. P. J.; Umr, C. Hunting for Better Li-Based Electrode Materials via Low Temperature Inorganic Synthesis . *Chem. Mater.* **2010**, *22*, 724–739.

[10] Liu, J. Addressing the Grand Challenges in Energy Storage. *Adv. Funct. Mater.* **2013**, *23*, 924–928.

[11] Orsini, F. In Situ SEM Study of the Interfaces in Plastic Lithium Cells. *J. Power Sources* **1999**, *81*, 918–921.

[12] Scrosati, B.; Garche, J. Lithium Batteries : Status, Prospects and Future. *J. Power Sources* **2010**, *195*, 2419–2430.

[13] Xu, Z.; Liu, X.; Luo, Y.; Zhou, L.; Kim, J. Nanosilicon Anodes for High Performance Rechargeable Batteries. *Prog. Mater. Sci.* **2017**, *90*, 1–44.

[14] Persson, K.; Sethuraman, V. A.; Hardwick, L. J.; Hinuma, Y. Lithium Diffusion in Graphitic Carbon. *J. Phys. Chem. Lett.* **2010**, *1*, 1176–1180.

[15] Kaskhedikar, B. N. A.; Maier, J. Lithium Storage in Carbon Nanostructures. *Adv. Mater.* **2009**, *21*, 2664–2680.

[16] Lian, P.; Zhu, X.; Xiang, H.; Li, Z.; Yang, W.; Wang, H. Enhanced Cycling Performance of Fe_3O_4 – Graphene Nanocomposite as an Anode Material for Lithium-Ion Batteries. *Electrochim. Acta* **2010**, *56*, 834–840.

[17] Hou, J.; Shao, Y.; Ellis, M. W.; Moore, B.; Yi, B. Graphene-Based Electrochemical Energy Conversion and Storage : Fuel Cells, Supercapacitors and Lithium Ion Batteries. *Phys. Chem. Chem. Phys.* **2011**, *13*, 15384–15402.

[18] Amer, A. A.; Reda, S. M.; Mousa, M. A.; Mohamed, M. M. Mn_3O_4/Graphene Nanocomposites: Outstanding Performances as Highly Efficient Photocatalysts and Microwave Absorbers†. *RSC Adv.* **2017**, *7*, 826–839.

[19] Landi, B. J. Carbon Nanotubes for Lithium Ion Batteries. *Energy Environ. Sci.* **2009**, *2*, 549–712.

[20] Zhou, B. H.; Zhu, S.; Hibino, M. Lithium Storage in Ordered Mesoporous Carbon (CMK-3) with High Reversible Specific Energy Capacity and Good Cycling Performance. *Adv. Mater.* **2003**, *15*, 2107–2111.

[21] Hwang, I.; Kim, J.; Seo, S.; Lee, S.; Lee, J.; Kim, D. A Binder-Free Ge-Nanoparticle Anode Assembled on Multiwalled Carbon Nanotube Networks for Li-Ion Batteries. *Chem. Commun.* **2012**, *48*, 7061–7063.

[22] Zhuo, K.; Jeong, M.; Chung, C. Highly Porous Dendritic Ni-Sn Anodes for Lithium-Ion Batteries. *J. Power Sources* **2013**, *244*, 601–605.

[23] Wang, H.; Pan, Q.; Zhao, J.; Chen, W. Fabrication of CuO/C Films with Sisal-like Hierarchical Microstructures and Its Application in Lithium Ion Batteries. *J. Alloys Compd.* **2009**, *476*, 408–413.

[24] Huang, X. H.; Xia, X. H.; Yuan, Y. F.; Zhou, F. Porous ZnO Nanosheets Grown on Copper Substrates as Anodes for Lithium Ion Batteries. *Electrochim. Acta* **2011**, *56*, 4960–4965.

[25] Hassan, M. F.; Guo, Z. P.; Chen, Z.; Liu, H. K. Carbon-Coated MoO_3 Nanobelts as Anode Materials for Lithium-Ion Batteries. *J. Power Sources* **2010**, *195*, 2372–2376.

[26] Wang, J.; Zhang, C.; Kang, F. Nitrogen-Enriched Porous Carbon Coating for Manganese Oxide Nanostructures toward High-Performance Lithium-Ion Batteries. *ACS Appl. Mater. Interfaces* **2015**, *7*, 9185–9194.

[27] Huang, S.; Jin, J.; Cai, Y.; Li, Y.; Tan, H.; Wang, H.; Van, G. Engineering Single Crystalline Mn_3O_4 Nano-Octahedra with Exposed Highly Active {011} Facets for High Performance Lithium Ion Batteries. *Nanoscale* **2014**, *6*, 6819–6827.

[28] Bai, Z.; Zhang, X.; Zhang, Y.; Guo, C.; Tang, B. Facile Synthesis of Mesoporous Mn_3O_4 Nanorods as a Promising Anode Material for High Performance Lithium-Ion Batteries†. *J. Mater. Chem. A* **2014**, *2*, 16755–16760.

[29] Wang, J.; Du, N.; Wu, H.; Zhang, H.; Yu, J.; Yang, D. Order-Aligned Mn_3O_4 Nanostructures as Super High-Rate Electrodes for Rechargeable Lithium-Ion Batteries. *J. Power Sources* **2013**, *222*, 32–37.

[30] Ponrouch, A.; Taberna, P.; Simon, P.; Palacín, M. R. On the Origin of the Extra Capacity at Low Potential in Materials for Li Batteries Reacting through Conversion Reaction. *Electrochim. Acta* **2012**, *61*, 13–18.

[31] Pasero, D.; Reeves, N.; West, A. R. Co-Doped Mn_3O_4 : A Possible Anode Material for Lithium Batteries. *J. Power Sources* **2005**, *141*, 156–158.

[32] Wang, C.; Yin, L.; Xiang, D.; Qi, Y. Uniform Carbon Layer Coated Mn_3O_4 Nanorod Anodes with Improved Reversible Capacity and Cyclic Stability for Lithium Ion Batteries. *ACS Appl. Mater. Interfaces* **2012**, *4*, 1636–1642.

[33] Liu, S.; Xie, J.; Zheng, Y.; Cao, G.; Zhu, T.; Zhao, X. Nanocrystal Manganese Oxide (Mn_3O_4 , MnO) Anchored on Graphite Nanosheet with Improved Electrochemical Li-Storage Properties. *Electrochim. Acta* **2012**, *66*, 271–278.

[34] L. Li, Z. Guo, A. D. and H. L. Rapid Microwave-Assisted Synthesis of Mn_3O_4–graphene Nanocomposite and Its Lithium Storage Properties†. *J. Mater. Chem.* **2012**, *22*, 3600–3605.

[35] Anilkumar, KM.; Manoj, M.; Jinisha, B.; VS, P.; Jayalekshmi, S. Mn_3O_4/Reduced Graphene Oxide Nanocomposite Electrodes with Tailored Morphology for High Power Supercapacitor Applications. *Electrochim. Acta* **2017**, *236*, 424–433.

[36] Wang, J.; Jin, D.; Zhou, R.; Li, X.; Liu, X.; Shen, C.; Xie, K.; Li, B.; Kang, F.; Wei, B. Highly Flexible Graphene/Mn_3O_4 Nanocomposite Membrane as Advanced Anodes for Li-Ion Batteries. *ACS Nano* **2016**, *10*, 6227–6234.

[37] Luo, Y.; Fan, S.; Hao, N.; Zhong, S.; Liu, W. An Ultrasound-Assisted Approach to Synthesize Mn_3O_4/RGO Hybrids with High Capability for Lithium Ion Batteries. *Dalt. Trans.* **2014**, *43*, 15317–15320.

[38] Liqiang, S. Facile Synthesis of One-Dimensional Mn_3O_4/Zn_2SnO_4 Hybrid Composites and Their High Performance as Anodes for LIBs. *Nanoscale* **2014**, *6*, 14221–14226.

[39] Sambandam, B.; Soundharrajan, V.; Song, J.; Kim, S. A Sponge Network-Shaped Mn_3O_4/C Anode Derived from a Simple, One-Pot Metal Organic Framework-Combustion Technique for Improved Lithium Ion Storage. *Inorg. Chem. Front.* **2016**, *3*, 1609–1615.

[40] Manoj, M.; Jasna, M.; Anilkumar, K. M.; Abhilash, A.; Jinisha, B.; Pradeep, V. S. Sulfur-Polyaniline Coated Mesoporous Carbon Composite in Combination with Carbon Nanotubes Interlayer as a Superior Cathode Assembly for High Capacity Lithium-Sulfur Cells. *Appl. Surf. Sci.* **2018**, *458*, 751–761.

[41] Julien, C. M.; Massot, M.; Poinsignon, C. Lattice Vibrations of Manganese Oxides Part I . Periodic Structures. *Spectrochim. Acta Part A* **2004**, *60*, 689–700.

[42] Wang, L.; Li, Y.; Han, Z.; Chen, L.; Qian, B.; Jiang, X. Composite Structure and Properties of Mn_3O_4/Graphene Oxide and Mn_3O_4/Graphene. *J. Mater. Chem. A* **2013**, *1*, 8385–8397.

[43] Hsieh, C.; Yang, B.; Chen, W. Dye-Sensitized Solar Cells Using Mesocarbon Microbead-Based Counter Dye-Sensitized Solar Cells Using Mesocarbon Microbead-Based Counter Electrodes. *Int. J. photoenergy* **2015**, *2012*, 709581.

[44] Xia, H.; Wang, Y.; Lin, J.; Lu, L. Hydrothermal Synthesis of MnO_2/CNT Nanocomposite with a CNT Core/Porous MnO_2 Sheath Hierarchy Architecture for Supercapacitors. *Nanoscale Res. Lett.* **2011**, *7*, 33.

[45] Seong, C.; Park, S.; Bae, Y.; Yoo, S.; Piao, Y. An Acid-Treated Reduced Graphene Oxide/Mn_3O_4 Nanorod Nanocomposite as an Enhanced Anode Material for Lithium Ion Batteries†. *RSC Adv.* **2017**, *7*, 37502–37507.

[46] Alfaruqi, M. H.; Gim, J.; Kim, S.; Song, J.; Duong, P. T.; Jo, J.; Baboo, J. P.; Xiu, Z.; Mathew, V.; Kim, J. One-Step Pyro-Synthesis of a Nanostructured Mn_3O_4/C Electrode with Long Cycle Stability for Rechargeable Lithium-Ion Batteries. *Chem. - A Eur. J.* **2016**, *22*, 2039–2045.

[47] Fangcai Zheng, Dequan Zhu, X. S. and Q. C. Metal–organic Framework-Derived Porous $Mn_{1.8}Fe_{1.2}O_4$ Nanocubes with an Interconnected Channel Structure as High-Performance Anodes for Lithium Ion Batteries. *J. Mater. Chem. A* **2015**, *3*, 2815–2824.

[48] Jian, G.; Xu, Y.; Lai, L.; Zachariah, M. R. Mn_3O_4 Hollow Spheres for Lithium-Ion Batteries with High Rate and Capacity. *J. Mater. Chem. A* **2014**, *2*, 4627–4632.

[49] Huang, H.; Zhang, L.; Xia, Y.; Gan, Y.; Tao, X.; Liang, C.; Zhang, W. Well-Dispersed Ultrafine Mn_3O_4 Nanocrystals on Reduced Graphene Oxide with High Electrochemical Li-Storage Performance. *New J. Chem.* **2014**, *38*, 4743–4747.

[50] Poizot, P.; Laruelle, S.; Grugeon, S.; Dupont, L.; Tarascon, J. Nano-Sized Transition-Metaloxides as Negative-Electrode Materials for Lithium-Ion Batteries. *Nature* **2000**, *407*, 496.

[51] Lowe, M. A.; Gao, J. In Operando X-Ray Studies of the Conversion Reaction in Mn_3O_4 Lithium Battery Anodes. *J. Mater. Chem. A* **2013**, *1*, 2094–2103.

[52] Yonekura, D.; Iwama, E.; Ota, N.; Muramatsu, M. Progress of the Conversion Reaction of Mn_3O_4 Particles as a Function of the Depth of Discharge. *Phys. Chem. Chem. Phys.* **2014**, *16*, 6027–6032.

[53] Wang, H.; Cui, L.; Yang, Y.; Casalongue, H. S. Mn_3O_4-Graphene Hybrid as a High-Capacity Anode Material for Lithium Ion Batteries. *J. Am. Chem. Soc.* **2010**, *132*, 13978–13980.

[54] Park, S.; Seong, C.; Yoo, S.; Piao, Y. Porous Mn_3O_4 Nanorod/Reduced Graphene Oxide Hybrid Paper as a Flexible and Binder-Free Anode Material for Lithium Ion Battery. *Energy* **2016**, *99*, 266–273.

[55] Wang, Z. H.; Yuan, L. X.; Shao, Q. G.; Huang, F.; Huang, Y. H. Mn_3O_4 Nanocrystals Anchored on Multi-Walled Carbon Nanotubes as High-Performance Anode Materials for Lithium-Ion Batteries. *Mater. Lett.* **2012**, *80*, 110–113.

[56] Zhaoqiang Li, Ningning Liu, Xuekun Wang, Changbin Wang, Y. Q. and L. Y. Three-Dimensional Nanohybrids of Mn_3O_4/Ordered Mesoporous Carbons for High Performance Anode Materials for Lithium-Ion Batteries. *J. Mater. Chem.* **2012**, *22*, 16640–16648.

3

Carbon materials for lithium-sulfur cells: A novel cathode assembly based on activated carbon-sulfur composite and carbon nanotubes interlayer

This chapter gives a detailed introduction to lithium-sulfur cell technology and the investigations carried out to develop lithium-sulfur (Li-S) cells based on eco-friendly cathode materials. Activated carbon, derived from natural resources is being extensively investigated for applications as electrode materials in high power supercapacitors and for making composite electrodes for designing high energy density electrochemical cells. The present chapter is aimed at introducing the potential of the composite cathode of sulfur with the biomass-derived, steam activated carbon (AC) along with the free-standing and flexible film of functionalized carbon nanotubes as the interlayer, for designing efficient Li-S cells. The composite obtained by impregnating sulfur particles into the pores of coconut shell derived, steam activated and acid washed carbon, called as the activated carbon-sulfur (ACS) is used as the cathode active material. The flexible film of acid-functionalized carbon nanotubes termed as the CNTF placed between the composite cathode and the separator material serves as an active interlayer to boost the performance efficiency of the assembled Li-S cells. The cells assembled with the ACS composite as the active cathode material and the CNTF as the interlayer are found to exhibit quite impressive discharge capacity and good cycling stability. The use of the coconut shell derived, steam activated and acid washed carbon for making the composite cathode with sulfur along with the CNTF interlayer, obtained by the acid functionalization of carbon nanotubes is a novel approach to realize Li-S cells with high capacity and excellent cycling stability, which has not yet been pursued in detail.

3.1 Introduction

The unprecedented growth in world population and the technologically advanced era we are living in, demand a huge supply of energy to meet our daily needs. It has become a long back tradition to rely largely upon the fossil fuels to meet the growing energy demands. The dependence on the highly polluting and non-renewable, fossil fuels based energy sources and the insatiable thirst for more and more energy production adversely affect the environment, ultimately leading to global warming and the problems related to acid rain and climatic changes, which can endanger even the human existence in this world.[1,2] It is high time to turn our attention towards renewable and pollution-free energy sources to generate clean energy to overcome all the hurdles related to the so called "energy crisis".[3–6] More attention and funding are now being directed towards solar plants and wind farms to ensure the generation of affordable, reliable, sustainable and eco-friendly energy. The development of efficient energy storage systems is the key to gain maximum utilization of these clean energy sources due to the intermittent nature of the energy generated from the sun and the wind.

Rechargeable batteries have played a significant role to meet the growing demands of energy storage systems and hence have become part and parcel of portable electronic devices. These batteries have transformed the portable electronic market with their advantages regarding energy density, cell voltage and cycling stability. Rechargeable electrochemical cells from the oldest lead-acid to the most successful lithium ion, have served to meet the energy demands of the society for over a century. With the rapid advances taking place in the field of

electronic gadgets, power devices, and hybrid electric vehicles, the design and development of novel types of electrochemical cells with high energy density and power density have become the primary target of various battery research groups.[7–11] Even though the lithium-ion cells, commercialized in 1991 have aided and transformed the electronic industry, these types of cells are reaching the limits of their potential and can no longer cope with the exponentially increasing energy demands of the society.[12–15] This technology falls behind when it comes to applications requiring much higher energy density and power density such as electric vehicles which require constant and sustainable energy for long durations.[13,16–18] These requirements have initiated the exploration of novel storage technologies having supremacy over the current lithium-ion technology.

Lithium-sulfur (Li-S) cells have gained widespread research attention, recently, as they offer the potential to overcome the storage limits of the existing Li-ion technology. Besides the high theoretical capacity of sulfur around 1675 mA h g^{-1}, the lower raw material cost and the earth abundance of sulfur make the lithium-sulfur technology, an efficient and relatively inexpensive strategy for energy storage applications.[19,20] The Li-S cells have a high theoretical energy density of 2600 W h kg^{-1}, almost five times higher than that of the commercially available lithium-ion cells.[21–23] However, the commercialization of Li-S cells is yet to be realized and is getting delayed due to some inherent drawbacks of this technology. The high insulating nature of elemental sulfur, with electrical conductivity around 5×10^{-30} S cm^{-1}, the problems related to the dissolution of lithium polysulfides in the electrolyte, the poor ionic conductivity of polysulfides, the polysulfide shuttle phenomenon and

the volume expansion of the sulfur cathode during lithium intake are the main limitations which cause poor cycling stability and significant extent of capacity fading.[24,25] The higher-order polysulfides generated at the cathode during the lithiation process get dissolved in the electrolyte, migrate towards the anode and react with the lithium metal, get reduced to lower-order polysulfides, migrate back to the sulfur cathode to regenerate the higher-order polysulfides again, and continue the cycling process. The above process, termed as the polysulfide shuttle behavior results in low Coulombic efficiency and poor cycling stability of the Li-S cells.[19,26] During lithium intake, the sulfur cathode may undergo enormous volume expansion, which can adversely affect the discharge capacity and the cycling stability of the cells.[3,27,28] In order to get rid of these drawbacks, modifications of the sulfur cathode, using various carbonaceous materials [29–33] and conducting polymers have been attempted.[7,34,35] The above approaches helps in improving the electrical conductivity of the sulfur cathode and in preventing the shuttling of the polysulfides and the volume expansion of sulfur. The addition of lithium nitrate as an electrolyte additive is also effective in hindering the polysulfide shuttle mechanism, since the direct reaction of lithium metal with polysulfides is passivated.[36,37]

The novel type of Li-S cell architecture with the concept of inserting an "interlayer" between the modified sulfur cathode and separator was primarily proposed by Arumugam Manthiram and his co-workers in 2012.[38] In their work, the free-standing interlayer film of multi-walled carbon nanotubes (MWCNTs) obtained by vacuum filtration functions as a pseudo-upper current collector and helps in enriching the overall cell performance. The working of the cell is found

to be significantly improved by incorporating the MWCNTs interlayer without any complex surface modifications and this has opened a new research area in the field of Li-S cells.[39] Afterwards, many types of interlayers based on different nano-structures have come up for enhancing the electrochemical performance of Li-S cells.[40–43] Various strategies have been adopted to address the issues adversely affecting the cell performance, which mainly include the encapsulation of sulfur in an electrically conducting matrix to improve the conductivity of the sulfur cathode and the use of protective coatings over it to minimize the volume expansion of sulfur. Various carbonaceous materials such as mesoporous carbon,[10,44] activated carbon,[45] carbon nanotubes,[46,47] graphene,[48–50] reduced graphene oxide,[51,52] and various conducting polymers including polyaniline,[34,53] PEDOT-PSS[54] and polypyrrole [55] have been used as the encapsulating conducting matrices and as the protective coating layers for the sulfur cathode. Different metal oxides like TiO_2 and MnO_2 have also been employed to improve the electrical properties of the sulfur cathode. [56–58]

Among the various materials used to address the challenges associated with pure sulfur cathodes, biomass-derived carbon materials are quite attractive. However, they have not yet been subjected to detailed studies and are not well utilized. Activated carbon materials (AC) derived from biomass sources such as jackfruit, coconut shell, sugarcane and rice husk are promising green products to be used to improve the performance of the sulfur cathodes in Li-S cells. The added advantages of these materials including the relatively low-cost, the availability of easy processing techniques and the adjustable surface properties have boosted their attention as electro active materials in

energy storage device applications.[59,60] The coconut shell derived carbons dominate among the biomass-derived carbons due to their natural abundance and the desirable electrochemical properties. The activation processes also play a crucial role in determining the performance of the electro active carbon materials.[61]

In order to overcome the adverse effects of the shuttling phenomenon of the polysulfides, the fruitful approach is to trap the polysulfides in the cathode region and obstruct them from reaching the anode. Suitable interlayers inserted between the cathode and the separator are found to be effective to achieve the trapping of the polysulfides in the cathode region.[38] The interlayers with appreciable electrical conductivity also help to reduce the charge transfer resistance of the sulfur cathode.[39,62]

In the present work, the carbon, derived from coconut shell was steam activated and washed with hydrofluoric acid (HF) to achieve maximum purity and is termed as the activated carbon (AC). The composite of pure sulfur powder with the AC was obtained by solvothermal treatment and the resulting carbon-sulfur composite is called as the ACS. The synthesized ACS composite was used as the active cathode material. The flexible film of the acid functionalized carbon nanotubes, termed as the CNTF was placed between the cathode and the separator to serve as an interlayer. The activated carbon in the ACS composite helps in improving the electrical conductivity of sulfur and the porous nature of the activated carbon facilitates the efficient impregnation of sulfur particles within its pores and thereby contributes towards minimizing the volume expansion of sulfur during lithium intake.

The CNTF interlayer efficiently brings about the localization of the higher order polysulfides within the cathode region and restricts the polysulfide shuttle phenomenon and also reduces the charge transfer resistance at the cathode-electrolyte interface. These advantageous aspects significantly contribute towards improving the overall performance of the Li-S cells.

To get a complete picture of the effect of the CNTF interlayer, Li-S cells were assembled with and without the interlayer and the cell performance results were compared. An initial discharge capacity of 1562 mA h g^{-1} at 0.05 C has been observed for the cells with the ACS composite cathode and the CNTF interlayer whereas for the cells with the same cathode without the interlayer the observed initial discharge capacity is 540 mA h g^{-1} at the same current rate. The cells with the ACS composite cathode with the CNTF interlayer show higher capacity retention of 71% at 1 C compared to the lower cycling stability of the cells without the interlayer. The use of the ACS composite cathode and the CNTF interlayer is a cost-effective approach since the AC sample is derived from the biomass, the coconut shell, and the steam activation and the acid washing processes are carried out using optimum quantities of chemicals. Moreover, the application of the CNTF interlayer, developed by the acid functionalization of carbon nanotubes gives a benign touch to the whole process. It has been established that the functionalization of carbon nanotubes results in the minimization of their cytotoxic effects and renders them with better dispersion and biocompatibility.[63–66]

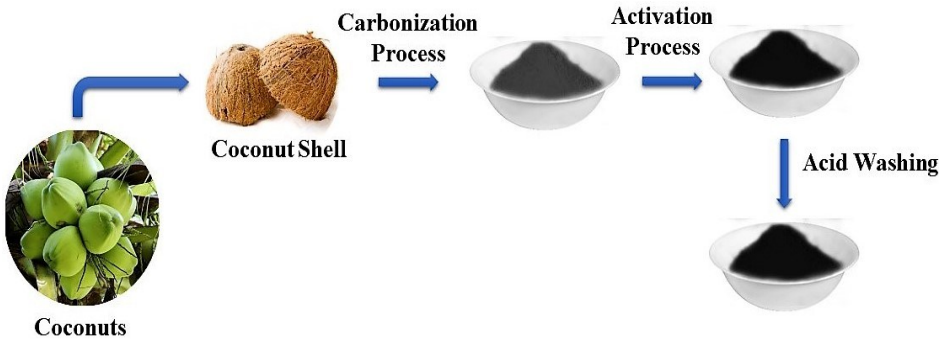

Figure 3.1. Schematic representation of the synthesis of acid washed, steam activated carbon.

3.2 Experimental

3.2.1 Materials

The coconut shell derived, steam activated carbon was acquired from local suppliers. Analytical grade chemicals were used for the synthesis of composites and the synthesis was carried out using distilled water.

3.2.2 Synthesis of acid washed, steam activated carbon (AC)

About 10 g of the purchased coconut shell derived, steam activated carbon was washed well with distilled water and dried overnight at 110 ºC. It was then washed well with 5 vol % NaOH and distilled water several times and dried at 110 °C for 12 hours. In the next step, 5 g of the dried sample was taken in a round-bottomed high-density polyethylene vessel (HDPE) and about 10 ml of 1.2 M hydrofluoric acid (HF) was added. The above mixture was stirred vigorously for 3 hours at room temperature. After the stirring was finished, the HF solution was decanted from the HDPE vessel, then filled with a fresh solution of HF and the washing process was repeated. The final sample was obtained by

continuous washing using distilled water until a neutral pH range was obtained. It was then dried in an oven at 110 ºC for 12 hours. The schematic representation of the synthesis of acid washed, steam activated carbon is shown in figure 3.1.

3.2.3 Synthesis of free-standing and flexible film of acid-functionalized carbon nanotubes (CNTF interlayer)

Multi-walled carbon nanotubes were suspended in a mixture of 6 M H_2SO_4 and 6 M HNO_3 in 3:1 volume ratio and ultra-sonicated for 2 hours. The suspension was refluxed at 120 °C for 12 hours. The resulting solution was then vacuum filtered and washed repeatedly using distilled water. The final product was then dried at 60 °C for 12 hours in a vacuum oven to obtain acid-functionalized carbon nanotubes (CNTs). The functionalized nanotubes powder, dispersed in N-methyl-2-pyrrolidone (NMP) solution was added into the solution of polyvinylidene fluoride (PVDF) in NMP, followed by ultra-sonication for 3 hours to get a uniform dispersion of CNTs in NMP. The whole solution was then poured into a well cleaned teflon petri-dish and kept in a vacuum oven at 60 °C for 12 hours for drying. Finally, free-standing and flexible CNTF films were peeled off the petri-dish. The CNTF films were then punched into small discs of 10 mm diameter, 0.2 mm thickness and 4-6 mg weight to serve as the CNTF interlayers in Li-S cells. The schematic configuration of the Li-S cell with the CNTF interlayer in between the separator and the cathode is illustrated in figure 3.2.

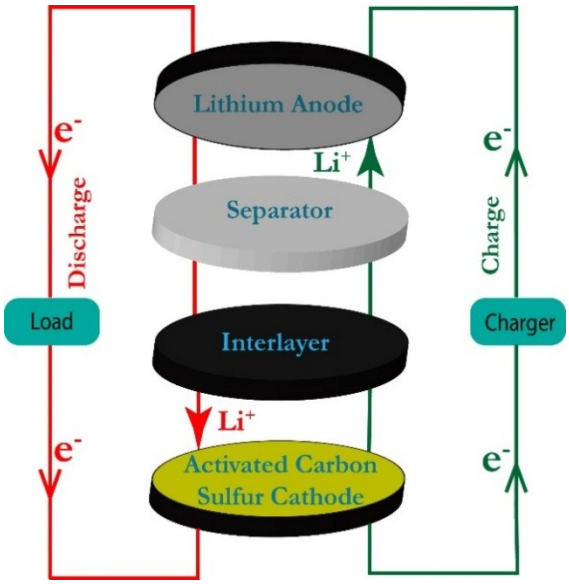

Figure 3.2. Schematic configuration of the Li-S cell with the CNTF interlayer inserted between the cathode and the separator.

3.2.4 Synthesis of acid washed, steam activated carbon-sulfur (ACS) composite

The acid washed, steam activated carbon-sulfur (ACS) composite was synthesized by solvothermal method. The commercially obtained sulfur and the synthesized activated carbon were mixed in a weight ratio of 8:2 in 30 ml of acetone. The resulting solution was then ultra-sonicated in an ice bath for 3 hours and then stirred for another 24 hours at room temperature. Finally, the whole mixture was transferred to an autoclave and then subjected to solvothermal treatment at a temperature of 120 °C for 4 hours. The autoclave was left to cool down to room temperature on the completion of the solvothermal process. Filtration of the resultant mixture was done thoroughly with deionized water. The filtered sample was dried at 80 °C under vacuum to obtain

the final ACS composite. The schematic representation of the synthesis of ACS composite is shown in figure 3.3.

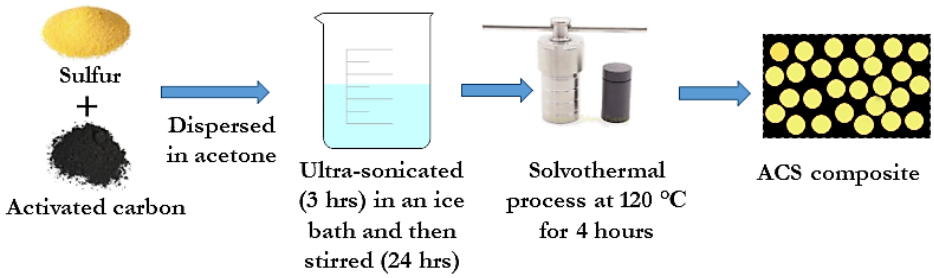

Figure 3.3. Schematic representation of the synthesis of ACS composite

3.2.5 Structural and morphological characterization

The X-ray diffraction (XRD) patterns of the samples were obtained using the PANalytical's X'Pert Pro machine with Cu-Kα radiation of 1.542 Å. The morphological details of the samples were analyzed by field-emission scanning electron microscopy (FE-SEM), using Carl Zeiss Sigma machine and high-resolution transmission electron microscopy (TEM), using Joel/JEM 2100, machine. Raman spectra were recorded using the Lab RAM HR Spectrophotometer (HORIBA Jobin Yvon) with Argon-ion laser (514.5 nm) laser as the excitation source. The BET specific surface area (SSA) measurements on the HF washed, steam activated carbon (AC) used in the present work were done using Micromeritics Tristar II 3020 surface area analyzer as described in one of our recent publications.[67] The samples were degassed at 90 °C for 1 hour and then at 300 °C for 16 hours prior to the measurements. The isotherm was plotted by varying the pressure in between 0.001 and 0.99. The pore size distribution curve was obtained using the desorption branch of the isotherm. Thermogravimetric analysis

(TGA) was conducted on a Perkin Elmer, Diamond TG/DTA instrument to determine the content of sulfur in the composite, at a heating rate of 10 °C min^{-1} in N_2 atmosphere.

3.2.6 Electrochemical studies

The ACS composite cathode electrodes for Li-S cells were prepared from the slurry containing 80 wt.% of ACS composite, 10 wt.% of acetylene black and 10 wt.% of polyvinylidene difluoride (PVDF) in N-methyl-2-pyrrolidone (NMP) solvent. The homogeneous slurry was then spray coated on an aluminium foil and after drying at 60 °C under vacuum for 12 hours, the cathode electrodes were cut into circular discs of 10 mm diameter with a sulfur loading of approximately 1.3 mg cm^{-2}. Using stainless steel Swagelok cells, Li-S cells were assembled by stacking the ACS composite as the cathode active material, Li foil as the anode and Celgard as the separator in an argon-filled glove box, with 1 M lithium perchlorate in a mixed solvent of 1, 3-dioxolane (DOL) and 1, 2-dimethoxymethane (DME) at a volume ratio of 1:1 including 0.5 M $LiNO_3$ as an electrolyte additive, as the electrolyte.[68,69] The synthesized CNTF interlayer was placed between the separator and the ACS cathode. The amount of electrolyte added to each cell was 70 μl. The cyclic voltammetry (CV) test was carried out at a scan rate of 0.1 mV s^{-1} in the voltage window of 1.5-3 V and the electrochemical impedance spectroscopy (EIS) studies, in the frequency range between 1 MHz and 10 mHz, using Bio-Logic SP300 workstation. The test cells were charge-discharge cycled between 1.5 and 3 V at various C-rates (1 C=1650 mA g^{-1}) using the 8 channel battery analyzer (MTI Corporation-USA) at room temperature.[25,38,40]

3.3 Results and discussion

3.3.1 BET surface area analysis

The BET surface area analysis on the activated carbon used in the present work displays a combination of both type I and type IV isotherms, indicating micro and meso porous nature as detailed in our earlier publication.[67,70] Generally, type I isotherms are the characteristic ones for micro-porous solids and type IV isotherms, those for mesoporous solids.[71,72] The presence of a considerable fraction of macropores is also anticipated due to the absence of well-defined saturation plateau in the isotherms. A hierarchical porosity nature spanning from the micro-porous to meso-porous and to macro-porous seems to constitute the microstructure of the AC sample.[73] The results show that the contribution from micro-pores dominates over the other two. The important parameters from the BET analysis are summarized in table 3.1.

Table 3.1. BET surface area, pore volume and the average pore size of the AC sample

Sample	**Surface area ($m^2\ g^{-1}$)**	**Avg. Pore size (Å)**	**Total Pore volume ($cm^3\ g^{-1}$)**	**Micropore area ($m^2\ g^{-1}$)**	**Micropore area (%)**
AC	1864	18.75	0.874	690	37

3.3.2 X-ray diffraction (XRD) analysis

The XRD patterns of AC, sulfur and the ACS composite are shown in figure 3.4. The pattern of AC shows no crystalline peaks which is an indication of its amorphous nature.[74] The diffraction peaks in the range 15° to 60°, observed in the XRD pattern of sulfur are in

good agreement with the already reported literature values for orthorhombic sulfur.[75,76] The XRD pattern of the ACS composite is almost similar to that of sulfur, sulfur being the bulk content in the ACS composite.

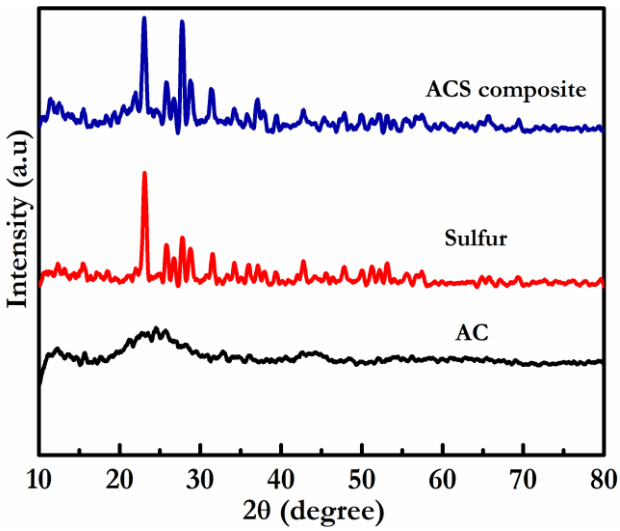

Figure 3.4. XRD patterns of Activated Carbon, Sulfur and the ACS composite

3.3.3 Raman spectroscopy studies

Raman spectra of CNTs and acid functionalized CNTs were probed to understand the impact of acid treatment on the structure of the CNTs and the results are displayed in figure 3.5. The characteristics peaks observed at 1346 cm^{-1}, 1574 cm^{-1}, and 2689 cm^{-1} for both the CNTs and the functionalized CNTs correspond to the D, G and G' bands, respectively. After functionalization, the intensity ratio I_D/I_G is found to increase to 0.82 from 0.62 which implies that the acid functionalization brings about structural distortions in the CNTs

network.[77] The acid treatment also facilitates the good dispersion of the CNTs in NMP solution with reduced agglomeration.[78]

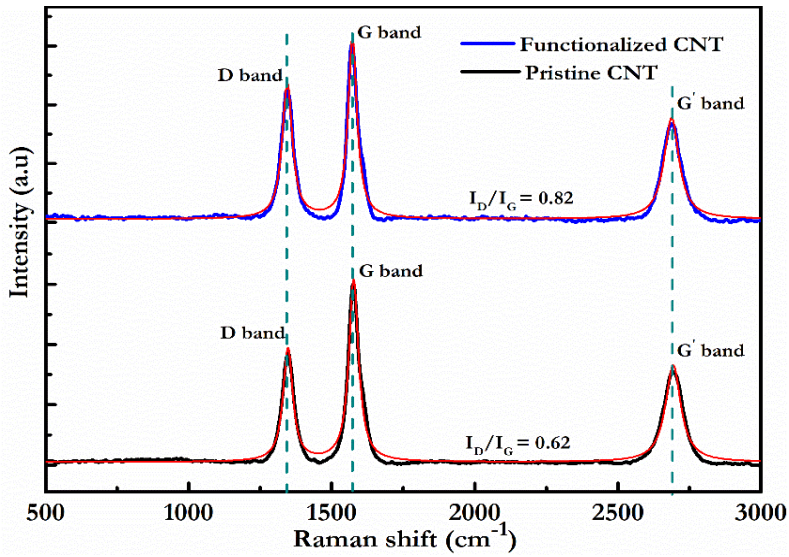

Figure 3.5. Raman spectra of CNTs and acid functionalized CNTs

Raman spectra of sulfur, AC and the ACS composite are displayed in figure 3.6. In the Raman spectrum of sulfur shown in figure 3.6a, a series of peaks are observed at 153 cm^{-1}, 219 cm^{-1}, and 473 cm^{-1} which are in good agreement with the reported data and correspond to those of orthorhombic sulfur.[79] There are two typical Raman peaks in the spectrum of AC shown in figure 3.6b, located at 1340 cm^{-1} and 1590 cm^{-1} which are related to the D-band and the G-band, respectively and the intensity ratio I_D/I_G of AC is observed to be 1.16. The D band corresponds to the defects in the carbon structure and the G band is linked to the vibrations of sp^2 carbon atoms.[80] The Raman spectrum of the ACS composite, shown in figure 3.6c, displays the significant peaks

of sulfur, while those of AC are not visible because of the presence of the high-intensity sulfur peaks in the composite. The distinct scan of the ACS composite in the range 1000-2000 cm^{-1} as depicted in figure 3.6d reveals the characteristics peaks of AC. After the reaction of AC with sulfur the intensity ratio I_D/I_G is found to decrease to 1.11, and slight changes in the positions of D and G bands are also observed in the spectrum of the composite which can be associated with the interaction of sulfur with carbon during the solvothermal process.[81,82]

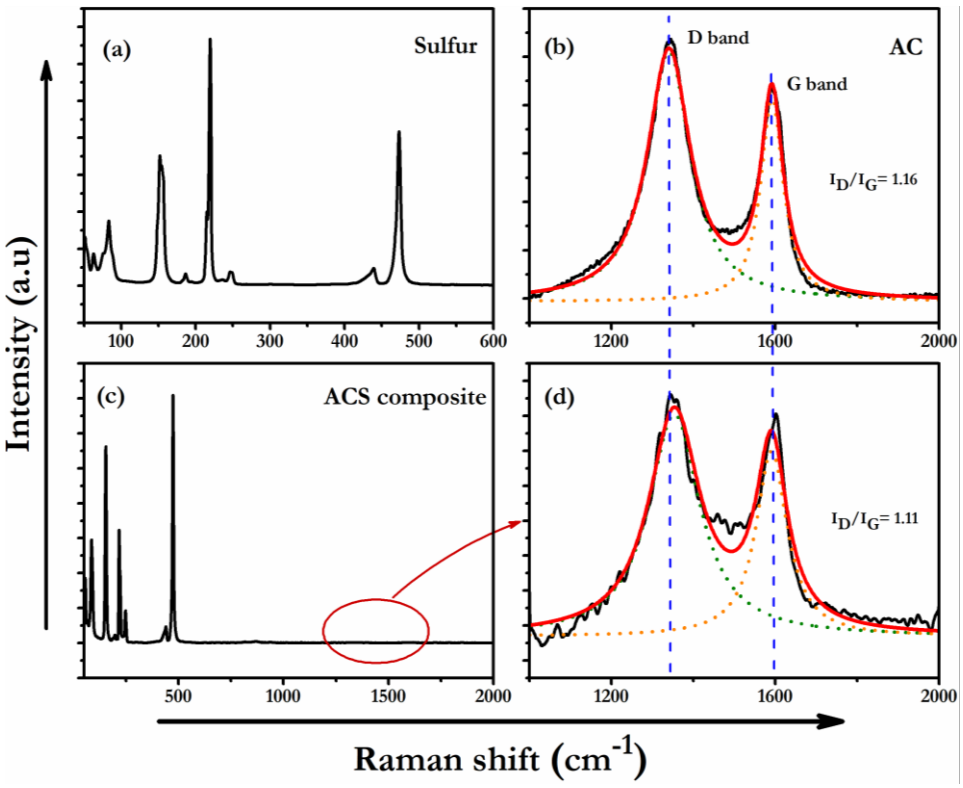

Figure 3.6. Raman spectra of (a) Sulfur, (b) AC, (c) ACS composite and (d) the ACS composite spectrum scanned in the range 1000-2000 cm^{-1}.

3.3.4 FE-SEM, TEM and EDAX analysis

The FE-SEM images of AC and the ACS composite and the TEM images of the ACS composite are shown in figure 3.7. The FE-SEM images in figure 3.7a and 3.7b clearly show the well-developed pores on the surface of the AC. The images of the ACS composite shown in figure 3.7c and 3.7d show that the sulfur particles get impregnated into the pores of AC after the solvothermal treatment. Most of the sulfur particles get well diffused into the pores of AC and the remaining ones aggregate on the surface of AC. The TEM image of the ACS composite shown in figure 3.7e gives further justification to the filling of pores of the activated carbon with sulfur particles.[83] The dark phase observed in the TEM image shows the trapping of the sulfur particles in the pores of AC.[84–86] The corresponding selected area electron diffraction (SAED) pattern depicted in figure 3.7g exhibits diffused ring patterns having brighter spots typically representing the presence of AC, with the bright spots signifying the crystalline sulfur in the composite. The lattice fringes of graphitic carbon layer with a spacing of 0.34 nm can be seen in figure 3.7f.[87,88] The EDAX spectrum of the ACS composite and the corresponding elemental mapping of sulfur, carbon and oxygen are displayed in figure 3.8 which also reveal the sulfur distribution in the composite.

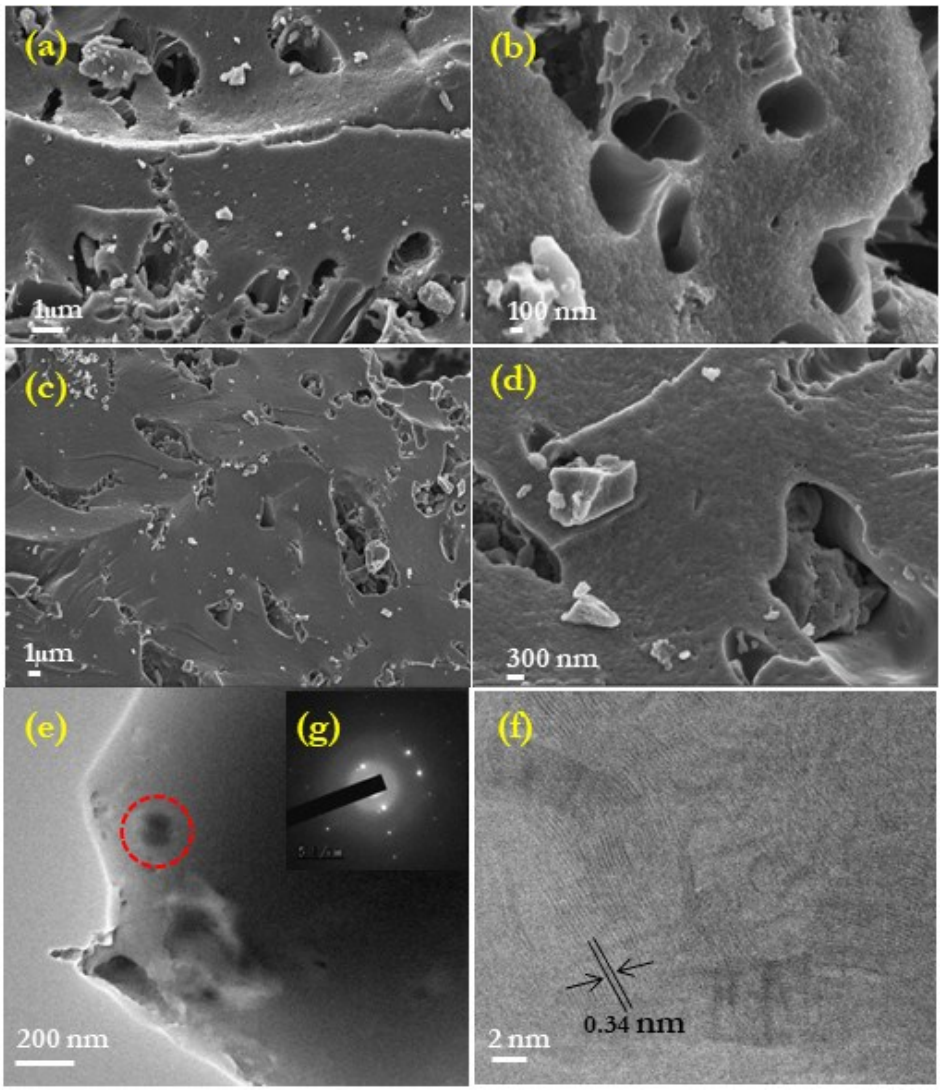

Figure 3.7. FE-SEM images (a-b) of AC, (c-d) of the ACS composite and TEM images (e-f) and the SAED pattern (g) of the ACS composite.

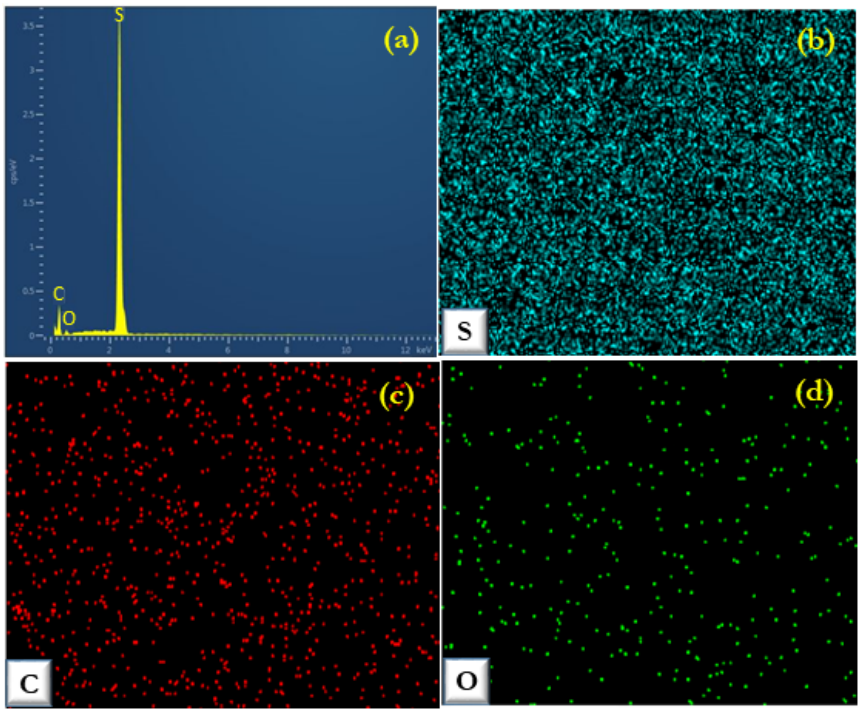

Figure 3.8. (a) EDAX spectrum of the ACS composite and the elemental mapping of (b) sulfur, (c) carbon and (d) oxygen.

3.3.5 Thermogravimetric (TGA) analysis

The TGA curves of AC, sulfur and the ACS composite under N_2 flow are shown in figure 3.9 and the sulfur content in the ACS composite is determined from the thermal analysis. The TGA curve of AC shows an initial weight loss corresponding to the removal of moisture content from the sample at around 100 °C. Mass loss observed above 600 °C corresponds to the decomposition of AC. Pure sulfur completely burns at around 330 °C, and in the ACS composite this sublimation temperature varies from 330 °C to 350 °C, perhaps due to the confinement of sulfur particles in the pores of AC and the weight loss above 600 °C in the ACS composite is related to the thermal

degradation of AC.[89,90] From the TGA data, the content of sulfur in the ACS composite is calculated as approximately 80 wt.%.

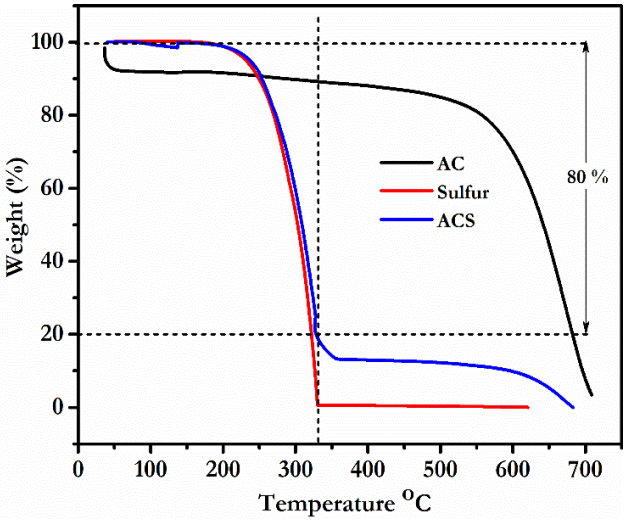

Figure 3.9. TGA curves of AC, sulfur and the ACS composite.

3.3.6 Electrochemical analysis

3.3.6.a Cyclic voltammetry (CV) analysis

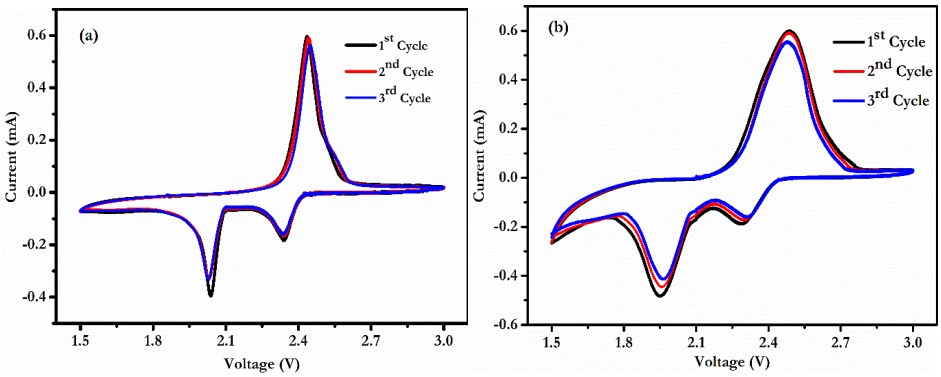

Figure 3.10. Cyclic voltammetry curves of the assembled Li-S cells (a) without the CNTF interlayer (b) with the CNTF interlayer at a scan rate of 0.1 mV s^{-1}.

The cyclic voltammetry (CV) curves at a scan rate of 0.1 mV s^{-1} between 1.5 V and 3 V of the Li-S cells for the first three cycles without and with the CNTF interlayer are shown in figures 3.10a and 3.10b, respectively. The curves exhibit two reduction peaks in the cathodic sweep and one oxidation peak in the anodic sweep for both the cell configurations which are consistent with the typical behaviour of sulfur cathodes.[91] It is evident from the figures that there is an increase in the redox current of the cells with the CNTF interlayer which is an indication of the better utilization of the sulfur cathode. Also, the broadening and slight shifts in the positions of the redox peaks for the Li-S cells with the interlayer show that the CNTF interlayer helps in improving the overall electrical conductivity of the cathode assembly and also in the effective conversion between the polysulfides and sulfur.[38] In the CV curves of the cells with the CNTF interlayer, the anodic and the cathodic peaks are identical for the first three cycles without significant shifts in peak locations or changes in intensities, suggesting the excellent cycling stability possessed by the system. The peak positioned at 2.3 V during the cathodic scan indicates the reduction of sulfur to soluble higher order lithium polysulfides (Li_2S_n, $4 \leq n \leq 8$), while the other reduction peak at 1.95 V represents the further reduction of the higher order lithium polysulfides to the lower order insoluble Li_2S_2 and ultimately to Li_2S.[50,92] The anodic peak at 2.48 V during the anodic sweep, indicates the conversion of Li_2S_2/Li_2S to polysulfides and sulfur.[93] The absence of other additional redox peaks for the Li-S configuration with the CNTF interlayer reveals the electrochemically inactive nature of the interlayer and the lack of any contribution to the final storage capacity of the cell.[47]

3.3.6.b Charge-discharge studies

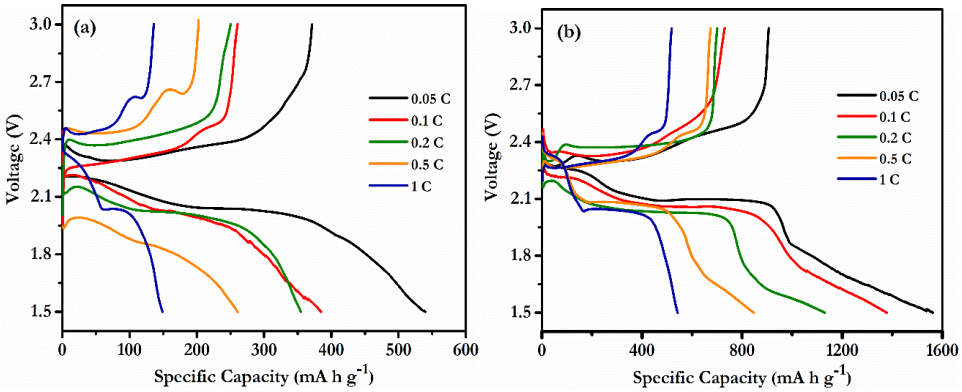

Figure 3.11. Discharge-charge profiles of the Li-S cells at various C-rates (a) Without the CNTF interlayer (b) With the interlayer.

The charge-discharge curves of the Li-S cells without and with the CNTF interlayer at various C-rates (1 C=1650 mA g^{-1}) are shown respectively in figures 3.11a and 3.11b. The cells without the interlayer exhibit a much lower initial discharge capacity and rapid capacity fading even at lower C-rates. Initial discharge capacities of 540 mA h g^{-1} and 385 mA h g^{-1} are observed at current rates of 0.05 C and 0.1 C respectively for the cells without employing the CNTF interlayer. At higher C-rates the initial discharge capacity gets further lowered indicating poor electrochemical activity of the cells without the interlayer. Significant improvement has been found in the charge-discharge capacities of the cells with the interlayer. The cells with the ACS cathode and the CNTF interlayer exhibit high initial discharge capacity of 1562 mA h g^{-1} at 0.05 C which is almost three times the capacity observed at the same C-rate for the cells without the interlayer.

The same improvement is retained in the discharge capacities even at higher current rates in the cells with the interlayer. On gradually increasing the C-rate to 0.1 C, 0.2 C, 0.5 C and 1 C, the cells are found to display an initial discharge capacity of 1378 mA h g^{-1}, 1129 mA h g^{-1}, 846 mA h g^{-1} and 542 mA h g^{-1} respectively. The charge-discharge capacities of the Li-S cells at various current rates without and with the CNTF interlayer are shown in table 3.2. The observed capacity decay in the following cycles, compared to the initial discharge capacity of the first discharge cycle can be ascribed to the low cutting off voltage of 1.5 V, where the reduction of $LiNO_3$ in the electrolyte occurs.[40,94–96]

The slope in the discharge curves observed at lower rates is mainly attributed to the reduction of $LiNO_3$, which is used as a co-salt in the electrolyte.[38] It is generally used as a co-salt in electrolytes due to its benefits on improving the Coulombic efficiencies of Li-S cells. On Li anode, it is reported to form a passivation film, which suppresses the redox shuttle of lithium polysulfides. The main limitation of $LiNO_3$ is its irreversible reduction on the cathode at lower voltages and this can be avoided by raising the discharge cut off potential. In the present studies, it is used only as a co-salt to improve the electrochemical properties. In the cells without the CNTF interlayer, $LiNO_3$ present in the electrolyte is mostly consumed during the formation of the passivation layer on Li anode. Presence of small reduction slopes in the curves of the cells with the interlayer can be due to the retention of $LiNO_3$ in the electrolyte, trapped within the porous interlayer, where it undergoes reduction process at lower voltages. At higher current rates,

this reduction is generally not visible in the Galvanostatic Cycling with Potential Limitation (GCPL) curves.[38,97]

The peaks observed in the charge curves at higher C rates (0.5 C and 1 C) are the results of the over potential due to the surface coverage by Li_2S. According to the previous reports, the kinks observed in the charge profile and the charge rates are linked, since the over potential drops with decreasing charge rates. This drop in the over potential at lower cycling rates is perhaps due to the longer span of time accessible for the full oxidation process of Li_2S to occur at lower rates.[98] The over potential of the charge curve is also influenced by the state of the sulfur cathode at the end of the discharge cycle.[99]

Table 3.2. Comparison of specific capacities of the ACS based Li-S cells at various scan rates without and with the CNTF interlayer.

Scan Rates	Specific Capacity (mA h g^{-1})			
	Without the CNTF interlayer		With the CNTF Interlayer	
	Discharge (mA h g^{-1})	Charge (mA h g^{-1})	Discharge (mA h g^{-1})	Charge (mA h g^{-1})
0.05 C	540	371	1562	905
0.1 C	385	261	1378	730
0.2 C	355	250	1129	700
0.5 C	261	202	846	674
1 C	149	136	542	518

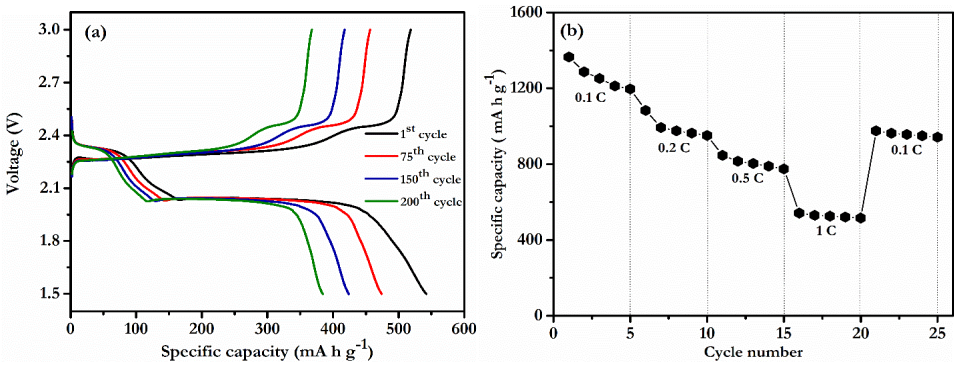

Figure 3.12. (a) Discharge-charge profiles of the Li-S cells with the CNTF interlayer after different number of cycles at 1 C (b) Rate performance of the cells with the CNTF interlayer.

The various stages of discharge-charge curves of the assembled Li-S cells employing the ACS composite cathode with the CNTF interlayer at 1 C rate are shown in figure 3.12a. At a current rate of 1 C the cells retain a discharge capacity of 384 mA h g^{-1} after 200 cycles from the initial discharge capacity of 542 mA h g^{-1} showing a capacity retention of about 71%. The charge efficiency of higher than 100% for the initial two cycles can be ascribed to the re-utilization of the sulfur core in the cathode as the cell is cycled, which is generally found in the Li-S cells during the initial cycles.[62] The rate performance of the cells with the CNTF interlayer at various C-rates from 0.1 C to 1 C in the voltage range 1.5 V-3 V is evaluated and displayed in figure 3.12b. During the initial cycles, capacity fading is observed and the cells deliver a discharge capacity of 1197 mA h g^{-1} at the end of the fifth cycle at 0.1 C-rate. After the initial five charge-discharge cycles, the cells attain stability and remain steady up to the end of the 20th cycle. In the interval between the 5th and the 20th cycle, the charge-discharge current was varied at different rates of 0.2 C, 0.5 C and 1 C, with each of these C

rates constituted by 5 cycles. The discharge capacity of the cells remains more or less constant throughout this interval. When the C-rate of the cells with the CNTF interlayer is brought back to 0.1 C from 1 C, the cells are found to restore a discharge capacity of 976 mA h g^{-1}. The admirable rate performance of the cells is due to the good electrical conductivity of the ACS cathode and the faster transport of lithium ions to the cathode material which can be ascribed to the presence of the conductive CNTF interlayer acting as an upper-current collector.[100]

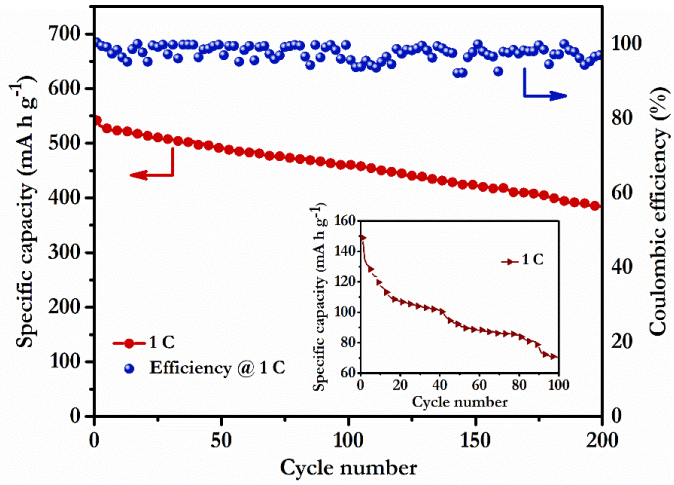

Figure 3.13. Cycle performance and Coulombic efficiency of the Li-S cells with the CNTF interlayer at 1 C.

The cycle performance and the Columbic efficiency of the cells with the interlayer at 1 C rate for 200 cycles are depicted in figure 3.13. The cells with the CNTF interlayer maintain a high Coulombic efficiency and the average value is found to be about 97%. The inset figure shows the cycle performance of the cells without the interlayer at a current rate of 1 C. The cells deliver an initial discharge capacity of 149 mA h g^{-1}, which is below one-third of the discharge capacity delivered by the cells

with the CNTF interlayer at the same C-rate. After 100 cycles the discharge capacity is found to decline sharply indicating low electrochemical utilization of the active material in the cells without the interlayer.

The above discussions highlight the meritorious roles of the novel Li-S configuration developed using the ACS composite cathode and the free-standing and flexible CNTF interlayer inserted between the cathode and the separator in enhancing the specific capacity and the cycling stability of the cells. The use of the ACS composite cathode is a cost-effective and rather benign approach to develop stable Li-S cells with high energy density, since the coconut shell derived carbon is a green product and the steam activation and the HF washing techniques adopted in the present work require easily available chemicals in moderate quantities. The functionalization of the carbon nanotubes is expected to reduce their cytotoxic effects significantly and induce better solubility and biocompatibility.[101,102] The activated carbon with its hierarchical porous nature facilitates the effective impregnation of the sulfur particles within the pores and thus brilliantly plays the decisive role of minimizing the volume expansion of sulfur during lithium intake. The enormous volume expansion of sulfur during lithium insertion is one of the prime aspects adversely affecting the cycling stability of the Li-S cells.[103,104] The good contact between the activated carbon and the embedded sulfur particles enhances the overall electrical conductivity of the composite cathode and consequently improves the electrochemical activity of the system and promotes better utilization of sulfur. Generally, conducting polymers are coated as thin layers over the sulfur cathode to minimize the volume expansion.[105–107] In the present work, the micro-pores dominated surface morphology of the activated carbon

is sufficient to minimize the adverse effects of the volume expansion. Although the use of the ACS composite cathode can rectify most of the inherent drawbacks of the pure sulfur cathode, the electrochemical studies show that the capacity and the cycling stability of the cells using the ACS cathode alone are not attractive. This is mainly due to the shuttling of polysulfides between the electrodes. The shuttling phenomenon considerably reduces the cell capacity and the cycling stability. As mentioned earlier, suitable interlayers inserted between the sulfur cathode and the separator are effective in hindering the polysulfide shuttle phenomenon. In the present work, the presence of the acid functionalized carbon nanotubes (CNTF) interlayer is found to be quite effective in considerably enhancing the capacity and the cycling stability of the assembled Li-S cells.

The excellent cycling and the charge-discharge performance of the cells with the CNTF interlayer can be credited to the effects of the conductive network of the interlayer which ensures improved cathode material utilization and significantly lowers the resistance at the cathode interface. The flexible CNT network facilitates the localization and retention of the dissolved active material during cycling. Most importantly, it accommodates the migrating polysulfides intermediates, preventing their passage to the anode region and thereby hindering the polysulfide shuttle phenomenon.[38,62,108] The conventional configuration of the Li-S cell with the concern over polysulfide shuttling effect and the novel configuration of the cell with the CNTF interlayer inserted between the cathode and the separator are depicted in figures 3.14a and 3.14b, respectively. The effective localization of the polysulfides within the

cathode region by the CNTF interlayer and thereby hindering their transport to the anode are illustrated in figure 3.14b.

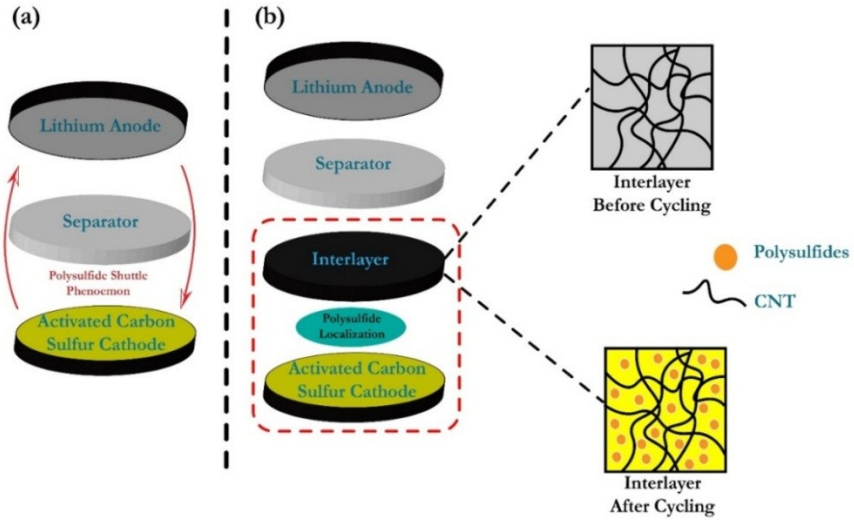

Figure 3.14. (a) Conventional configuration of the Li-S cell. (b) New configuration of the Li-S cell with the CNTF interlayer.

3.3.6.c Electrochemical impedance spectroscopy (EIS) studies

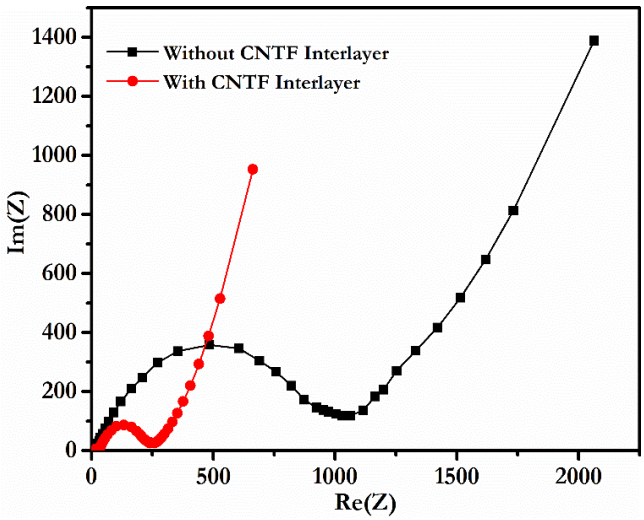

Figure 3.15. Electrochemical impedance spectra of the Li-S cells with and without the CNTF interlayer.

The electrochemical impedance spectroscopy (EIS) is a powerful tool to inspect the internal resistance of Li-S cells. The EIS measurements were carried out in the frequency range between 1 MHz and 10 mHz at the open-circuit voltage. The observed Nyquist plots of the Li-S cells without and with the CNTF interlayer are shown in figure 3.15. In the Nyquist plot, the diameter of the semicircular portion in the high-frequency region gives the charge transfer resistance (R_{ct}) of the cell.[109] It is observed that there is a sharp fall in the value of R_{ct} from 1050 **Ω** to 250 **Ω** for the cells with the CNTF interlayer. This drastic decrease in the value of the charge transfer resistance after the insertion of the CNTF interlayer shows that the effective resistance of the ACS composite cathode gets considerably reduced by the presence of the conductive network of the functionalized carbon nanotubes.[38] The EIS results reveal that the CNTF interlayer helps in better utilization of the cathode material and promotes the electrochemical reactions in the cell.[62,110]

3.3.7 Analysis of CNT interlayer after cycling

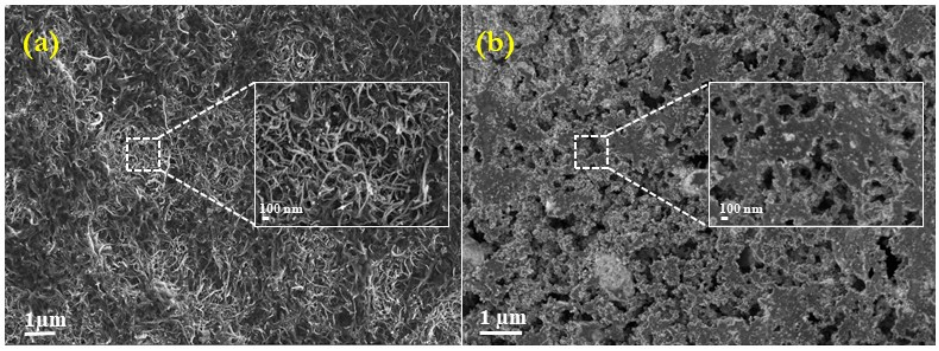

Figure 3.16. FE-SEM images of the CNTF interlayer (a) before cycling (inset: enlarged image), (b) after 200 cycles at 1 C rate (inset: enlarged image).

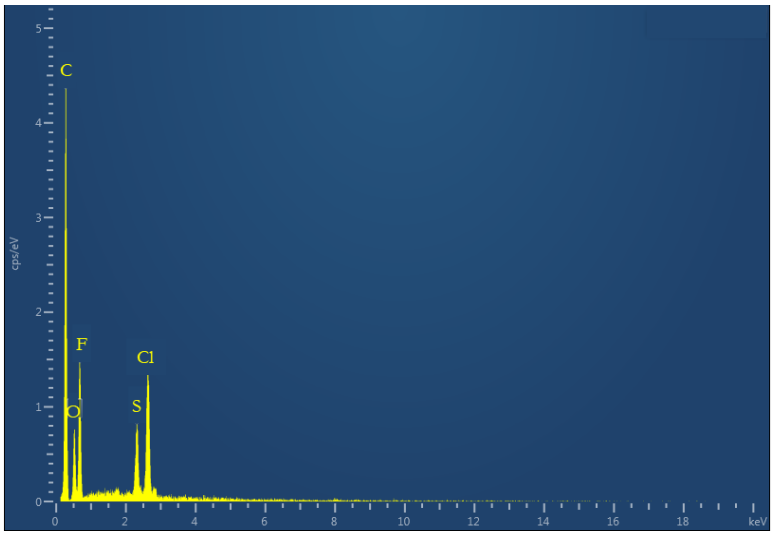

Figure 3.17. The EDAX spectrum of the CNTF interlayer after 200 cycles at 1 C rate.

In order to have a visual proof of the role of the CNTF interlayer in trapping the polysulfides, the morphology of the interlayer was examined before and after carrying out the charge-discharge cycling process. The FE-SEM image of the CNTF interlayer before cycling is shown in figure 3.16a and the inset displays its enlarged version. The image of the free standing and flexible CNTF interlayer displays interconnected carbon nanotubes which are randomly aligned with a porous structure. The porous nature of the interlayer is beneficial in two different ways. It allows an easy pathway for the electrolyte to permeate through the layer. The porous CNTF layer can trap the migrating polysulfides species and retain them within the cathode region. The FE-SEM image of the CNTF interlayer after 200 charge-discharge cycles is given in figure 3.16b and the inset shows the enlarged image. The morphology of the interlayer after cycling is quite different from that of the interlayer before cycling. The pores of the interlayer have

almost disappeared after cycling as they have been blocked by the precipitate. The agglomeration found in the interlayer after cycling indicates the trapping of the migrating polysulfides from the cathode region. The EDAX elemental distribution pattern shown in figure 3.17 confirms the nature of the precipitate that blocks the pores of the CNTF interlayer. It is clear that the precipitate contains elemental sulfur which further supports the entry of the polysulfides and their accumulation in the interlayer. The CNTF interlayer thus suppresses the polysulfide shuttle phenomenon and effectively improves the electrochemical activity of the Li-S cells.[110]

3.4 Conclusions

In the present work, the coconut shell derived, steam activated carbon, treated with HF to achieve maximum purity (AC), is used as the material to make the composite with sulfur to serve as the composite cathode ACS. The free-standing and flexible film of acid-functionalized carbon nanotubes, termed as the CNTF is used as the interlayer to be inserted between the composite cathode and the separator. The novelty of the present work is concerned with the Li-S cell configuration adopted, consisting of the ACS composite cathode and the CNTF interlayer as the cathode assembly. The adoption of this type of cathode assembly is a cost-effective approach, since the AC sample is obtained from the bio product, coconut shell and the steam activation and washing procedures can be done using easily available chemicals. The CNTF interlayer is obtained by the acid functionalization of carbon nanotubes and the subsequent solution casting. The acid functionalization is expected to remove the cytotoxic effects of the carbon nanotubes and enhance their dispersion and biocompatibility. The porous surface morphology of the activated carbon helps in the effective impregnation

of the sulfur particles within the pores and enhances the contact between sulfur and the activated carbon to achieve good electrical conductivity and also to minimize the adverse effects of the volume expansion of sulfur during lithium intake. However, the use of the ACS composite cathode alone is not sufficient to achieve high cell capacity and excellent cycling stability, due to the bad effects of the inherent problem of the polysulfide shuttling phenomenon. In the present work, the use of the flexible CNTF interlayer inserted between the ACS cathode and the separator is found to generate miraculous effects of enhancing the cell capacity almost three times compared to the values obtained without using the CNTF interlayer. The interlayer effectively stimulates the performance of the cells by providing much higher discharge capacity and excellent cycling stability. With the CNTF interlayer, the assembled Li-S cells deliver an initial discharge capacity of 542 mA h g^{-1} at a current rate of 1 C with a capacity retention of 71% after 200 cycles. The drastic improvement in the activity of the cells with the CNTF interlayer is due to the effective trapping of the migrating polysulfides within the cathode region and thus hindering the polysulfide shuttling process and also by reducing the charge transfer resistance of the composite sulfur cathode by providing the conductive network of the carbon nanotubes. The improvement in electrical conductivity at the cathode-electrolyte interface ensures better utilization of the cathode material to upgrade the cell performance. The present design of the cathode assembly consisting of the ACS composite cathode and the CNTF interlayer offers a cost-effective and rather benign approach for developing the next-generation rechargeable Li-S cells with high capacity and excellent cycling stability.

References

[1] Jacobson, M. Z. Review of Solutions to Global Warming, Air Pollution, and Energy Security. *Energy Environ. Sci.* **2009**, *2*, 148–173.

[2] Wang, J. G.; Xie, K.; Wei, B. Advanced Engineering of Nanostructured Carbons for Lithium-Sulfur Batteries. *Nano Energy* **2015**, *15*, 413–444.

[3] Seh, Z. W.; Sun, Y.; Zhang, Q.; Cui, Y. Designing High-Energy Lithium–sulfur Batteries. *Chem. Soc. Rev.* **2016**, *45*, 5605–5634.

[4] Chu, S.; Majumdar, A. Opportunities and Challenges for a Sustainable Energy Future. *Nature* **2012**, *488*, 294–303.

[5] Armand, M.; Tarascon, J.-M. Building Better Batteries. *Nature* **2008**, *451*, 652–657.

[6] Wu, S.; Ge, R.; Lu, M.; Xu, R.; Zhang, Z. Graphene-Based Nano-Materials for Lithium-Sulfur Battery and Sodium-Ion Battery. *Nano Energy* **2015**, *15*, 379–405.

[7] Yang, Y.; Yu, G.; Cha, J. J.; Wu, H.; Vosgueritchian, M.; Yao, Y.; Bao, Z.; Cui, Y. Improving the Performance of Lithium-Sulfur Batteries by Conductive Polymer Coating. *ACS Nano* **2011**, *5*, 9187–9193.

[8] Whittingham, M. S. Lithium Batteries and Cathode Materials. *Chem. Rev.* **2004**, *104*, 4271–4301.

[9] Tarascon, J. M.; Armand, M. Issues and Challenges Facing Rechargeable Lithium Batteries. *Nature* **2001**, *414*, 359–367.

[10] Ji, X.; Lee, K. T.; Nazar, L. F. A Highly Ordered Nanostructured Carbon–sulphur Cathode for Lithium–sulphur Batteries. *Nat. Mater.* **2009**, *8*, 500–506.

[11] Kim, K. R.; Lee, K.-S.; Ahn, C.-Y.; Yu, S.-H.; Sung, Y.-E. Discharging a Li-S Battery with Ultra-High Sulphur Content Cathode Using a Redox Mediator. *Sci. Rep.* **2016**, *6*, 32433.

[12] Bruce, P. G.; Freunberger, S. A.; Hardwick, L. J.; Tarascon, J.-M. Li–O_2 and Li–S Batteries with High Energy Storage. *Nat. Mater.* **2011**, *11*, 172–172.

[13] Lin, Z.; Liang, C. Lithium–sulfur Batteries: From Liquid to Solid Cells. *J. Mater. Chem. A* **2015**, *3*, 936–958.

[14] Yang, Y.; Zheng, G.; Cui, Y. Nanostructured Sulfur Cathodes. *Chem. Soc. Rev.* **2013**, *42*, 3018.

[15] Wang, A.; Xu, G.; Ding, B.; Chang, Z.; Wang, Y.; Dou, H.; Zhang, X. Highly Conductive and Lightweight Composite Film as Polysulfide Reservoir for High-Performance Lithium Sulfur Batteries. *Chem ElectroChem* **2017**, *4*, 362–368.

[16] Carbone, L.; Greenbaum, G.; Hassoun, J. Sustainable Energy & Fuels Lithium Sulfur and Lithium Oxygen Batteries : New. *Sustain. Energy Fuels* **2017**, *1*, 228–247.

[17] Ji, X.; Nazar, L. F. Advances in Li–S Batteries. *J. Mater. Chem.* **2010**, *20*, 9821.

[18] Li, Z.; Huang, Y.; Yuan, L.; Hao, Z.; Huang, Y. Status and Prospects in Sulfur-Carbon Composites as Cathode Materials for Rechargeable Lithium-Sulfur Batteries. *Carbon N. Y.* **2015**, *92*, 41–63.

[19] Manthiram, A.; Fu, Y.; Su, Y. S. Challenges and Prospects of Lithium-Sulfur Batteries. *Acc. Chem. Res.* **2013**, *46*, 1125–1134.

[20] Yan, J.; Liu, X.; Qi, H.; Li, W.; Zhou, Y.; Yao, M.; Li, B. High-Performance Lithium-Sulfur Batteries with a Cost-Effective Carbon Paper Electrode and High Sulfur-Loading. *Chem. Mater.* **2015**, *27*, 6394–6401.

[21] Jeong, T.-G.; Chun, J.; Cho, B.-W.; Lee, J.; Kim, Y.-T. Enhanced Performance of Sulfur-Infiltrated Bimodal Mesoporous Carbon Foam by Chemical Solution Deposition as Cathode Materials for Lithium Sulfur Batteries. *Sci. Rep.* **2017**, *7*, 42238.

[22] Wang, J.; Xie, K.; Wei, B. Advanced Engineering of Nanostructured Carbons for Lithium – Sulfur Batteries. *Nano Energy* **2015**, *15*, 413–444.

[23] Xiong, S.; Xie, K.; Diao, Y.; Hong, X. Oxidation Process of Polysulfides in Charge Process for Lithium-Sulfur Batteries. *Ionics (Kiel).* **2012**, *18*, 867–872.

[24] Mikhaylik, Y. V.; Akridge, J. R. Polysulfide Shuttle Study in the Li/S Battery System. *J. Electrochem. Soc.* **2004**, *151*, A1969.

[25] Li, H.; Sun, M.; Zhang, T.; Fang, Y.; Wang, G. Improving the Performance of PEDOT-PSS Coated Sulfur@activated Porous Graphene Composite Cathodes for Lithium–sulfur Batteries. *J. Mater. Chem. A* **2014**, *2*, 18345–18352.

[26] Manthiram, A.; Fu, Y.; Chung, S.; Zu, C.; Su, Y. Rechargeable Lithium − Sulfur Batteries. *Chem. Rev.* **2014**, *114*, 11751–11787.

[27] Li, W.; Zheng, G.; Yang, Y.; Seh, Z. W.; Liu, N.; Cui, Y. High-Performance Hollow Sulfur Nanostructured Battery Cathode through a Scalable, Room Temperature, One-Step, Bottom-up Approach. *Proc. Natl. Acad. Sci.* **2013**, *110*, 7148–7153.

[28] Ma, L.; Hendrickson, K. E.; Wei, S.; Archer, L. A. Nanomaterials : Science and Applications in the Lithium-Sulfur Battery. *Nano Today* **2015**, 1–24.

[29] Fu, K.; Li, Y.; Dirican, M.; Chen, C.; Lu, Y.; Zhu, J.; Li, Y.; Cao, L.; Bradford, P. D.; Zhang, X. Sulfur Gradient-Distributed CNF Composite: A Self-Inhibiting Cathode for Binder-Free Lithium–sulfur Batteries. *Chem. Commun.* **2014**, *50*, 10277.

[30] Wu, F.; Magasinski, A.; Yushin, G. Nanoporous Li_2 S and MWCNT-Linked Li_2S Powder Cathodes for Lithium-Sulfur and Lithium-Ion Battery Chemistries. *J. Mater. Chem. A* **2014**, *2*, 6064–6070.

[31] Lee, J. T.; Zhao, Y.; Thieme, S.; Kim, H.; Oschatz, M.; Borchardt, L.; Magasinski, A.; Cho, W. Il; Kaskel, S.; Yushin, G. Sulfur-Infiltrated Micro- and Mesoporous Silicon Carbide-Derived Carbon Cathode for High-Performance Lithium Sulfur Batteries. *Adv. Mater.* **2013**, *25*, 4573–4579.

[32] Jin, F.; Xiao, S.; Lu, L.; Wang, Y. Efficient Activation of High-Loading Sulfur by Small CNTs Confined Inside a Large CNT for High-Capacity and High-Rate Lithium-Sulfur Batteries. *Nano Lett.* **2016**, *16*, 440–447.

[33] Zeng, S.-Z.; Yao, Y.; Zeng, X.; He, Q.; Zheng, X.; Chen, S.; Tu, W.; Zou, J. A Composite of Hollow Carbon Nanospheres and Sulfur-Rich Polymers for Lithium-Sulfur Batteries. *J. Power Sources* **2017**, *357*, 11–18.

[34] Li, W.; Zhang, Q.; Zheng, G.; Seh, Z. W.; Yao, H.; Cui, Y. Understanding the Role of Different Conductive Polymers in Improving the Nanostructured Sulfur Cathode Performance. *Nano Lett.* **2013**, *13*, 5534–5540.

[35] Yin, L.; Wang, J.; Lin, F.; Yang, J.; Nuli, Y. Polyacrylonitrile/Graphene Composite as a Precursor to a Sulfur-Based Cathode Material for High-Rate Rechargeable Li–S Batteries. *Energy Environ. Sci.* **2012**, *5*, 6966.

[36] Angulakshmi, N.; Stephan, A. M. Efficient Electrolytes for Lithium Sulfur Batteries. *Front. Energy Res.* **2015**, *3*, 1–8.

[37] Dirlam, P. T.; Park, J.; Simmonds, A. G.; Domanik, K.; Arrington, C. B.; Schaefer, J. L.; Oleshko, V. P.; Kleine, T. S.; Char, K.; Glass, R. S.; Soles, C. L.; Kim, C.; Pinna, N.; Sung, Y. E.; Pyun, J. Elemental Sulfur and Molybdenum Disulfide Composites for Li-S Batteries with Long Cycle Life and High-Rate Capability. *ACS Appl. Mater. Interfaces* **2016**, *8*, 13437–13448.

[38] Su, Y.-S.; Manthiram, A. A New Approach to Improve Cycle Performance of Rechargeable Lithium–Sulfur Batteries by Inserting a Free-Standing MWCNT Interlayer. *Chem. Commun.* **2012**, *48*, 8817.

[39] Huang, J. Q.; Zhang, Q.; Wei, F. Multi-Functional Separator/Interlayer System for High-Stable Lithium-Sulfur Batteries: Progress and Prospects. *Energy Storage Mater.* **2015**, *1*, 127–145.

[40] Huang, J. Q.; Xu, Z. L.; Abouali, S.; Akbari Garakani, M.; Kim, J. K. Porous Graphene Oxide/Carbon Nanotube Hybrid Films as Interlayer for Lithium-Sulfur Batteries. *Carbon N. Y.* **2016**, *99*, 624–632.

[41] Vizintin, A.; Lozinšek, M.; Chellappan, R. K.; Foix, D.; Krajnc, A.; Mali, G.; Drazic, G.; Genorio, B.; Dedryvère, R.; Dominko, R.; Balach, J.; Jaumann, T.; Klose, M.; Oswald, S.; Eckert, J.; Giebeler, L.; Yuan, Z.; Peng, H. J.; Hou, T. Z.; Huang, J. Q.; Chen, C. M.; Wang, D. W.; Cheng, X. B.; Wei, F.; Zhang, Q. Fluorinated Reduced Graphene Oxide as an Interlayer in Li-S Batteries. *Nano Lett.* **2015**, *119*, 519–527.

[42] Balach, J.; Jaumann, T.; Klose, M.; Oswald, S.; Eckert, J.; Giebeler, L. Mesoporous Carbon Interlayers with Tailored Pore Volume as Polysulfide Reservoir for High-Energy Lithium - Sulfur Batteries. *J. Phys. Chem. C* **2015**, *119*, 4580–4587.

[43] Yuan, Z.; Peng, H. J.; Hou, T. Z.; Huang, J. Q.; Chen, C. M.; Wang, D. W.; Cheng, X. B.; Wei, F.; Zhang, Q. Powering Lithium-Sulfur Battery Performance by Propelling Polysulfide Redox at Sulfiphilic Hosts. *Nano Lett.* **2016**, *16*, 519–527.

[44] Manoj, M.; Jasna, M.; Anilkumar, K. M.; Abhilash, A.; Jinisha, B.; Pradeep, V. S. Sulfur-Polyaniline Coated Mesoporous Carbon Composite in Combination with Carbon Nanotubes Interlayer as a Superior Cathode Assembly for High Capacity Lithium-Sulfur Cells. *Appl. Surf. Sci.* **2018**, *458*, 751–761.

[45] He, N.; Zhong, L.; Xiao, M.; Wang, S.; Han, D.; Meng, Y. Foldable and High Sulfur Loading 3D Carbon Electrode for High-Performance Li-S Battery Application. *Sci. Rep.* **2016**, *6*, 33871.

[46] Yuan, L.; Yuan, H.; Qiu, X.; Chen, L.; Zhu, W. Improvement of Cycle Property of Sulfur-Coated Multi-Walled Carbon Nanotubes Composite Cathode for Lithium/Sulfur Batteries. *J. Power Sources* **2009**, *189*, 1141–1146.

[47] Han, S.-C.; Song, M.-S.; Lee, H.; Kim, H.-S.; Ahn, H.-J.; Lee, J.-Y. Effect of Multiwalled Carbon Nanotubes on Electrochemical Properties of Lithium/Sulfur Rechargeable Batteries. *J. Electrochem. Soc.* **2003**, *150*, A889.

[48] Wang, H.; Yang, Y.; Liang, Y.; Robinson, J. T.; Li, Y.; Jackson, A.; Cui, Y.; Dai, H. Graphene-Wrapped Sulfur Particles as a Rechargeable Lithium-Sulfur Battery Cathode Material with High Capacity and Cycling Stability. *Nano Lett.* **2011**, *11*, 2644–2647.

[49] Gao, X.; Li, J.; Guan, D.; Yuan, C. A Scalable Graphene Sulfur Composite Synthesis for Rechargeable Lithium Batteries with Good Capacity and Excellent Columbic Efficiency. *ACS Appl. Mater. Interfaces* **2014**, *6*, 4154–4159.

[50] Zhao, M.-Q.; Zhang, Q.; Huang, J.-Q.; Tian, G.-L.; Nie, J.-Q.; Peng, H.-J.; Wei, F. Unstacked Double-Layer Templated Graphene for High-Rate Lithium–sulphur Batteries. *Nat. Commun.* **2014**, *5*, 1–8.

[51] Chen, K.; Cao, J.; Lu, Q.; Wang, Q.; Yao, M.; Han, M.; Niu, Z.; Chen, J. Sulfur Nanoparticles Encapsulated in Reduced Graphene Oxide Nanotubes for Flexible Lithium-Sulfur Batteries. *Nano Res.* **2017**, *1*, 1–13.

[52] Liu, F.; Liang, J.; Zhang, C.; Yu, L.; Zhao, J.; Liu, C.; Lan, Q.; Chen, S.; Cao, Y.; Zheng, G. Results in Physics Reduced Graphene Oxide Encapsulated Sulfur Spheres for the Lithium- Sulfur Battery Cathode. *Results Phys.* **2017**, *7*, 250–255.

[53] Moon, S.; Jung, Y. H.; Kim, D. K. Enhanced Electrochemical Performance of a Crosslinked Polyaniline-Coated Graphene Oxide-Sulfur Composite for Rechargeable Lithium-Sulfur Batteries. *J. Power Sources* **2015**, *294*, 386–392.

[54] Anilkumar, K. M.; Jinisha, B.; Manoj, M.; Pradeep, V. S.; Jayalekshmi, S. Layered Sulfur/PEDOT:PSS Nano Composite Electrodes for Lithium Sulfur Cell Applications. *Appl. Surf. Sci.* **2018**, *442*, 556–564.

[55] Liang, X.; Wen, Z.; Liu, Y.; Zhang, H.; Jin, J.; Wu, M.; Wu, X. A Composite of Sulfur and Polypyrrole-Multi Walled Carbon Combinatorial Nanotube as Cathode for Li/S Battery. *J. Power Sources* **2012**, *206*, 409–413.

[56] Liu, X.; Huang, J.-Q.; Zhang, Q.; Mai, L. Nanostructured Metal Oxides and Sulfides for Lithium-Sulfur Batteries. *Adv. Mater.* **2017**, *29*, 1601759.

[57] Li, Y.; Cai, Q.; Wang, L.; Li, Q.; Peng, X.; Gao, B.; Huo, K.; Chu, P. K. Mesoporous TiO_2 Nanocrystals/Graphene as an Efficient Sulfur Host Material for High-Performance Lithium-Sulfur Batteries. *ACS Appl. Mater. Interfaces* **2016**, *8*, 23784–23792.

[58] Wang, S.; Yang, Z.; Zhang, H.; Tan, H.; Yu, J.; Wu, J. Mesoporous-MnO_2/Sulfur Composite as Cathode Material for Li-S Batteries. *Electrochim. Acta* **2013**, *106*, 307–311.

[59] Deng, J.; Li, M.; Wang, Y. Biomass-Derived Carbon: Synthesis and Applications in Energy Storage and Conversion. *Green Chem.* **2016**, *18*, 4824–4854.

[60] Wang, J.; Nie, P.; Ding, B.; Dong, S.; Hao, X.; Dou, H.; Zhang, X. Biomass Derived Carbon for Energy Storage Devices. *J. Mater. Chem. A* **2017**, *5*, 2411–2428.

[61] Jain, A.; Aravindan, V.; Jayaraman, S.; Kumar, P. S.; Balasubramanian, R.; Ramakrishna, S.; Madhavi, S.; Srinivasan, M. P. Activated Carbons Derived from Coconut Shells as High Energy Density Cathode Material for Li-Ion Capacitors. *Sci. Rep.* **2013**, *3*, 1–6.

[62] Su, Y.-S.; Manthiram, A. Lithium–sulphur Batteries with a Microporous Carbon Paper as a Bifunctional Interlayer. *Nat. Commun.* **2012**, *3*, 1166.

[63] Tan, J. M.; Arulselvan, P.; Fakurazi, S.; Ithnin, H.; Hussein, M. Z. A Review on Characterizations and Biocompatibility of Functionalized Carbon Nanotubes in Drug Delivery Design. *J. Nanomater.* **2014**, *2014,* 917024.

[64] Dong, C.; Campell, A. S.; Eldawud, R.; Perhinschi, G.; Rojanasakul, Y.; Zoica, C. Effects of Acid Treatment on Structure , Properties and Biocompatibility of Carbon Nanotubes. *Appl. Surf. Sci.* **2013**, *264*, 261–268.

[65] Tian, Z.; Shi, Y.; Yin, M.; Shen, H.; Jia, N. Functionalized Multiwalled Carbon Nanotubes- Anticancer Drug Carriers : Synthesis , Targeting Ability and Antitumor Activity. *Nano Biomed Eng* **2011,** *3,* 157–162.

[66] Dennis, V. A.; Singh, S. R. Functionalized Carbon Nanotubes : Biomedical Applications. *Int. J. Nanomedicine* **2012**, 5361–5374.

[67] Ashraf, C. M.; Anilkumar, K. M.; Jinisha, B.; Manoj, M.; Pradeep, V. S.; Jayalekshmi, S. Acid Washed, Steam Activated, Coconut Shell Derived Carbon for High Power Supercapacitor Applications. *J. Electrochem. Soc.* **2018**, *165*, A900–A909.

[68] Kim, H. S.; Jeong, C. S.; Kim, Y. T. Shuttle Inhibitor Effect of Lithium Perchlorate as an Electrolyte Salt for Lithium-Sulfur Batteries. *J. Appl. Electrochem.* **2012**, *42*, 75–79.

[69] Wang, W.; Wang, Y.; Huang, Y.; Huang, C.; Yu, Z.; Zhang, H.; Wang, A.; Yuan, K. The Electrochemical Performance of Lithium-Sulfur Batteries with $LiClO_4$ DOL/DME Electrolyte. *J. Appl. Electrochem.* **2010**, *40*, 321–325.

[70] Wang, Y.; Yokoi, T.; Namba, S.; Tatsumi, T. Effects of Dealumination and Desilication of Beta Zeolite on Catalytic Performance in N-Hexane Cracking. *Catalysts* **2016**, *6*, 8.

[71] Lv, M.; Xie, W.; Sun, S.; Wu, G.; Zheng, L.; Chu, S.; Gao, C.; Bao, J. *Activated-Carbon-Supported K–Co–Mo Catalysts for Synthesis of Higher Alcohols from Syngas*; *Catal. Sci. Technol.***2015**, *5*, 2925–2934.

[72] Jäckel, N.; Weingarth, D.; Schreiber, A.; Krüner, B.; Zeiger, M.; Tolosa, A.; Aslan, M.; Presser, V. Performance Evaluation of Conductive Additives for Activated Carbon Supercapacitors in Organic Electrolyte. *Electrochim. Acta* **2016**, *191*, 284–298.

[73] Pradeep, V. S.; Ayana, D. G.; Graczyk-Zajac, M.; Soraru, G. D.; Riedel, R. High Rate Capability of SiOC Ceramic Aerogels with Tailored Porosity as Anode Materials for Li-Ion Batteries. *Electrochim. Acta* **2015**, *157*, 41–45.

[74] Shang, H.; Lu, Y.; Zhao, F.; Chao, C.; Zhang, B.; Zhang, H. Preparing High Surface Area Porous Carbon from Biomass by Carbonization in a Molten Salt Medium. *RSC Adv.* **2015**, *5*, 75728–75734.

[75] Ghosh Chaudhuri, R.; Paria, S. Visible Light Induced Photocatalytic Activity of Sulfur Doped Hollow TiO_2 Nanoparticles, Synthesized via a Novel Route. *Dalt. Trans.* **2014**, *43*, 5526–5534.

[76] Kim, J. H.; Fu, K.; Choi, J.; Kil, K.; Kim, J.; Han, X.; Hu, L.; Paik, U. Encapsulation of S/SWNT with PANI Web for Enhanced Rate and Cycle Performance in Lithium Sulfur Batteries. *Sci. Rep.* **2015**, *5*, 1–6.

[77] Ponraj, R.; Kannan, A. G.; Ahn, J. H.; Lee, J. H.; Kang, J.; Han, B.; Kim, D. W. Effective Trapping of Lithium Polysulfides Using a Functionalized Carbon Nanotube-Coated Separator for Lithium-Sulfur Cells with Enhanced Cycling Stability. *ACS Appl. Mater. Interfaces* **2017**, *9*, 38445–38454.

[78] Geng, H.-Z.; Kim, K. K.; So, K. P.; Lee, Y. S.; Chang, Y.; Lee, Y. H. Effect of Acid Treatment on Carbon Nanotube-Based Flexible Transparent Conducting Films. *J. Am. Chem. Soc.* **2007**, *129*, 7758–7759.

[79] Yang, X.; Zhu, W.; Cao, G.; Zhao, X. Preparation of a Carbon Nanofibers–carbon Matrix–sulfur Composite as the Cathode Material of Lithium–sulfur Batteries. *RSC Adv.* **2016**, *6*, 7159–7171.

[80] Cheng, Y.; Ji, S.; Xu, X.; Liu, J. Wheat Straw Carbon Matrix Wrapped Sulfur Composites as a Superior Cathode for Li–S Batteries. *RSC Adv.* **2015**, *5*, 100089–100096.

[81] Wang, Y.-X.; Huang, L.; Sun, L.-C.; Xie, S.-Y.; Xu, G.-L.; Chen, S.-R.; Xu, Y.-F.; Li, J.-T.; Chou, S.-L.; Dou, S.-X.; Sun, S.-G. Facile Synthesis of a Interleaved Expanded Graphite-Embedded Sulphur Nanocomposite as Cathode of Li–S Batteries with Excellent Lithium Storage Performance. *J. Mater. Chem.* **2012**, *22*, 4744.

[82] Zeng, Q. (Ray); Wang, D.-W.; Wu, K.-H.; Li, Y.; Condi de Godoi, F.; Gentle, I. R. Synergy of Nanoconfinement and Surface Oxygen in Recrystallization of Sulfur Melt in Carbon Nanocapsules and the Related Li–S Cathode Properties. *J. Mater. Chem. A* **2014**, *2*, 6439.

[83] Zhang, S.; Li, N.; Lu, H.; Zheng, J.; Zang, R.; Cao, J. Improving Lithium–sulfur Battery Performance via a Carbon-Coating Layer Derived from the Hydrothermal Carbonization of Glucose. *RSC Adv.* **2015**, *5*, 50983–50988.

[84] Ji, X.; Lee, K. T.; Nazar, L. F. A Highly Ordered Nanostructured Carbon–sulphur Cathode for Lithium–sulphur Batteries. *Nat. Mater.* **2009**, *8,* 500-6.

[85] Cosmidis, J.; Templeton, A. S. Self-Assembly of Biomorphic Carbon/Sulfur Microstructures in Sulfidic Environments. *Nat. Commun.* **2016**, *7,* 12812.

[86] Zhang, B.; Qin, X.; Li, G. R.; Gao, X. P. Enhancement of Long Stability of Sulfur Cathode by Encapsulating Sulfur into Micropores of Carbon Spheres . *Energy Environ. Sci.* **2010**, *3*, 1531–1537.

[87] Bhandari, S.; Deepa, M.; Joshi, A. G.; Saxena, A. P.; Srivastava, A. K. Revelation of Graphene-Au for Direct Write Deposition and Characterization. *Nanoscale Res. Lett.* **2011**, *6*, 2–8.

[88] Kumari, S.; Kumar A. ; Singh, A. P. ; Garg, M. Cu – Ni Alloy Decorated Graphite Layers for EMI Suppression. *RSC Adv.* **2014**, *4,* 23202–23209.

[89] Takahashi, T.; Yamagata, M.; Ishikawa, M. A Sulfur–microporous Carbon Composite Positive Electrode for Lithium/Sulfur and Silicon/Sulfur Rechargeble Batteries. *Prog. Nat. Sci. Mater. Int.* **2015**, *25*, 612–621.

[90] Tang, Z.; Jiang, J.; Liu, S.; Chen, L.; Liu, R.; Zheng, B.; Fu, R.; Wu, D. Polyaniline-Coated Activated Carbon Aerogel/Sulfur Composite for High- Performance Lithium-Sulfur Battery. *Nanoscale Res. Lett.* **2017**, *12,* 617 .

[91] Guo, J.; Xu, Y.; Wang, C. Sulfur-Impregnated Disordered Carbon Nanotubes Cathode for Lithium-Sulfur Batteries. *Nano Lett.* **2011**, *11*, 4288–4294.

[92] Fu, Y.; Manthiram, A. Core-Shell Structured Sulfur-Polypyrrole Composite Cathodes for Lithium-Sulfur Batteries. *RSC Adv.* **2012**, *2*, 5927.

[93] Zhou, G.; Yin, L. C.; Wang, D. W.; Li, L.; Pei, S.; Gentle, I. R.; Li, F.; Cheng, H. M. Fibrous Hybrid of Graphene and Sulfur Nanocrystals for High-Performance Lithium-Sulfur Batteries. *ACS Nano* **2013**, *7*, 5367–5375.

[94] Zhang, S. S. Role of $LiNO_3$ in Rechargeable Lithium/Sulfur Battery. *Electrochim. Acta* **2012**, *70*, 344–348.

[95] Zhang, S. S. Liquid Electrolyte Lithium/Sulfur Battery: Fundamental Chemistry, Problems, and Solutions. *J. Power Sources* **2013**, *231*, 153–162.

[96] Rosenman, A.; Elazari, R.; Salitra, G.; Markevich, E.; Aurbach, D.; Garsuch, A. The Effect of Interactions and Reduction Products of $LiNO_3$, the Anti-Shuttle Agent, in Li-S Battery Systems. *J. Electrochem. Soc.* **2015**, *162*, A470–A473.

[97] Rosenman, A.; Elazari, R.; Salitra, G.; Markevich, E.; Aurbach, D. The Effect of Interactions and Reduction Products of $LiNO_3$, the Anti-Shuttle Agent, in Li-S Battery Systems. *J. Electrochem. Soc.* **2015**, *162*, 470–473.

[98] Poux, T.; Nov, P.; Trabesinger, S. Pitfalls in Li-S Rate-Capability Evaluation. *J. Electrochem. Soc.* **2016**, *163,* A1139-A1145.

[99] Zhang, T.; Marinescu, M.; Walus, S.; Kovacik, P.; Offer, G. J. What Limits the Rate Capability of Li-S Batteries during Discharge : Charge Transfer or Mass Transfer ? *J. Electrochem. Soc.* **2018**, *165*, 6001–6004.

[100] Singhal, R.; Chung, S.-H.; Manthiram, A.; Kalra, V. A Free-Standing Carbon Nanofiber Interlayer for High-Performance Lithium–sulfur Batteries. *J. Mater. Chem. A* **2015**, *3*, 4530–4538.

[101] Eatemadi, A.; Daraee, H.; Karimkhanloo, H.; Kouhi, M.; Zarghami, N.; Akbarzadeh, A.; Abasi, M.; Hanifehpour, Y.; Joo, S. W. Carbon Nanotubes: Properties, Synthesis, Purification, and Medical Applications. *Nanoscale Res. Lett.* **2014**, *9*, 1–13.

[102] Singh, S.; Vardharajula, S.; Tiwari, P.; Erdal Eroğlu; Komal Vig; Dennis, V.; Ali. Functionalized Carbon Nanotubes: Biomedical Applications. *Int. J. Nanomedicine* **2012**, *7*, 5361–5374.

[103] Letters, E. M.; Texas, P. B.; Texas, A. M.; Texas, P. M. Poromechanical Effect in the Lithium- Sulfur Battery Cathode. *Extrem. Mech. Letetrs* **2016**, *9*, 359–370.

[104] Cai, Y.; Guo, Y.; Jiang, B.; Lv, Y. Encapsulation of Cathode in Lithium-Sulfur Batteries with a Novel Two-Dimensional Carbon Allotrope: DHP-Graphene. *Sci. Rep.* **2017**, *7*, 1–7.

[105] Li, Y.; Yuan, L.; Li, Z.; Qi, Y.; Wu, C.; Liu, J.; Huang, Y. Improving the Electrochemical Performance of a Lithium–Sulfur Battery with a Conductive Polymer-Coated Sulfur Cathode. *RSC Adv.* **2015**, *5*, 44160–44164.

[106] Zhou, W.; Yu, Y.; Chen, H.; Disalvo, F. J. Yolk − Shell Structure of Polyaniline-Coated Sulfur for Lithium-Sulfur Batteries. *J. Am. Chem. Soc.* **2013**, No. 135, 16736–16743.

[107] Liang, X.; Zhang, M.; Rejaul, M.; Gao, X.; Konstantinov, K.; Tandiono, R.; Wang, Z.; Dou, S.; Wang, J. Split-Half-Tubular Polypyrrole @ Sulfur @ Polypyrrole Composite with a Novel. *Nano Energy* **2014**, *11*, 587-599

[108] Chung, S. H.; Manthiram, A. Lithium-Sulfur Batteries with Superior Cycle Stability by Employing Porous Current Collectors. *Electrochim. Acta* **2013**, *107*, 569–576.

[109] Yuan, L.; Qiu, X.; Chen, L.; Zhu, W. New Insight into the Discharge Process of Sulfur Cathode by Electrochemical Impedance Spectroscopy. *J. Power Sources* **2009**, *189*, 127–132.

[110] Qin, F.; Zhang, K.; Fang, J.; Lai, Y.; Li, Q.; Zhang, Z.; Li, J. High Performance Lithium Sulfur Batteries with a Cassava-Derived Carbon Sheet as a Polysulfides Inhibitor. *New J. Chem.* **2014**, *38*, 4549–4554.

4

Sulfur-polyaniline coated mesoporous carbon composite in combination with carbon nanotubes interlayer as a superior cathode assembly for high capacity lithium-sulfur cells

The present chapter illustrates the modified attempts undertaken to improve the electrochemical performance of the assembled Li-S cells, the details of which are discussed in the previous chapter. The cathode assembly described in the third chapter consists of the composite of sulfur with acid washed, steam activated carbon and the interlayer of functionalized carbon nanotubes inserted between the cathode and the separator. With a view to improve the capacity and the cycling stability of the Li-S cells further towards commercial standards, the sulfur cathode is modified by making composite with highly conducting polyaniline (PANI) coated mesoporous carbon and the flexible interlayer of carbon nanotubes (CNT interlayer) is inserted between the cathode and the separator to complete the cathode assembly. These modifications effected on the sulfur cathode and the quite laudable improvements observed in the assembled Li-S cell performance, form the central theme of this chapter.

4.1 Introduction

The urge for resorting to pollution free and renewable energy harvesting strategies and the need for developing efficient storage systems for storing the generated energy have already been outlined in detail in the previous chapter. The meritorious aspects of the lithium-sulfur cell technology for realizing the next generation energy storage devices and the inherent limitations of this technology that delay its commercialization have also been deliberated in the earlier section. As mentioned before, the additional modifications carried out on the cathode assembly to improve the capacity, rate capability and the cycling performance of the Li-S cells, form the vital theme of the present chapter. The surface modification of sulfur cathode is carried out using the combination of the conducting polymer, polyaniline (PANI) and mesoporous carbon (MC). The composite of sulfur with the PANI coated mesoporous carbon (SPMC) is used as the modified sulfur cathode. The mesoporous carbon (MC) is an inexpensive and highly conductive carbon material which can significantly improve the electrical conductivity of the sulfur cathode. The high surface area and pore volume of MC facilitate the effective confining of sulfur particles within its pores. The electrically conducting polymer PANI is extensively used to improve the electrochemical properties of various energy storage devices including rechargeable cells, supercapacitors and fuel cells owing to its ease of synthesis, environmental stability and relatively high electrical conductivity.[1,2] Interestingly, the PANI in the SPMC composite ensures better utilization of sulfur by intensifying the contact between sulfur and the MC and ascertains excellent control over the volume expansion of sulfur during lithium intake.[3] The flexible film

of multi walled carbon nanotubes, termed as the CNT interlayer, inserted between the SPMC composite cathode and the separator helps in preventing the dissolution of sulfur in the form of polysulfides into the electrolyte and hinders the polysulfide shuttle phenomenon and thereby improves the cycle life and performance of the Li-S cells.[4] A comparative study of the working of the assembled Li-S cells with and without the CNT interlayer has been carried out. The results reveal that the effective modification of the sulfur cathode using PANI and MC and the presence of the interlayer significantly improve the electrochemical performance of the assembled cells. Our group has recently reported the studies on Li-S cells assembled using the PEDOT:PSS coated sulfur as the modified cathode, without carbon and the CNT interlayer.[5] The conducting polymer PEDOT:PSS is however much expensive than polyaniline and requires more complex procedures for storing and handling. In the present approach, attempts have been carried out to replace PEDOT:PSS with polyaniline and mesoporous carbon and introduce the CNT interlayer to achieve higher capacity and better performance characteristics. It is satisfactory to see that, quite impressive cell performance and much better cycling stability could be achieved through the modifications effected on the sulfur cathode.

4.2 Experimental

4.2.1 Materials

The chemicals used for the synthesis of the SPMC composite were of analytical grade. Aniline was purified by vacuum distillation to remove impurities before use. Mesoporous carbon, ammonium persulfate, hydrochloric acid, and sulfur were used as received.

4.2.2 Synthesis of PANI coated mesoporous carbon composite (PMC)

The PMC composite was synthesized by in-situ polymerization of aniline on the surface of mesoporous carbon (MC). The MC was dispersed in 50 ml, 1 M HCl solution with ultrasonication for 3 hours. The monomer aniline was then added to the above solution and again ultrasonicated for 2 hours followed by stirring for another 2 hours to get a uniform dispersion of the MC in aniline - HCl solution. The solution of the oxidant, ammonium persulfate in 50 ml, 1 M HCl solution was added drop wise to the MC-aniline - HCl solution under stirring in an ice-bath. The mixture was stirred for 12 hours. Finally, the product was carefully filtered with distilled water and then with acetone to obtain the PMC composite. After filtration, the sample was dried to yield the final PMC powder sample.

4.2.3 Synthesis of sulfur-PMC (SPMC) composite

Solvothermal approach was employed for the synthesis of the SPMC composite. The synthesized PMC composite and finely powdered sulfur were mixed at a weight ratio of 2:8 in 30 ml acetone. The above dispersion was first ultrasonicated for 3 hours and then stirred for another 24 hours at room temperature. After the stirring was completed the mixture was transferred to an autoclave and then subjected to solvothermal treatment for 4 hours at a temperature of 120 °C. After the completion of the solvothermal process, the autoclave was allowed to cool to room temperature and the resulting mixture was filtered thoroughly using deionized water. The product obtained after filtration was dried at 60 °C under vacuum to obtain the final SPMC composite.

The schematic representation of synthesis of SPMC composite is shown in the figure 4.1.

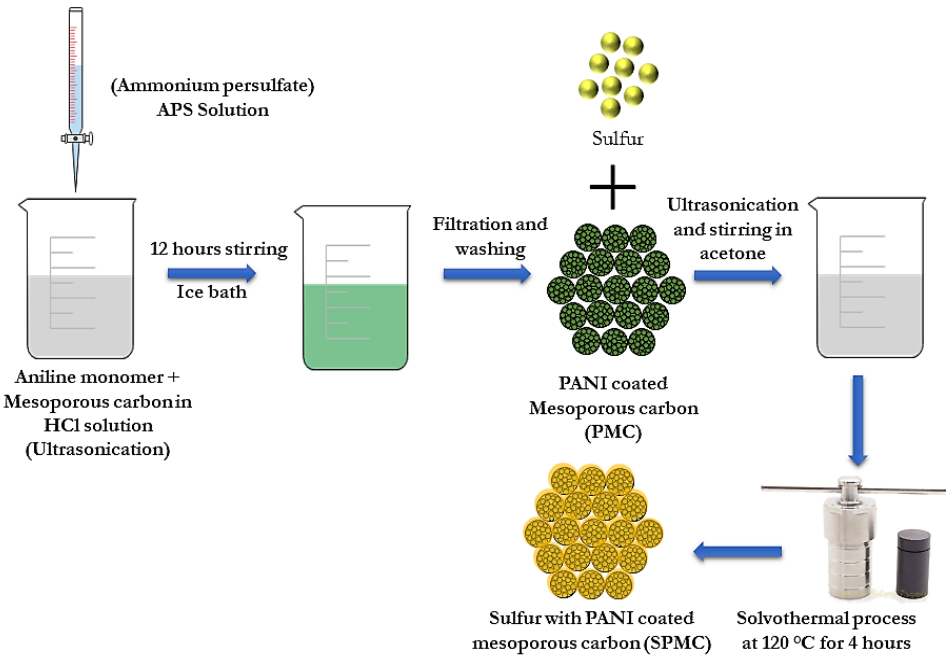

Figure 4.1. Schematic representation of the synthesis of SPMC composite.

4.2.4 Synthesis of free-standing interlayer of carbon nanotubes (CNT interlayer)

The commercially obtained multi-walled carbon nanotubes (CNTs) powder was added to N-methyl-2-pyrrolidone (NMP) solution and kept for ultra-sonication for 3 hours to get a uniform dispersion of CNTs in NMP**.** The material, polyvinylidene fluoride (PVDF) was dissolved in NMP and this solution was mixed with the above CNTs dispersion and again ultra-sonicated for 3 hours. Here, PVDF is used as the host polymer for CNTs because the low molecular weight and the durability

of PVDF are suitable to cast thin films in the desired thickness range.[6,7] The resulting solution was poured into a teflon petri-dish and kept for drying in a vacuum oven at 60 °C for 12 hours. Free standing and flexible CNTs films were peeled off the petri-dish and punched into small discs of 10 mm diameter, 0.2 mm thickness and 4-6 mg weight to serve as the CNT interlayers and were used for further investigations. The schematic representation of the synthesis of the CNT interlayer and the configuration of the Li-S cells with the interlayer in between the separator and the SPMC cathode are illustrated in figures 4.2a and 4.2b respectively.

4.2.5 Structural and morphological characterization

The structural characterization of the SPMC composite was carried out by X-ray diffraction technique employing the PANalytical X'Pert Pro machine with Cu-Kα radiation of wavelength 1.542 Å. The surface morphological features of the composite were studied using the Carl Zeiss Sigma, field emission scanning electron microscope (FE-SEM). High-resolution transmission electron microscope (HR-TEM) images were taken on a Joel/JEM-2100 machine. Thermogravimetric analyzer (Perkin Elmer, Diamond TG/DTA) under nitrogen atmosphere was employed to determine the sulfur content in the composite and the heating rate used was 10 °C min^{-1}.

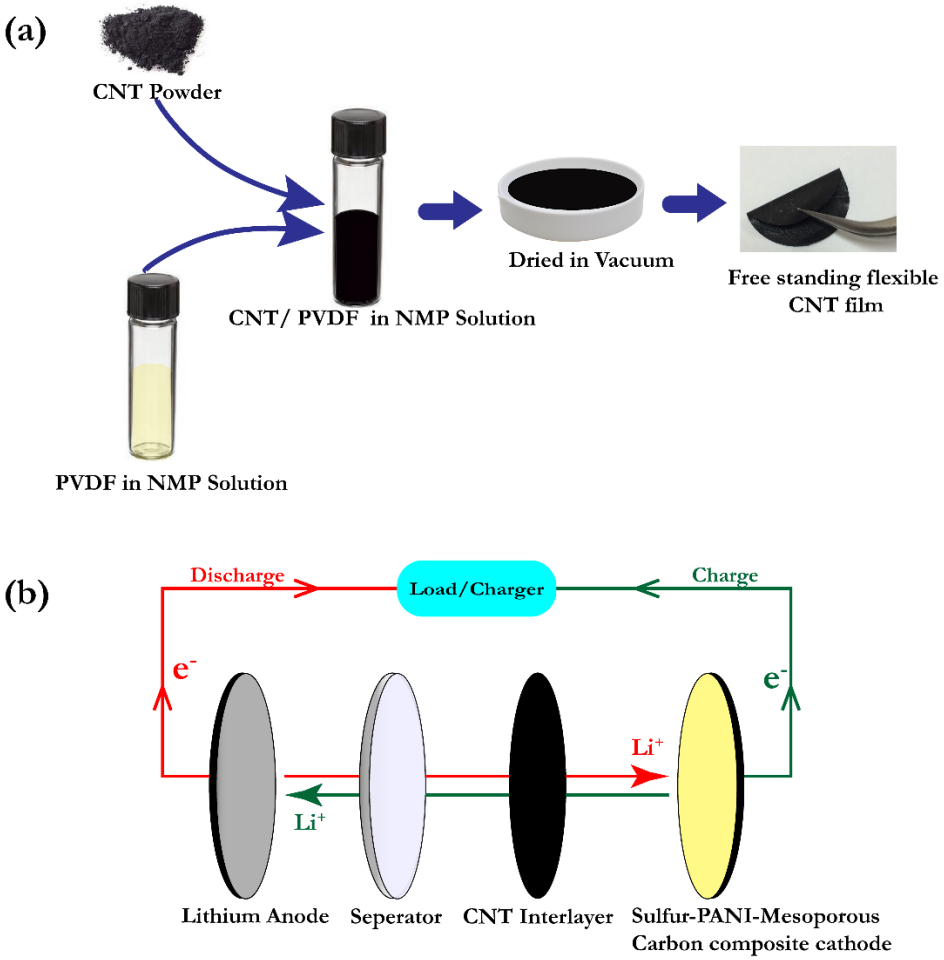

Figure 4.2. Schematic representation of (a) the synthesis of the CNT interlayer and (b) the configuration of the Li-S cell with the CNT interlayer

4.2.6 Electrochemical studies

The cathode electrodes for Li-S cells were made by mixing 80 wt.% of the SPMC composite material with 10 wt.% of acetylene black as the conducting medium and 10 wt.% of polyvinylidene difluoride

(PVDF) in N-methyl-2-pyrrolidone (NMP) solvent. The homogeneous slurry thus obtained was coated on a thin aluminum foil by spray coating and was allowed to dry at 60 °C overnight under vacuum. Circular disks of diameter 10 mm were cut from the coated aluminum foil and used as active cathode electrodes. The mass of sulfur in each piece of the circular disc was kept approximately at 1.3 mg cm^{-2}. The electrochemical characterizations were carried out by assembling stainless steel Swagelok cells in an argon-filled glove box. The electrolyte used was 1 M $LiClO_4$ in a mixed solvent of 1,3-dioxolane (DOL) and 1, 2-dimethoxyethane (DME) at a volume ratio of 1:1 including 0.5 M $LiNO_3$ as an electrolyte additive.[8,9] Lithium metal was used as the counter/reference electrode and Celgard was used as the separator. The synthesized CNT interlayer was placed between the separator and the SPMC cathode and the electrolyte of volume around 70 μl was added to each cell. The cyclic voltammetry (CV) and the electrochemical impedance spectroscopy (EIS) studies were carried out using the Bio-Logic SP300 workstation. The CV test was carried out at a scan rate of 0.1 mV s^{-1} in the voltage window of 1.5-3 V. The EIS data was recorded in the frequency range between 1 MHz and 10 mHz at open-circuit voltage (OCV). The galvanostatic charge-discharge test of the assembled Li-S cells was carried out at various C-rates (1 C=1650 mA g^{-1}) using the 8 channel battery analyzer (MTI Corporation-USA) in the potential window of 1.5-3 V.[10–13]

4.3 Results and discussion

4.3.1 X-ray diffraction (XRD) analysis

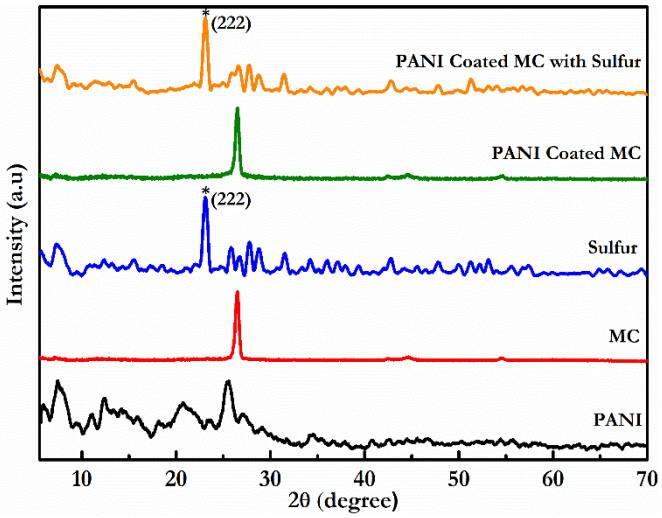

Figure 4.3. XRD patterns of PANI, MC, Sulfur, PANI coated MC and the sulfur composite with PANI coated MC.

The XRD patterns of PANI, MC, Sulfur, PANI coated MC, and the sulfur composite with PANI coated MC, are shown in figure 4.3. For PANI, characteristic diffraction peaks are observed at 12°, 20° and 25°, in agreement with the previously reported data in the literature.[14] The XRD pattern of MC shows a sharp peak at 26° which remains intact in the PMC composite, with reduced intensity, confirming that the polymer coating does not affect the structure of MC and no new phase is formed during the in-situ oxidative polymerization process. In the XRD pattern of sulfur, several sharp diffraction peaks are observed in the 15° to 60° range, representing the orthorhombic structure and the dominant peak at 23.1° is attributed to the (222) crystal plane of

sulfur.[13,15] In the case of the SPMC composite, the diffraction peaks of sulfur are obvious while that of MC is not obvious due to the high degree of crystallization of sulfur and relatively high content of sulfur in the composite.[16]

4.3.2 FE-SEM, TEM and EDAX analysis

The TEM and FE-SEM techniques were employed to investigate the surface morphology of the synthesized samples and the images are shown in figure 4.4. The FE-SEM image of PANI (figure 4.4a) shows rod-like structure with random stacking morphology. The FE-SEM image of MC shown in figure 4.4b shows micro-beads like structure. The TEM images of the PMC composite, shown in figure 4.4c and 4.4d, clearly show the PANI coating on the surface of MC which is also evident from the FE-SEM image of the composite shown in figure 4.4e. The conducting polymer coating can improve the electrical conductivity of sulfur by strengthening the interaction between sulfur and MC and thereby ensuring better utilization of the sulfur cathode. Thus, the PANI coated MC composite acts as the conducting framework for hosting sulfur particles. Elemental mapping of the PMC composite is carried out to confirm the distribution of carbon and is shown in figure 4.4f. The presence of elements such as oxygen and sulfur, observed in the elemental mapping of the PMC composite shown in figure 4.4g and 4.4h, arises from the oxidant, ammonium persulfate used in the polymerization of aniline and further confirms the existence of PANI on the surface of MC.[17]

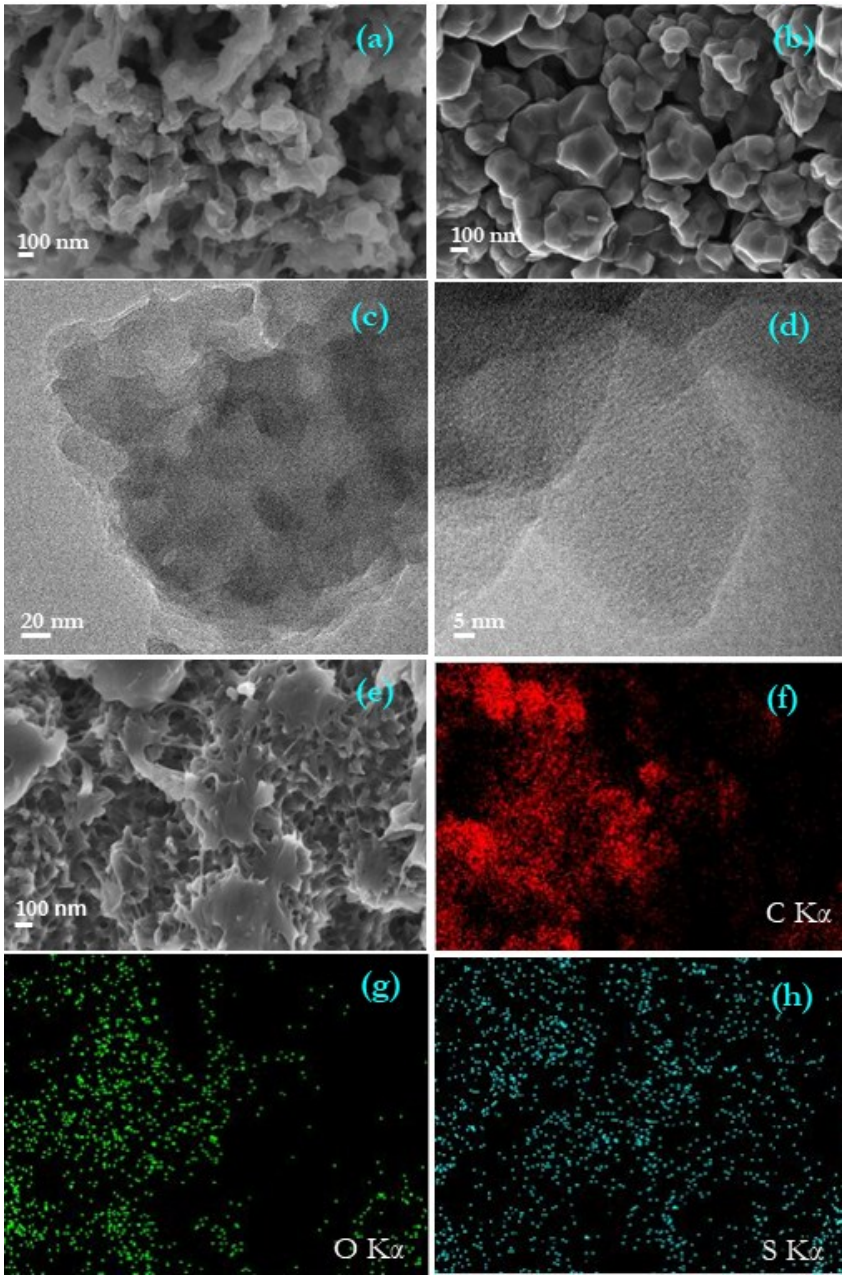

Figure 4.4. FE-SEM images of (a) PANI, (b) MC, TEM images of (c and d) PMC, FE-SEM image of (e) PMC and the elemental mapping of (f) carbon, (g) oxygen and (h) sulfur.

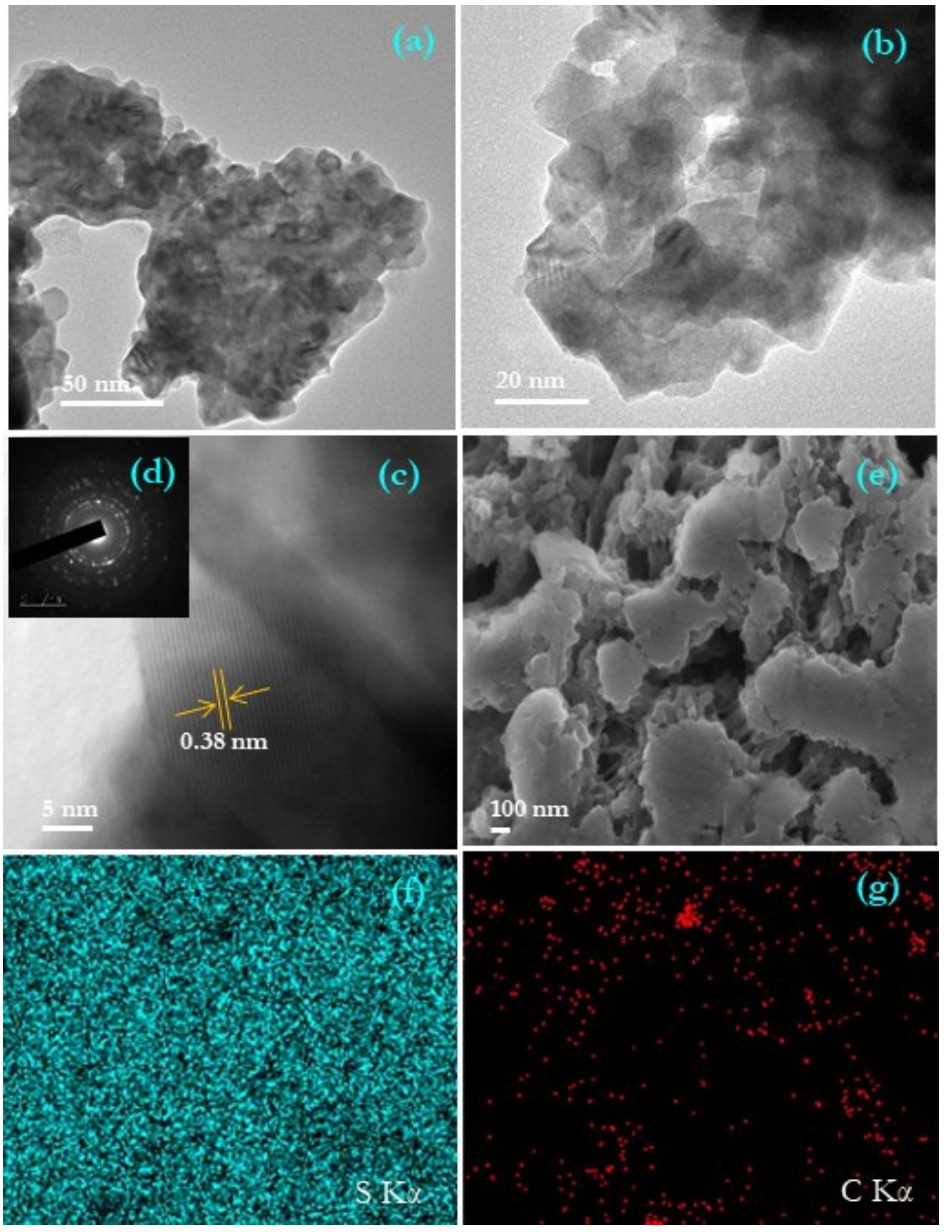

Figure 4.5. The morphological features of the SPMC composite observed by (a-c) TEM images, (d) SAED pattern, (e) FE-SEM image and (f-g) elemental mapping.

The TEM images of the SPMC composite obtained after the solvothermal treatment of sulfur with the PMC composite are shown in figure 4.5(a-c). The TEM images, shown in figure 4.5a and 4.5b, indicate that the sulfur particles are uniformly distributed and attached to the conductive network structure formed by the PMC composite. The crystalline nature of sulfur particles is clearly visible in the HR-TEM image shown in figure 4.5c. The clear lattice fringes observed with an interlayer spacing of 0.38 nm in the HR-TEM image, correspond to the (222) plane, in excellent correlation with the XRD pattern of sulfur, in which the (222) plane shows the highest intensity.[18] The selected area electron diffraction (SAED) pattern of the SPMC composite shown in figure 4.5d can be indexed to the contribution of the polycrystalline sulfur particles.[19] The FE-SEM image of the SPMC composite, shown in figure 4.5e reveals that most of the sulfur particles get encapsulated within the PMC composite during the heat treatment and the rest of the particles aggregates on the surface of the PMC composite. The elemental mapping of SPMC composite shown in figure 4.5f and 4.5g, confirms the presence of sulfur and carbon in the composite as well as the homogenous distribution of sulfur particles in the conducting framework of the PMC composite.

4.3.3 Thermogravimetric (TGA) analysis

The content of sulfur in the SPMC composite was determined from the thermo-gravimetric analysis. The TGA plots of sulfur, MC, PANI, PMC and the SPMC composite are shown in figure 4.6. The plot of pure sulfur shows that the complete weight loss of sulfur occurs at around 330 °C and that of MC shows the highest thermal stability as the

decomposition happens above 600 °C. [20] The thermal decomposition of PANI matches with the previous reports and the PMC composite exhibits thermal properties similar to those of PANI.[21]

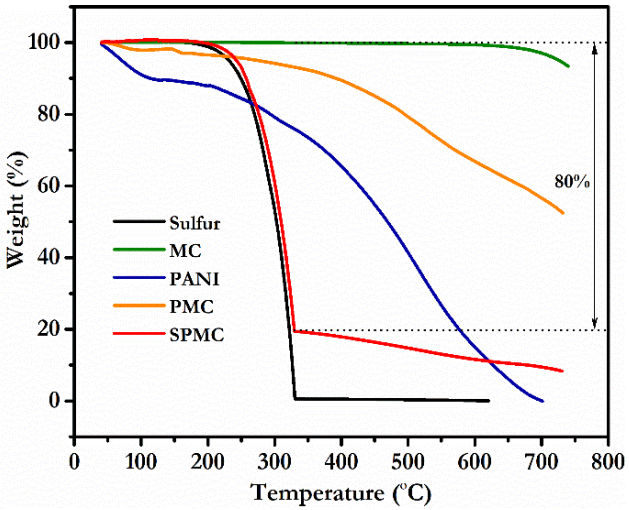

Figure 4.6. TGA curves of PANI, sulfur, MC, PMC and SPMC composite.

The similarity between the TGA curves of sulfur and the SPMC composite indicates that decrease in the mass of the composite takes place due to the loss of sulfur from the composite and the remaining mass corresponds to that of the PMC composite.[16] Based on the TGA analysis, the sulfur content in the SPMC composite is calculated to be about 80 wt.%.

4.3.4 Electrochemical analysis

4.3.4.a Cyclic voltammetry (CV) analysis

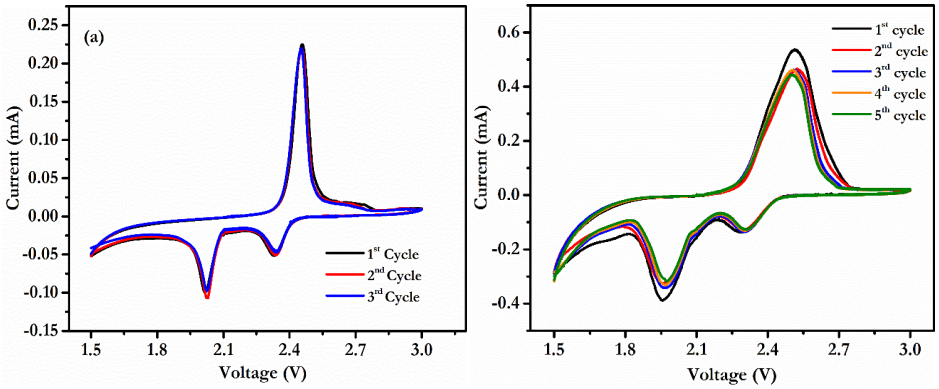

Figure 4.7. CV curves of Li-S cells (a) without and (b) with the CNT interlayer at 0.1 mV s^{-1}.

The cyclic voltammetry (CV) curves of the Li-S cells assembled without and with the CNT interlayer are shown in figures 4.7a and 4.7b respectively. Both the CV curves show two reduction peaks and one oxidation peak consistent with the typical behavior of sulfur cathodes. In the case of the Li-S cell with the CNT interlayer inserted between the sulfur cathode and the separator, an increase in the redox currents are observed, which indicates better utilization of the sulfur cathode material. No additional redox peaks are observed in the CV curve after the insertion of the interlayer, showing the inactive nature of the interlayer towards contributing to the final storage capacity of the Li-S cell.[4] In the cathodic scan, the peak at 2.3 V represents the reduction of sulfur to soluble, higher order lithium polysulfides (Li_2S_n, $4 \leq n \leq 8$) and the second reduction peak at 2.0 V can be related to the further reduction of the higher order lithium polysulfides to the lower order, insoluble Li_2S_2 and ultimately to Li_2S.[22] In the anodic scan, the oxidation peak at 2.45 V is attributed to the conversion

of Li_2S_2/Li_2S to polysulfides and sulfur.[23] There is a slight shift and broadening of the redox peaks for the cells with the CNT interlayer. This is due to the rapid conversion between the polysulfides and sulfur, credited to the good electrical conductivity of the CNT interlayer, acting as a pseudo-upper current collector and improving the overall conductivity of the sulfur composite cathode.[11] The slight over potential observed in the initial cathodic and anodic peaks for the cells with the interlayer disappears after the first cycle, perhaps due to the rearrangement of the active material to electrochemically favorable positions.[10] After the first cycle, the peaks overlap and are well positioned indicating reversibility in the following four cycles.

4.3.4.b Charge-discharge studies

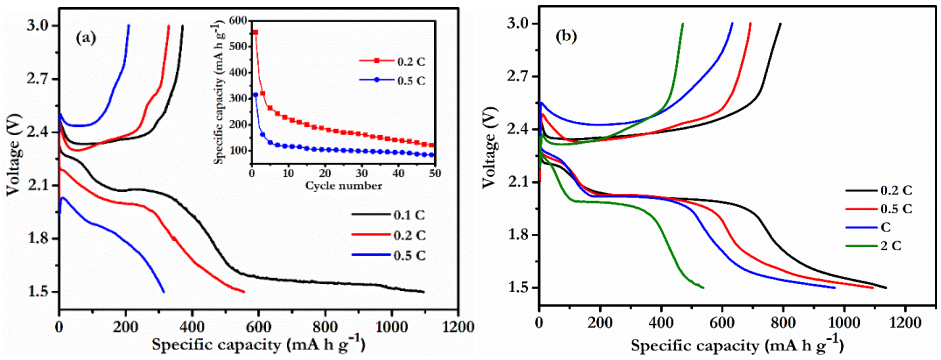

Figure 4.8. Charge-discharge profiles of Li-S cells (a) without the CNT interlayer and the inset shows the cycling data at rates of 0.2 C and 0.5 C and (b) with the CNT interlayer at various C-rates.

The charge-discharge profiles of the Li-S cells without and with the CNT interlayer at various C-rates (1 C=1650 mA g^{-1}) are shown in figures 4.8a and 4.8b, respectively. The cell capacities are calculated by considering the weight of sulfur in the active cathode material. The cells without the CNT interlayer show an initial capacity of 1095 mA h g^{-1} at

0.1 C with rapid capacity fading. At higher C-rates of 0.2 C and 0.5 C, the initial discharge capacities observed are 555 mA h g^{-1} and 315 mA h g^{-1} respectively which give an indication of the weakening of the electrochemical activity in the cells. The inset of figure 4.8a shows the cycling stability curves of the Li-S cells without the CNT interlayer at the rates of 0.2 C and 0.5 C. The discharge capacities of the cells without employing the CNT interlayer are found to deteriorate sharply to below one-forth of the initial values on cycling at both the C rates, after 50 cycles. The cells with the CNT interlayer show much better electrochemical performance during the charge-discharge process with higher charge-discharge capacities. For these cells, an initial discharge capacity of 1137 mA h g^{-1} is observed at 0.2 C which corresponds to 68.9% of the theoretical capacity of sulfur. Also at higher charge-discharge current rates of 0.5 C, 1 C, and 2 C, the observed discharge capacities are 1093 mA h g^{-1}, 968 mA h g^{-1}, and 537 mA h g^{-1} respectively as shown in figure 4.8b. The voltage tails found at the end of the discharge process can be attributed to the irreversible reduction of $LiNO_3$ in the electrolyte.[11,24]

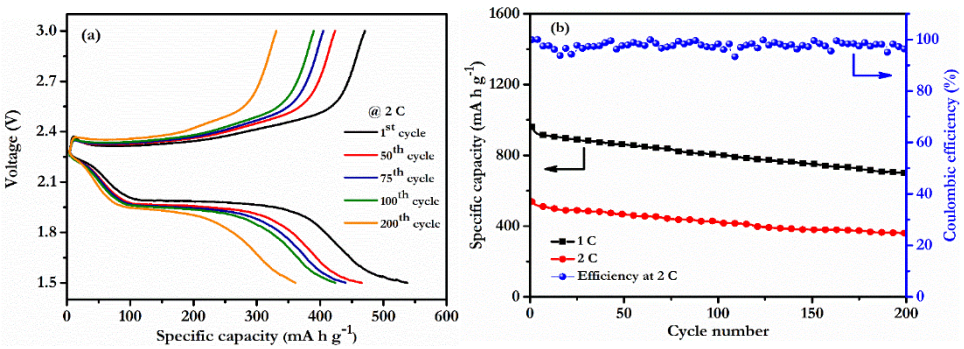

Figure 4.9. (a) Charge-discharge profiles of Li-S cells with the CNT interlayer after a number of cycles at 2 C and (b) Cycling data of Li-S cells with the CNT interlayer at higher rates of 1 C and 2 C and Coulombic efficiency at 2 C.

The extended cycling behaviour of the Li-S cells with the CNT interlayer at 2 C rate is shown in figure 4.9a. The cycling stability curves of the cells with the CNT interlayer at 1 C and 2 C rates and the Coulombic efficiency values of the cells at 2 C rate for 200 cycles are depicted in figure 4.9b. Even though the discharge capacity gets gradually decreased on increasing the cycle number for the cells with the interlayer, a capacity of 360 mA h g^{-1} is observed at the end of the 200th cycle at 2 C rate which corresponds to a capacity retention of about 67% of the initial capacity and the average Coulombic efficiency during the cycling process remains at 98%. Similarly, at 1 C rate a capacity retention of 72.3% of the initial capacity is observed in the cells with the CNT interlayer at the end of the 200th cycle corresponding to a low capacity decay of 0.14% per cycle.

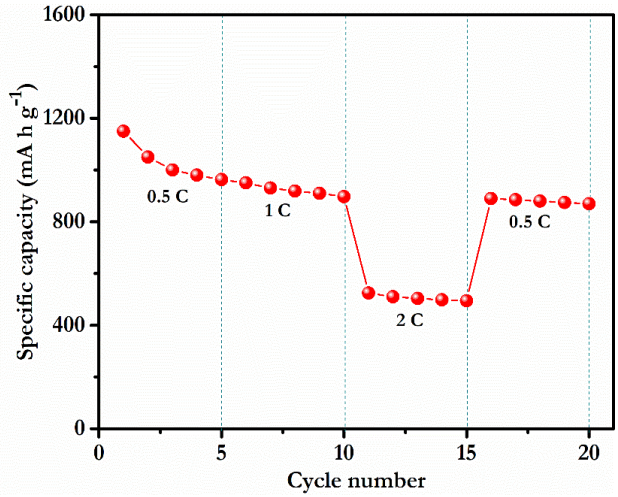

Figure 4.10. Rate capability of Li-S cells with the CNT interlayer from 0.5 C to 2 C.

The rate capability of the Li-S cells with the SPMC cathode and the CNT interlayer was evaluated at various C-rates from 0.5 C to 2 C

for 5 cycles at each C-rate and is shown in figure 4.10. The capacity fading is observed only in the first few cycles at 0.5 C and thereafter the cells display stable capacity at higher C-rate of 2 C.When the C-rate is reverted back to 0.5 C from 2 C, after 15 cycles, the discharge capacity increases to 890 mA h g^{-1}. This retention of discharge capacity even after undergoing cycling at higher C-rates indicates good compatibility between the CNT interlayer and the SPMC cathode, which facilitates the smooth transport of lithium ions, suppressing the shuttling of polysulfides across the electrodes.

From these observations, it is quite clear that the insertion of the CNT interlayer between the separator and the sulfur composite cathode significantly improves the electrochemical performance of the Li-S cells. The CNT interlayer helps in better utilization of the sulfur composite cathode material by improving the conductivity of the interface and thereby accelerating the electrochemical kinetics. This is in addition to the effects of the polyaniline coated mesoporous carbon (PMC) in improving the electrical contact and thereby enhancing the utilization of sulfur. The presence of the PMC helps in blocking the dissolution of the polysulfides in the electrolyte and the CNT interlayer facilitates the localization of the polysulfides within the cathode region and the combined effects substantially hinder the polysulfide shuttle phenomenon. As described earlier, the CNT interlayer can also act as a pseudo-upper current collector and can effectively modify the performance of the Li-S cells. The schematic representation of the prototype of the Li-S cell with the SPMC cathode in combination with the CNT interlayer in the cathode region is shown in figure 4.11.

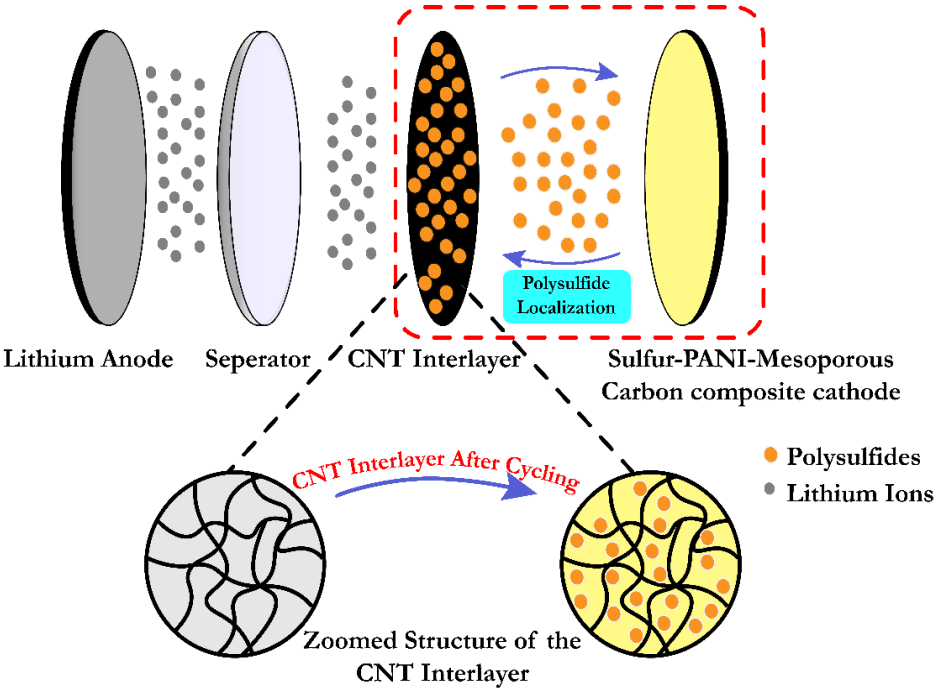

Figure 4.11. Prototype of a typical Li-S cell with the CNT interlayer in the cathode region.

4.3.4.c Electrochemical impedance spectroscopy (EIS) studies

The electrochemical impedance spectroscopy (EIS) technique was employed to study how the cathode material, the interlayer and the electrolyte influence the impedance of the assembled cells. The EIS is a powerful tool to monitor the electrochemical processes occurring in electrochemical cells during the charge-discharge process.[25] The observed Nyquist plots of the Li-S cells with and without the CNT interlayer are shown in figure 4.12. The plots show a semicircular loop at high to medium frequency region, which is related to the charge transfer resistance followed by an inclined line at the low-frequency region.[26] The charge transfer resistance (R_{ct}), generated at the interface between

the electrode and the electrolyte can be estimated from the diameter of the semicircular loop.[27,28]

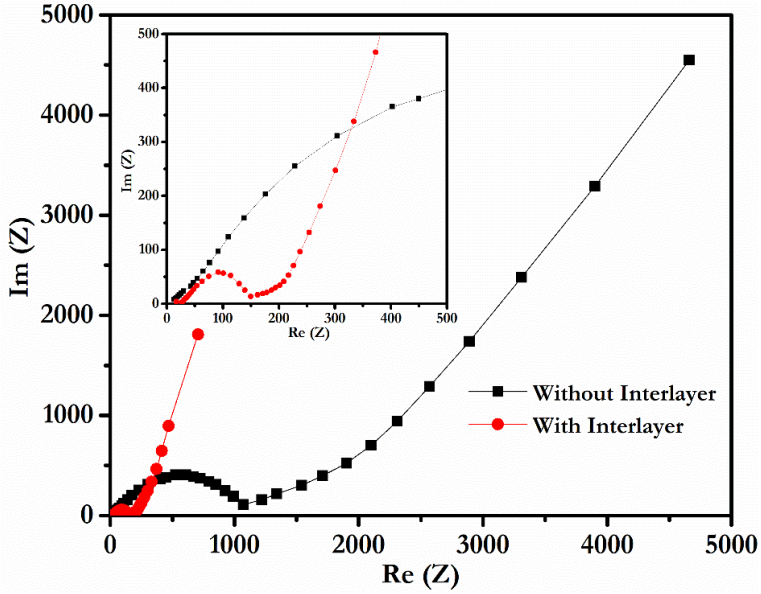

Figure 4.12. EIS data of the Li-S cells with and without the CNT interlayer.

The Li-S cell with the CNT interlayer shows a drastic decrease in R_{ct} from 1073 Ω to 150 Ω. The significant decrease in the value of R_{ct} after the insertion of the CNT interlayer is attributed to the formation of a conductive pathway for charge transfer by the highly conducting CNT interlayer.[29,30] The interlayer acts as an upper current collector, reducing the resistance of cathode material and thereby conversely enhancing the utilization of the SPMC composite cathode.[10,31,32] The presence of the interlayer improves the electrochemical environment at the cathode by allowing rapid electron transfer and efficient accessibility of the cathode material to the electrolyte[11,33] and accelerates the electrochemical kinetics taking place at the cathode. The increase in the available surface

area by the introduction of the conductive CNT matrix is the main reason for the improved electrochemical kinetics at the cathode.[34,35] The analysis of the Nyquist plots supports the excellent electrochemical performance of the Li-S cells with the CNT interlayer. In addition to the decisive role of the CNT interlayer in boosting the electrochemical activity of the Li-S cells, the thickness of the interlayer also influences the cell performance. There are previous reports that increased thickness of the interlayer can adversely affect the free movement of lithium ions across the interlayer during the cycling process which eventually leads to poor electrochemical activity in the cells.[36] In the present work, using the solution casting technique, extra care has been taken to limit the CNT layer thickness to the required levels.

4.3.5 Analysis of CNT interlayer after cycling

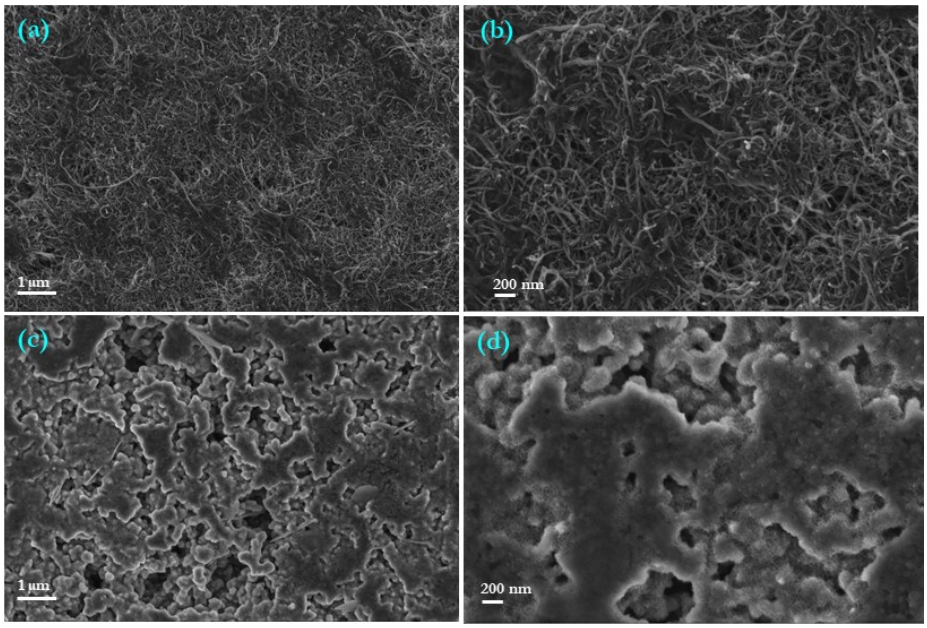

Figure 4.13. FE-SEM images of CNT interlayers: (a) and (b) before cycling and (c) and (d) after 200 cycles at 1 C rate.

To gain further insight into the capability of the CNT interlayer in improving the performance of the Li-S cells, the cells were dismantled after subjecting to 200 charge-discharge cycles and the morphology of the CNT interlayer was analysed. The FE-SEM images of the CNT interlayers before cycling are shown in figures 4.13a and 4.13b in which the CNTs are randomly aligned and cross-linked with a porous structure. The porous nature of the CNT interlayer is significant as it makes the electrolyte diffusion smoother, provides pathway for lithium-ion transport and facilitates the electrochemical reactions at the cathode. The porous structured CNT interlayer also helps in the localization of the polysulfides within the cathode region and in hindering the polysulfide shuttle phenomenon and thereby eventually improving the performance and the cycle life of the Li-S cells.[10,11] The FE-SEM images of the interlayer after being subjected to 200 charge-discharge cycles are shown in figures 4.13c and 4.13d which reveal a quite different morphology of the interlayer. Randomly aligned aggregates are observed in the CNT interlayer which block some of the pores in the interlayer. This indicates that the interlayer with CNT network is effective in obstructing and holding the migrating polysulfide species within the cathode region and thereby evading the problems of polysulfide shuttle phenomenon.[11,37,38] The design of Li-S cells with the modified sulfur cathode structure, using the SPMC as the composite cathode in combination with the CNT interlayer ensures better sulfur utilization and reduced shuttle phenomenon by the effective trapping of polysulfides and the effective control over the volume expansion of sulfur and thereby improves the overall electrochemical performance of the cells. A comparative assessment of the electrochemical performance

of the Li-S cells assembled using the two different types of cathode assembly described in the third and the present chapters, is illustrated in the table 4.1.

Table 4.1. Performance comparison of the ACS based and the SPMC based Li-S cells with the CNT interlayer.

Scan Rates	Modified sulfur cathodes			
	ACS cathode		SPMC cathode	
	Discharge (mA h g^{-1})	Charge (mA h g^{-1})	Discharge (mA h g^{-1})	Charge (mA h g^{-1})
0.05 C	1562	905	-	-
0.1 C	1378	730	-	-
0.2 C	1129	700	1137	790
0.5 C	846	674	1093	692
1 C	542	518	968	632
2 C	-	-	537	470

The table shows the performance comparison between the activated carbon-sulfur composite (ACS) based Li-S cells and the SPMC composite based Li-S cells with the CNT interlayer. The ACS composite-based cells with the CNT interlayer deliver high discharge capacity at lower C-rates compared to the SPMC composite based Li-S cells with the CNT interlayer. This is mainly due to the large surface area around 1864 m^2 g^{-1}, possessed by the activated carbon compared to that of the mesoporous carbon, around 1.5 m^2 g^{-1}, and the subsequent increase in the interfacial area between the cathode material and the electrolyte.[39,40] At higher C-rates, the SPMC composite based cells overpower the performance of the ACS composite-based ones. The former is found to offer an initial discharge capacity of 537 mA h g^{-1} at 2 C which is comparable to the discharge capacity observed for the

latter at 1 C, which is around 542 mA h g^{-1}. As detailed in the previous chapter, activated carbon possesses a hierarchical porosity nature ranging from micro-porous through meso-porous to macro-porous, with the micro-porous nature dominating the other two. The ion mobility drastically decreases in the presence of micro-pores as they create bottlenecks and the performance of the cells is adversely affected at higher C-rates. On the other hand, the meso-pores offer wider pathways for ion transport even at higher C rates and thereby help to achieve high capacitance at high C-rates. In addition, the presence of the conducting polymer PANI in the SPMC composite improves the electrical conductivity substantially and rallies the movement of electrons.

4.4 Conclusions

The use of the SPMC composite cathode, which represents the modified sulfur cathode, in combination with the free-standing and flexible CNT interlayer inserted between the SPMC cathode and the separator significantly improves the performance of the assembled Li-S cells. For the cells with the CNT interlayer, enhanced specific capacitance with extended cycling stability has been observed, compared to the cells without the interlayer. The rather uniform distribution of the sulfur particles within the conducting network of the polyaniline-mesoporous carbon (PMC) composite is quite clear from the TEM and the FE-SEM images of the SPMC composite. The presence of the conducting PMC network facilitates good electrical contact for the sulfur particles and helps to hinder the dissolution of the lithium polysulfides in the electrolyte. The polyaniline coating over sulfur particles also limits the adverse effects of the possible enormous volume expansion of sulfur during lithium intake. The FE-SEM images of the CNT interlayer after

subjecting the cells to a number of charge-discharge cycles show the evidence of the interactions between the interlayer and the lithium polysulfides. The network of the carbon nanotubes of the interlayer acts as a "storeroom" of the polysulfides by holding back the migrating polysulfides, which is evident from the piling up of particles observed in the FE-SEM images of the interlayer. By localizing the polysulfides in the cathode region, the interlayer inhibits the polysulfide shuttle phenomenon. Moreover, the conducting network of the interlayer helps in lowering the charge transfer resistance and subsequently ensuring better utilization of the sulfur composite cathode material during the cycling process.

The novelty of the present work is the introduction of the SPMC (sulfur with the polyaniline coated mesoporous carbon) composite cathode in combination with the CNT interlayer to improve the performance of the Li-S cells. Although there are previous reports based on the use of CNT interlayers, the work on the advantageous aspects of the SPMC composite cathode in combination with the CNT interlayer has not been reported earlier. Here, the sulfur cathode is effectively modified by making the composite with the polyaniline coated mesoporous carbon. The polyaniline coating with electrical conductivity in the metallic range and the conducting mesoporous carbon enhance the overall electrical conductivity of the sulfur cathode and ensure better utilization of sulfur. The polymer coating also helps in limiting the volume expansion of sulfur during Li intake, which is mandatory for the stable operation of the Li- S cells. The unique combination of the SPMC cathode, obtained by the simple technique of solvothermal synthesis and the flexible CNT interlayer, grown by the cost-effective solution casting

method is found to be quite suitable to achieve high discharge capacity at higher C rates with good cycling stability over 200 cycles for the cells. The work thus emphasizes the decisive role of the CNT interlayer, along with the effects of the surface modification of the sulfur cathode by making the composite with the PANI coated mesoporous carbon, in realizing high energy density Li-S cells with quite impressive performance features for the next generation energy storage applications.

References

[1] Manoj, M.; Anilkumar, K. M.; Jinisha, B.; Jayalekshmi, S. Polyaniline–Graphene Oxide Based Ordered Nanocomposite Electrodes for High-Performance Supercapacitor Applications. *J. Mater. Sci. Mater. Electron.* **2017**, *28,* 14323–14330.

[2] Qiao, Y.; Bao, S.; Li, C. M.; Cui, X.; Lu, Z.; Guo, J. Nanostructured Polyaniline/Titanium Fuel Cells. *ACS Nano* **2008**, *2*, 113–119.

[3] Zhao, X.; Ahn, H. J.; Kim, K. W.; Cho, K. K.; Ahn, J. H. Polyaniline-Coated Mesoporous Carbon/Sulfur Composites for Advanced Lithium Sulfur Batteries. *J. Phys. Chem. C* **2015**, *119*, 7996–8003.

[4] Han, S.-C.; Song, M.-S.; Lee, H.; Kim, H.-S.; Ahn, H.-J.; Lee, J.-Y. Effect of Multiwalled Carbon Nanotubes on Electrochemical Properties of Lithium/Sulfur Rechargeable Batteries. *J. Electrochem. Soc.* **2003**, *150*, A889.

[5] Anilkumar, K. M.; Jinisha, B.; Manoj, M.; Pradeep, V. S.; Jayalekshmi, S. Layered Sulfur/PEDOT:PSS Nano Composite Electrodes for Lithium Sulfur Cell Applications. *Appl. Surf. Sci.* **2018**, *442*, 556–564.

[6] Guo, C.; Zhou, L.; Lv, J. Effects of Expandable Graphite and Modified Ammonium Polyphosphate on the Flame-Retardant and Mechanical Properties of Wood Flour-Polypropylene Composites. *Polym. Polym. Compos.* **2013**, *2*, 449–456.

[7] Begum, S.; Kausar, A.; Ullah, H.; Siddiq, M. Potential of Polyvinylidene Fluoride/Carbon Nanotube Composite in Energy, Electronics, and Membrane Technology: An Overview. *Polym. - Plast. Technol. Eng.* **2016**, *55*, 1949–1970.

[8] Kim, H. S.; Jeong, C. S.; Kim, Y. T. Shuttle Inhibitor Effect of Lithium Perchlorate as an Electrolyte Salt for Lithium-Sulfur Batteries. *J. Appl. Electrochem.* **2012**, *42*, 75–79.

[9] Wang, W.; Wang, Y.; Huang, Y.; Huang, C.; Yu, Z.; Zhang, H.; Wang, A.; Yuan, K. The Electrochemical Performance of Lithium-Sulfur Batteries with $LiClO_4$ DOL/DME Electrolyte. *J. Appl. Electrochem.* **2010**, *40*, 321–325.

[10] Su, Y.-S.; Manthiram, A. Lithium–sulphur Batteries with a Microporous Carbon Paper as a Bifunctional Interlayer. *Nat. Commun.* **2012**, *3*, 1166.

[11] Su, Y.-S.; Manthiram, A. A New Approach to Improve Cycle Performance of Rechargeable Lithium-Sulfur Batteries by Inserting a Free-Standing MWCNT Interlayer. *Chem. Commun.* **2012**, *48*, 8817–8819.

[12] Huang, J. Q.; Xu, Z. L.; Abouali, S.; Akbari Garakani, M.; Kim, J. K. Porous Graphene Oxide/Carbon Nanotube Hybrid Films as Interlayer for Lithium-Sulfur Batteries. *Carbon N. Y.* **2016**, *99*, 624–632.

[13] Li, H.; Sun, M.; Zhang, T.; Fang, Y.; Wang, G. Improving the Performance of PEDOT-PSS Coated Sulfur@activated Porous Graphene Composite Cathodes for Lithium–Sulfur Batteries. *J. Mater. Chem. A* **2014**, *2*, 18345–18352.

[14] Varma, S. J.; Xavier, F.; Varghese, S.; Jayalekshmi, S. Synthesis and Studies of Exceptionally Crystalline Polyaniline Thin Films. *Polym. Int.* **2012**, *61*, 743–748.

[15] Ghosh Chaudhuri, R.; Paria, S. Visible Light Induced Photocatalytic Activity of Sulfur Doped Hollow TiO_2 Nanoparticles, Synthesized via a Novel Route. *Dalt. Trans.* **2014**, *43* , 5526–5534.

[16] Yang, X.; Zhu, W.; Cao, G.; Zhao, X. Preparation of Reduced Carbon-Wrapped Carbon–sulfur Composite as Cathode Material of Lithium–Sulfur Batteries. *RSC Adv.* **2015**, *5*, 93926–93936.

[17] Zhao, X.; Kim, J.-K.; Ahn, H.-J.; Cho, K.-K.; Ahn, J.-H. A Ternary Sulfur/Polyaniline/Carbon Composite as Cathode Material for Lithium Sulfur Batteries. *Electrochim. Acta* **2013**, *109*, 145–152.

[18] Li, G.; Sun, J.; Hou, W.; Jiang, S.; Huang, Y.; Geng, J. Three-Dimensional Porous Carbon Composites Containing High Sulfur Nanoparticle Content for High-Performance Lithium-Sulfur Batteries. *Nat. Commun.* **2016**, *7*, 1–10.

[19] Zhang, Y.; Gao, Z.; Song, N.; Li, X. High-Performance Supercapacitors and Batteries Derived from Activated Banana-Peel with Porous Structures. *Electrochim. Acta* **2016**, *222*, 1257–1266.

[20] Cai, J.; Bennici, S.; Shen, J.; Auroux, A. Microporous and Mesoporous Materials The Acid Base Properties of Nitrogen-Containing Mesoporous Carbon Materials. **2015**, *212*, 156–168.

[21] Joelma, M.; Cardoso, R.; Fogliato, M.; Lima, S.; Lenz, D. M. Polyaniline Synthesized with Functionalized Sulfonic Acids for Blends Manufacture. Materials Research **2007**, *10*, 425–429.

[22] Zhao, M.-Q.; Zhang, Q.; Huang, J.-Q.; Tian, G.-L.; Nie, J.-Q.; Peng, H.-J.; Wei, F. Unstacked Double-Layer Templated Graphene for High-Rate Lithium–sulphur Batteries. *Nat. Commun.* **2014**, *5*, 1–8.

[23] Zhou, G.; Yin, L. C.; Wang, D. W.; Li, L.; Pei, S.; Gentle, I. R.; Li, F.; Cheng, H. M. Fibrous Hybrid of Graphene and Sulfur Nanocrystals for High-Performance Lithium-Sulfur Batteries. *ACS Nano* **2013**, *7*, 5367–5375.

[24] Zhang, S. S. Role of $LiNO_3$ in Rechargeable Lithium/Sulfur Battery. *Electrochim. Acta* **2012**, *70*, 344–348.

[25] Canas, N. A.; Hirose, K.; Pascucci, B.; Wagner, N.; Friedrich, K. A.; Hiesgen, R. Investigations of Lithium-Sulfur Batteries Using Electrochemical Impedance Spectroscopy. *Electrochim. Acta* **2013**, *97*, 42–51.

[26] Deng, Z.; Zhang, Z.; Lai, Y.; Liu, J.; Li, J.; Liu, Y. Electrochemical Impedance Spectroscopy Study of a Lithium/Sulfur Battery: Modeling and Analysis of Capacity Fading. *J. Electrochem. Soc.* **2013**, *160*, A553–A558.

[27] Su, Y. S.; Manthiram, A. A Facile in Situ Sulfur Deposition Route to Obtain Carbon-Wrapped Sulfur Composite Cathodes for Lithium-Sulfur Batteries. *Electrochim. Acta* **2012**, *77*, 272–278.

[28] Ma, G.; Wen, Z.; Jin, J.; Lu, Y.; Rui, K.; Wu, X.; Wu, M.; Zhang, J. Enhanced Performance of Lithium Sulfur Battery with Polypyrrole Warped Mesoporous Carbon/Sulfur Composite. *J. Power Sources* **2014**, *254*, 353–359.

[29] Huang, J.; Zhang, B.; Xu, Z.; Abouali, S.; Garakani, M. A.; Huang, J.; Kim, J. Novel Interlayer Made from Fe_3C/Carbon Nano Fiber Webs for High Performance Lithium Sulfur Batteries. *J. Power Sources* **2015**, *285*, 43–50.

[30] Singhal, R.; Chung, S. H.; Manthiram, A.; Kalra, V. A Free-Standing Carbon Nanofiber Interlayer for High-Performance Lithium-Sulfur Batteries. *J. Mater. Chem. A* **2015**, *3*, 4530–4538.

[31] Huang, Y.; Zheng, M.; Lin, Z.; Zhao, B.; Zhang, S.; Yang, J.; Zhu, C.; Zhang, H.; Sun, D.; Shi, Y. Flexible Cathodes and Multifunctional Interlayers Based on Carbonized Bacterial Cellulose for High-Performance Lithium-Sulfur Batteries. *J. Mater. Chem. A* **2015**, *3*, 10910 – 10918.

[32] Balach, J.; Jaumann, T.; Klose, M.; Oswald, S.; Eckert, J.; Giebeler, L. Improved Cycling Stability of Lithium Sulfur Batteries Using a Polypropylene-Supported Nitrogen-Doped Mesoporous Carbon Hybrid Separator as Polysulfide Adsorbent. *J. Power Sources* **2016**, *303*, 317–324.

[33] Qin, F.; Zhang, K.; Fang, J.; Lai, Y.; Li, Q.; Zhang, Z.; Li, J. High Performance Lithium Sulfur Batteries with a Cassava-Derived Carbon Sheet as a Polysulfides Inhibitor. *New J. Chem.* **2014**, *38*, 4549–4554.

[34] Xu, Q.; Hu, G. C.; Bi, H. L.; Xiang, H. F. A Trilayer Carbon Nanotube/Al_2O_3/Polypropylene Separator for Lithium-Sulfur Batteries. *Ionics (Kiel).* **2015**, *21*, 981–986.

[35] Chung, S. H.; Manthiram, A. Lithium-Sulfur Batteries with Superior Cycle Stability by Employing Porous Current Collectors. *Electrochim. Acta* **2013**, *107*, 569–576.

[36] Wang, A.; Xu, G.; Ding, B.; Chang, Z.; Wang, Y.; Dou, H.; Zhang, X. Highly Conductive and Lightweight Composite Film as Polysulfide Reservoir for High-Performance Lithium Sulfur Batteries. *ChemElectroChem* **2017**, *4*, 362–368.

[37] Yoo, J.; Cho, S. J.; Jung, G. Y.; Kim, S. H.; Choi, K. H.; Kim, J. H.; Lee, C. K.; Kwak, S. K.; Lee, S. Y. COF-Net on CNT-Net as a Molecularly Designed, Hierarchical Porous Chemical Trap for Polysulfides in Lithium-Sulfur Batteries. *Nano Lett.* **2016**, *16*, 3292–3300.

[38] Qin, F.; Zhang, K.; Fang, J.; Lai, Y.; Li, Q.; Zhang, Z.; Li, J. High Performance Lithium Sulfur Batteries with a Cassava-Derived Carbon Sheet as a Polysulfides Inhibitor. *New J. Chem.* **2014**, *38*, 4549–4554.

[39] Huang, G.; Xu, S.; Lu, S.; Li, L.; Sun, H. Micro-/Nanostructured Co_3O_4 Anode with Enhanced Rate Capability for Lithium-Ion Batteries. *ACS Appl. Mater. Interfaces* **2014**, No. 6, 7236–7243.

[40] Huang, G.; Xu, S.; Cheng, Y.; Zhang, W.; Li, J.; Kang, X. NiO Nanosheets with Large Specific Surface Area for Lithium-Ion Batteries and Supercapacitors. *Int. J. Electrochem. Sci.* **2015**, *10*, 2594–2601.

5

The ordered, polyaniline-graphene oxide nanocomposite as a promising carbonaceous electrode material for high power supercapacitor applications

The present chapter deals with the attempts carried out to assess the suitability of polyaniline (PANI)-graphene oxide (GO) composite material, obtained using the simple in-situ oxidative polymerization technique, for developing supercapacitors with good performance characteristics. The structurally ordered PANI-GO nanocomposite is tested as a supercapacitor electrode by employing three-electrode configuration and also in the two electrode configuration by assembling supercapacitor test cells. The composite electrode material in three electrode configuration is found to give specific capacitance of 810 F g^{-1}, which is the highest value being reported, compared to the already available previous reports. The assembled supercapacitor test cells show high specific capacitance of 132 F g^{-1} at a high current density of 5 A g^{-1} with good capacity retention over 1000 cycles. These results highlight the significance of PANI-GO nanocomposite, grown through the simple polymerization technique employed in the present work, as a favorable electrode material in the development of high-power supercapacitors.

5.1 Introduction

The extensive usage of fossil fuels based energy sources has made a pathetic effect on our entire ecosystem due to the production of carbon dioxide as waste, which is inevitably dumped into the atmosphere. Intensive research efforts are hence focused on the development of clean and sustainable energy sources to meet the expanding needs of the society, without environmental detriment. As mentioned earlier, the clean and sustainable energy, available from the sun and the wind is not continuous and hence suitable energy storage systems are mandatory for the efficient utilization of the generated power. Supercapacitors and rechargeable batteries constitute the most efficient energy storage systems, presently available and electrochemical supercapacitors are promising types with long cycle-life and high power density.[1–3] Generally supercapacitors can be turned on instantaneously, charged quickly and they require less complicated charging circuits. They are of two types, termed as, interfacial double-layer capacitors and pseudo capacitors. Many research groups are working on the development of different types of supercapacitor electrodes based on high surface area carbon materials,[4,5] transition metal oxides,[6–9] and conducting polymers.[10] Interfacial double layer capacitance is associated with carbon-based electrode materials and pseudo capacitance with the transition metal oxides and conducting polymers based ones. Polyaniline (PANI), from the group of electrically conducting polymers, is a highly preferred supercapacitor electrode material owing to its ease of synthesis, environmental stability and tunable electrical properties.[11–13] However, PANI has relatively lower surface area, and it suffers from poor cycling stability due to the low mechanical strength during charging and discharging.[14,15] Conducting

polymer composites with carbon-based materials can be used to serve as active materials in supercapacitors to eliminate the above-mentioned limitations of conducting polymers.[16] In the present work, graphene oxide (GO) is chosen as the material to make composites with PANI. The availability of simple synthesis methods and good mechanical properties make graphene oxide, one of the most suitable,[17,18] carbon nanostructures for making composites with conducting polymers. Although GO has lower electrical conductivity compared to graphene, reduced graphene oxide and carbon nanotubes, it will be compensated by the higher electrical conductivity of PANI. The literature review of the published data on the applications of PANI-GO composite as a supercapacitor electrode provides the following observations.

Wang and co-workers[19] have reported a specific capacitance of 531 F g^{-1} at 200 mA g^{-1} current density for GO doped PANI, synthesized via in-situ polymerization of aniline. Xinlu Li group[20] has observed specific capacitance around 162 F g^{-1} at a current density of 0.1 A g^{-1} for PANI-GO composites synthesized via in-situ polymerization, which is higher than that of pure PANI and GO. Mitchell's group[21] has deposited multilayers of PANI and GO on indium tin oxide (ITO) electrode for supercapacitor application. They have observed a specific capacitance of 429 F g^{-1} for PANI-GO electrode at 1 mA discharge current in 1 M H_2SO_4 solution. The PANI-GO composite synthesized by Dayong Gui and co-workers[22] is found to exhibit a specific capacitance of 355.2 F g^{-1} at 0.5 A g^{-1} in 1 M H_2SO_4 electrolyte. Zhe-Fei Li's group[23] has developed covalently-grafted PANI-GO nanocomposites with a specific capacitance of 422 F g^{-1} at a current density of 1 A g^{-1} in 1 M H_2SO_4.

As per the previously reported publications, most of the data on the electrochemical characterization of PANI-GO composites is based on studies using aqueous electrolytes which offer a low voltage window of 1 V and limit the practical applications of the supercapacitor material. In the present work, the use of organic electrolytes helps to have a higher voltage window of 2.5 V for carrying out the electrochemical characterization of the PANI-GO composites. The simple, direct, in-situ polymerization method adopted in the present work for the synthesis of the PANI-GO composite electrode is a straight forward approach compared to the various synthesis methods mentioned in the above reported publications.

The suitability of PANI-GO composite as the active material for supercapacitor application is investigated with the aim of improving the electrochemical performance of the composite. The PANI-GO composite was prepared by in-situ oxidative polymerization of monomer aniline in the presence of GO. The structural and morphological studies of the synthesized composite were carried out using X-ray diffraction (XRD), Fourier Transform Infrared (FTIR) spectroscopy and Field Emission Scanning Electron Microscopy (FE-SEM) techniques. The electrochemical behavior of the composite was investigated with 1 M $LiClO_4$ dissolved in acetonitrile as the electrolyte in the three electrode configuration. To get more information about the potential application of PANI-GO composite as a supercapacitor electrode material, the two electrode type supercapacitors were assembled, and complete electrochemical characterization was carried out at comparatively higher current densities of 3 A g^{-1}, 4 A g^{-1} and 5 A g^{-1}. Characterization of the assembled supercapacitor test cells at higher current densities is

specifically important for assessing the high power applications of the supercapacitors.

5.2 Experimental

5.2.1 Materials

Analytical grade chemicals were used for the synthesis of PANI and GO. Aniline was vacuum distilled under reduced pressure before use to remove impurities. The chemical synthesis was carried out using distilled water.

5.2.2 Synthesis of Graphene Oxide (GO)

Modified Hummer's method was used to synthesize graphene oxide[24] from graphite powder.[25] Graphite powder (3 g) was dispersed in 120 mL of H_2SO_4, and the mixture was ultra-sonicated for two hours. It was then stirred for 30 minutes in an ice bath and potassium permanganate was added to the suspension very slowly. The rate of addition was slowly controlled to keep the reaction temperature below 20 °C. After stirring for 2 hours, the ice bath was removed, and the mixture was stirred for 10 hours at room temperature. Water was slowly added to dilute the mixture. The reaction temperature was rapidly increased to 98 °C with effervescence and the color changed to brown. The solution was finally treated with 20 mL of hydrogen peroxide, and the color changed to bright yellow. The mixture was purified using 5 % HCl and deionized water several times until the filtration was neutral. The powder obtained after filtration was ultrasonicated for one hour. Finally, graphene oxide (GO) was obtained as a gray powder after drying at 100 °C under vacuum.

5.2.3 Synthesis of PANI-GO composite

Polyaniline-graphene oxide (PANI-GO) composite was synthesized by in-situ oxidative polymerization of monomer aniline in the presence of the dispersion of GO in HCl solution. The filtered aniline was dissolved in 1 M HCl solution. The suspension of the synthesized GO in the aniline containing solution was obtained by adding GO powder to the solution and sonicating for half an hour and then vigorously stirring for another 30 minutes. During the continuous vigorous stirring in an ice-bath, the oxidant, ammonium persulfate was slowly added to the mixture. Upon the starting of the in-situ polymerization of aniline, the color was found to change to dark green. The mixture was stirred for 12 hours. The resulting powder sample was washed with distilled water and acetone repeatedly until the filtrate became colorless. The filtered sample was dried at 80 °C for 12 hours to yield the PANI-GO composite powder. The schematic representation of the synthesis of PANI-GO composite is shown in figure 5.1.

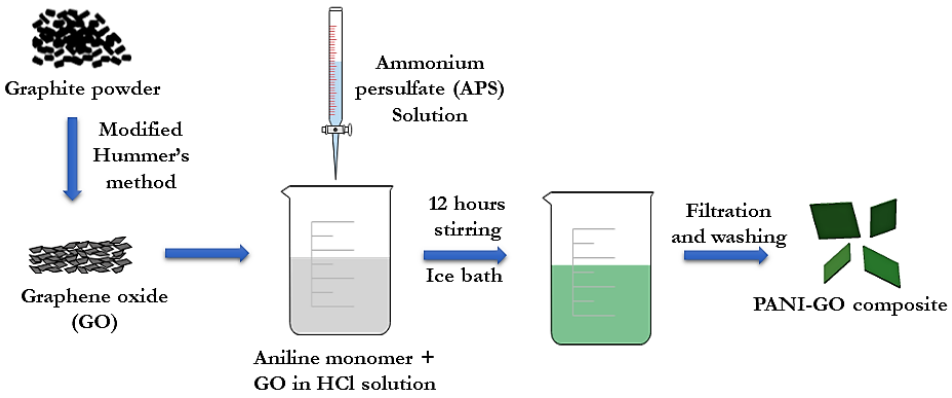

Figure 5.1. Schematic representation of the synthesis of PANI-GO composite

5.2.4 Characterization and testing

For the making of the supercapacitor electrode, the active material, PANI-GO powder, conductive carbon additive and the binder polyvinylidene fluoride (PVDF) dissolved in dimethylformamide (DMF) were mixed in the weight ratio 80:20 to make a slurry, keeping the weight percentage of the active material, PANI-GO as 80. The slurry was then uniformly coated on a stainless-steel collector and then dried at 100 °C for 10 hours in a vacuum oven.

The surface morphology of the PANI-GO composite was analyzed using the Carl Zeiss Sigma field emission scanning electron microscope. X-ray diffraction technique employing the PANalytical X'Pert Pro with Cu-Kα radiation of 1.542 Å was used for structural characterization of the composite material, followed by FTIR spectroscopy studies, using Shimadzu IR Affinity instrument.

For the electrochemical characterization of the PANI-GO composite, the three electrode cell configuration consisting of Saturated Calomel Electrode (SCE) as the reference electrode, platinum rod as the counter electrode, the prepared PANI-GO composite as the working electrode and 1 M lithium perchlorate ($LiClO_4$) dissolved in acetonitrile as the electrolyte, was used. The electrochemical tests were carried out at room temperature. The cyclic voltammetry (CV) experiment and the galvanostatic charge/discharge (GCD) test were conducted using Biologic SP 300 instrument. The cyclic voltammetry was carried out at different scanning rates from 1 mV s^{-1} to 100 mV s^{-1} between -1.5 and 1.5 V. In the three-electrode configuration, GCD test was carried out between 0 V and 1.5 V at different current density values in the range

0.2 A g^{-1} to 2 A g^{-1}. To assess the practical application of the PANI-GO composite as a supercapacitor electrode material, supercapacitor test cells were assembled. The PANI-GO active material was coated on stainless steel circular discs. The coated discs were placed one above the other with standard separator Celgard in between them, and the electrolyte was added and then the assembled discs were crimped to get sealed supercapacitor test cells. The GCD study was carried out in the potential window of 0 V to 2.5 V at different current densities of 3 A g^{-1}, 4 A g^{-1} and 5 A g^{-1}

5.3 Results and discussion

5.3.1 X- ray diffraction (XRD) analysis

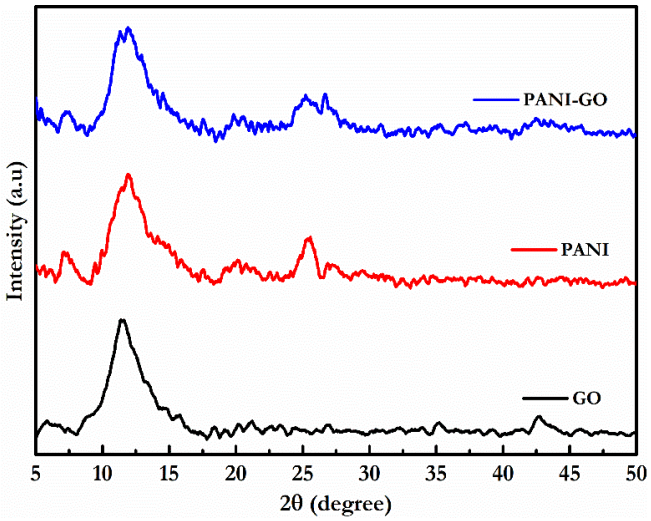

Figure 5.2. XRD patterns of pure GO, PANI and PANI-GO composite.

The XRD patterns of synthesized graphene oxide, PANI and PANI-GO composite are shown in figure 5.2. The synthesized GO shows diffraction peaks at 11.4° and 42.6° corresponding to the (002)

and (100) planes. The characteristic peaks of PANI are observed at 12°, 20° and 25°, matching with the already reported data in literature.[26] The broad XRD peaks observed for PANI indicate the semi-crystalline nature of the polymer and the same nature of the peaks observed for the PANI-GO composite confirms that the semi-crystalline nature of PANI is maintained after the in-situ polymerization to yield the PANI-GO composite.[27] The XRD pattern of PANI-GO composite shows all the characteristics peaks of both PANI and GO and no additional impurity peaks are observed.

5.3.2 Field Emission Scanning Electron Microscopy (FE-SEM) analysis

The surface morphology of the synthesized GO, PANI and the PANI-GO composite was analyzed by FE-SEM studies and the images are shown in figure 5.3. The FE-SEM image of the synthesized GO (figure 5.3a) shows a layered structure. Those of PANI and PANI-GO composite are shown in figure 5.3b and figure 5.3(c-d), respectively. The image of pure PANI shows rod-like structure with a random stacking morphology and that of PANI-GO composite exhibits the homogenous layered structure of GO with PANI rods densely aligned in an ordered manner on the surfaces of the GO sheets, which is a consequence of the template effect of GO.[28] In the PANI-GO composite formation, GO acts as a supporting material and provides sites for the nucleation and growth processes of PANI rods on the surfaces of GO sheets, resulting in an increased surface area for the PANI-GO composite material.

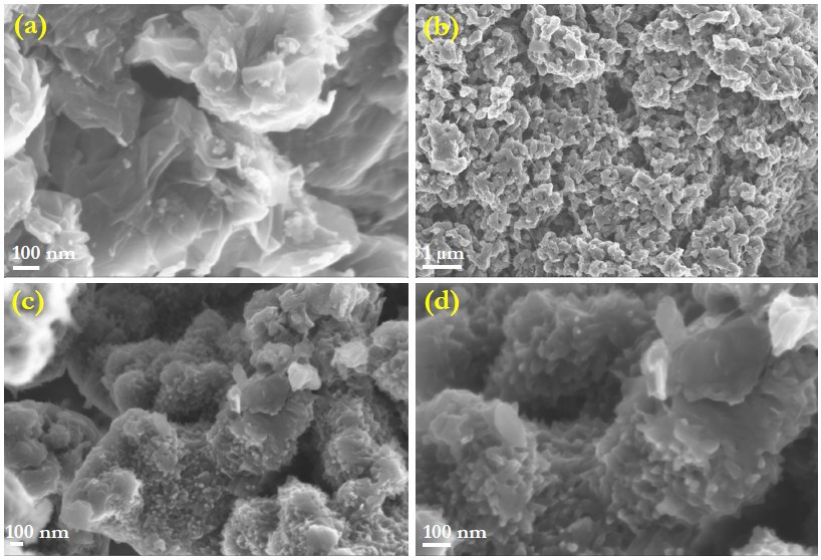

Figure 5.3. FE-SEM images of (a) GO (b) pure PANI and (c-d) PANI-GO composite.

5.3.3 Fourier Transform Infrared Spectroscopy (FTIR) studies

The FTIR spectra of PANI, GO and PANI-GO composite are shown in figure 5.4. The spectrum of GO shows peaks at 1025 cm^{-1}, 1220 cm^{-1} and 1720 cm^{-1} which can be assigned to C-O (alkoxy groups) stretching, C-O (epoxy groups) stretching and C=O stretching respectively.[29] For PANI, the characteristic peaks at 1480 and 1560 cm^{-1} correspond to the benzenoid and quinoid ring vibrations respectively. The peaks at 1292 cm^{-1}, 1111 cm^{-1}, 793 cm^{-1} can be associated with the C-N stretching of the secondary aromatic amine, C-H in-plane bending and C-H out of plane bending vibrations, respectively. These peak positions match well with those reported in the literature.[30] Almost all the characteristic peaks of PANI and GO are observed in the spectrum of the PANI-GO composite.[22]

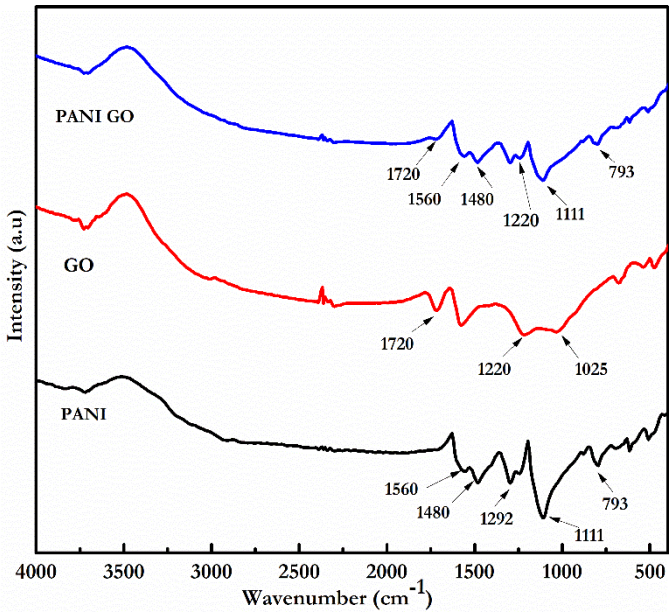

Figure 5.4. FTIR spectra of PANI, GO and PANI-GO composite.

5.3.4 Electrochemical analysis

5.3.4.a Electrochemical impedance spectroscopy (EIS) studies

To estimate the internal resistance and understand the charge transfer kinetics and ion diffusion process of PANI-GO composite, Electrochemical Impedance Spectroscopy (EIS) technique was used. The EIS studies were carried out in the frequency range of 20 kHz to 10 mHz. The Nyquist plots for GO and PANI-GO electrodes are shown in figure 5.5. The Nyquist plot of GO and the equivalent circuit for the plot are shown as inset in the same figure. The symbols R_s, C_{dl}, R_{ct} and CPE in the equivalent circuit represent the series resistance, electrical double layer resistance, charge transfer resistance and constant phase element respectively. The series resistance and charge transfer resistance of the GO electrode are found to be 1.508 Ω and 240 Ω respectively and those of the PANI- GO composite electrode are 0.7441 Ω and

13.5 Ω, respectively. The significant decrease in the value of the charge transfer resistance for PANI- GO electrode is due to the increased surface area of the composite. The improved surface area of the PANI-GO composite offers added area of contact between the electrode and the electrolyte and thus reduces the resistance at the interface. The semicircle portion of the Nyquist plot in the high-frequency region corresponds to the charge transfer resistance at the electrode-electrolyte interface and the straight line portion at low frequencies can be associated with the ion diffusion.[31] On comparison with the GO electrode, the PANI-GO composite electrode shows lower electrode resistance and consequently higher electrical conductivity. The lower resistance of the PANI-GO composite electrode and the possibility of faster ion diffusion as a consequence of the enhanced surface area make the composite material a promising one for supercapacitor applications.

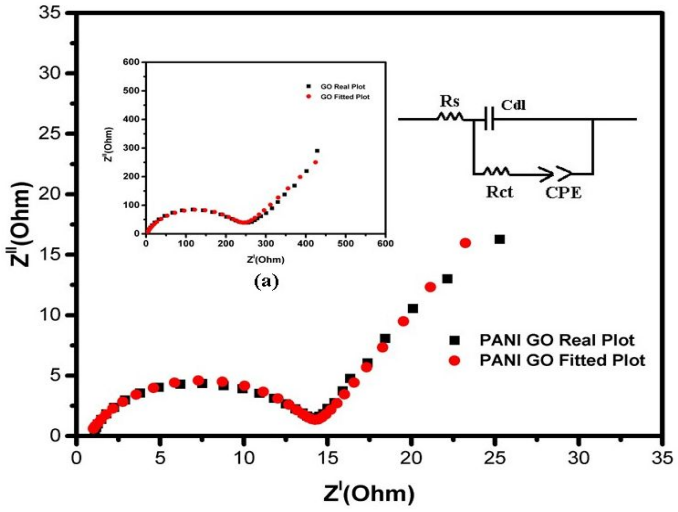

Figure 5.5. Nyquist plots of GO and PANI-GO electrodes in the frequency range of 20 kHz to 10 mHz.

5.3.4.b Three electrode configuration

The cyclic voltammetry (CV) curves of GO and PANI-GO composite at the scan rate of 10 mV s^{-1}, using 1 M solution of lithium perchlorate dissolved in acetonitrile as electrolyte, are shown in figure 5.6. The CV curve of GO is almost rectangular in shape and depicts the typical behavior of EDLC capacitors. On the other hand, the CV curve of PANI-GO composite exhibits redox peaks indicating the pseudo-capacitor behavior of PANI. The CV curve of the composite represents a combination of both the electrochemical double layer capacitance and the pseudo-capacitance. It is clear that the area of the CV curve of the PANI-GO composite is larger than that of GO, thus obviously showing an improved specific capacitance for the composite electrode compared to GO. The CV curves of the PANI-GO composite material at different scan rates are shown in figure 5.7. The curves maintain almost the same shape at different scan rates indicting that the PANI-GO composite electrode material has good rate capability.

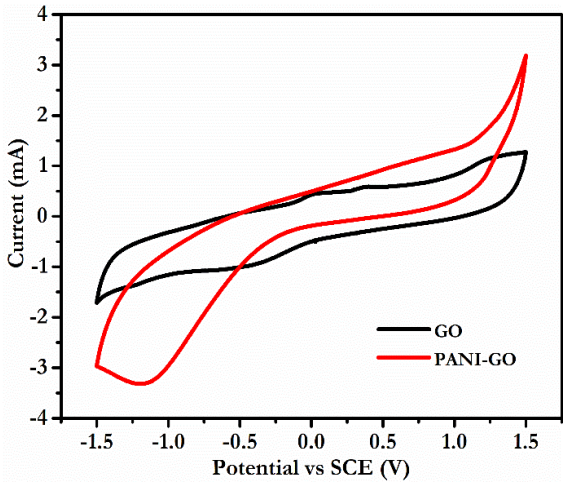

Figure 5.6. CV curves of GO and PANI-GO composite at 10 mV s^{-1}.

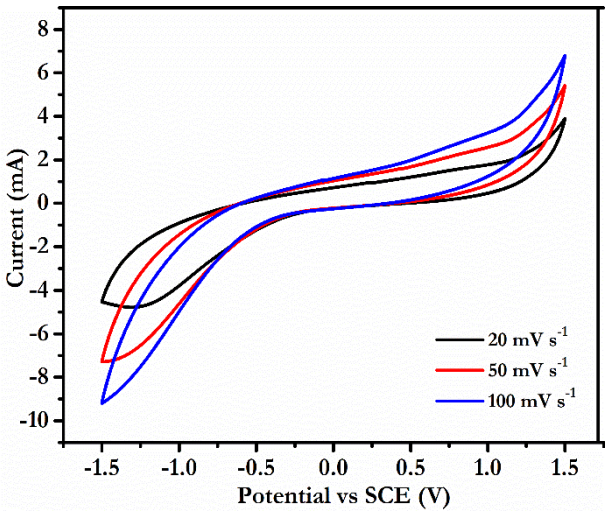

Figure 5.7. CV curves of PANI-GO composite at different scan rates.

Galvanostatic charge-discharge curves (GCD) of the synthesized GO at different current densities varying from 0.2 A g^{-1} to 2 A g^{-1} using 1 M solution of lithium perchlorate dissolved in acetonitrile as the electrolyte are shown in figure 5.8. The specific capacitance can be calculated from the GCD curve using the equation $C = I \times \Delta t/m \times \Delta V$, where I is the applied current for the charge/discharge, Δt is the discharge time, m-the mass of active material in the working electrode and ΔV, the potential window. The mass of active material in the working electrode is 2 mg. The specific capacitance of GO electrode, evaluated from the charge discharge curve is 177 F g^{-1} at a current density of 0.2 A g^{-1}.

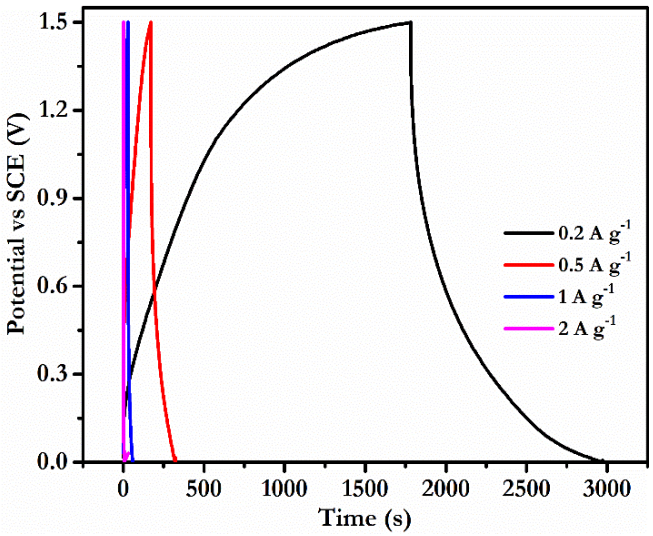

Figure 5.8. GCD curves of GO at various current densities from 0.2 A g^{-1} to 2 A g^{-1}.

The GCD curves of the PANI-GO composite at various current densities from 0.2 A g^{-1} to 2 A g^{-1} are shown in figure 5.9.

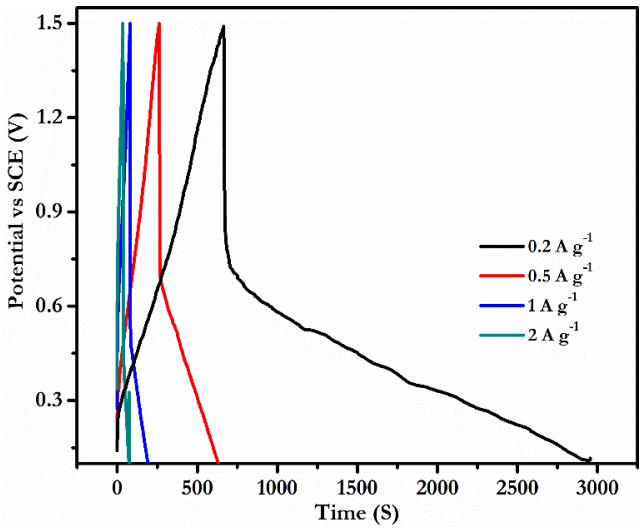

Figure 5.9. GCD curves of PANI-GO composite at various current densities from 0.2 A g^{-1} to 2 A g^{-1}.

The composite shows a stable capacitance of 810 F g^{-1} at a current density of 0.2 A g^{-1} which is much higher than that of the synthesized GO electrode which gives a specific capacitance of 177 F g^{-1} at the same current density. The present value of specific capacitance for the PANI-GO composite is quite a high value, compared to the already reported values for PANI and PANI-GO composites.[19,20,22]

The specific capacitance and the potential window ranging from -1.5 to 1.5 V of the present work are higher than the corresponding values in the previous reports using aqueous electrolytes. The narrow voltage window of aqueous electrolytes makes it difficult for improving the energy and power densities of supercapacitors. As seen in the GCD curve, the discharge time increases with decreasing current density and results in a higher specific capacitance. At lower current densities, there is the probability of more ions diffusing into the electrode material which contributes to the higher specific capacitance. The specific capacitance values of the composite, calculated at different current densities from 0.2 A g^{-1} to 2 A g^{-1} are shown in figure 5.10. It gets reduced to 200 F g^{-1} at a current density of 2 A g^{-1}. The specific capacitance decreases with increase in current density due to the limited diffusivity of ions in the electrolyte at higher currents.[32]

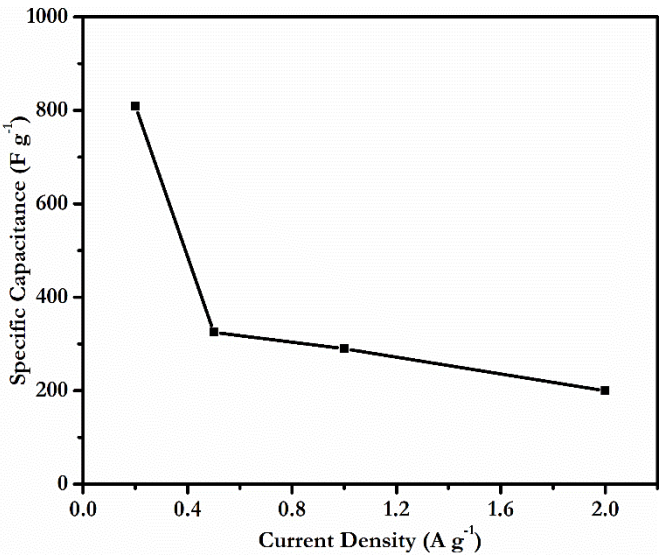

Figure 5.10. Specific capacitance of PANI-GO composite at different current densities from 0.2 A g^{-1} to 2 A g^{-1}.

5.3.4.c Two electrode configuration

For practical applications, the two electrode configuration is more preferred to assess the suitability of a material as the supercapacitor electrode. Supercapacitor test cells were assembled using PANI-GO composite as the electrode active material as explained before and the cells were subjected to GCD studies. The use of organic electrolyte facilitates the operation at a wider voltage window as high as 2.5 V which is an advantage of organic electrolytes over aqueous electrolytes. The GCD measurements were carried out between 0 V and 2.5 V at relatively higher current densities of 3 A g^{-1}, 4 A $g^{-1}$and 5 A g^{-1} using the same electrolyte. The supercapacitor test cells assembled using PANI-GO composite as the electrode show a capacitance of 230 F g^{-1}, 175 F g^{-1} and 132 F g^{-1} at current densities of 3 A g^{-1}, 4 A g^{-1} and 5 A g^{-1} respectively. The charge-discharge curves of the test cells at 5 A g^{-1} for 5

cycles are shown in figure 5.11. The curves are almost symmetric. The specific capacitance of the assembled supercapacitor test cells, calculated from the GCD curves reaches a value of 132 F g^{-1} at a current density of 5 A g^{-1}. The cycling stability of the assembled device, investigated using the GCD test for 1000 cycles is illustrated in figure 5.12. After 1000 cycles, the specific capacitance reaches a value around 112 F g^{-1}. This corresponds to about 84.8 % of the initial capacitance. Although a specific capacitance of 422 F g^{-1} has been reported for the PANI-GO composite based supercapacitors, this value corresponds to a much lower current density of 1 A g^{-1} compared to the present work.[23] Moreover, the PANI-GO composite of the previously reported work is synthesized using covalently functionalized aniline which is a more sophisticated procedure compared to the simple synthesis approach of the present work. For the PANI-GO composite electrode based supercapacitor test cells of the present work, in the comparatively higher voltage window of 0-2.5 V, a specific capacitance of 132 F g^{-1} at a higher current density of 5 A g^{-1} has been achieved. The higher value of the specific capacitance observed in the present work, compared to the previous reports can be attributed to the higher electrical conductivity of the PANI-GO composite, synthesized by the simple in-situ chemical oxidative polymerization method. As per the FE-SEM images, the GO sheets act as templates for the growth of PANI rods, providing enhanced surface area for the composite electrode material. This enhancement in the effective surface area of the composite also contributes towards the high value of the specific capacitance of the PANI-GO based two electrode supercapacitor device.

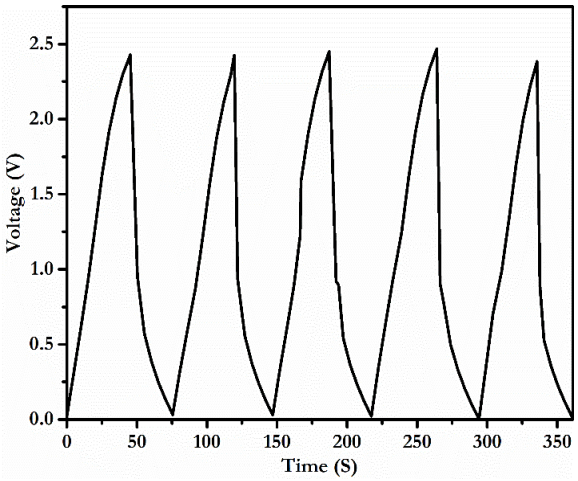

Figure 5.11. GCD curves of PANI-GO composite based supercapacitor test cells at a current density of 5 A g^{-1}.

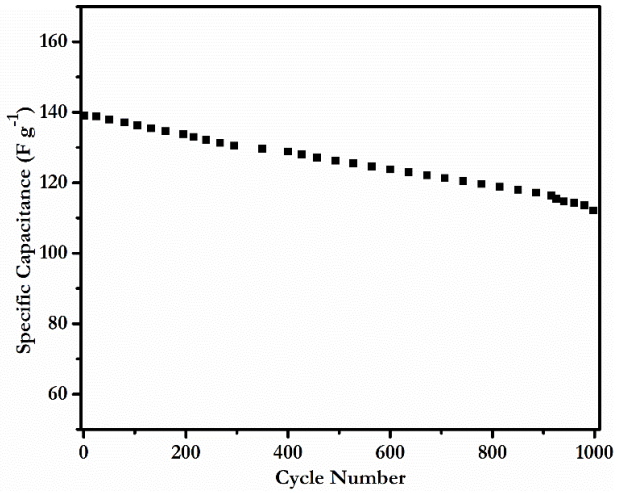

Figure 5.12. Specific capacitance of the assembled PANI-GO based supercapacitor test cells, as a function of cycle number, measured at a current density of 5 A g^{-1}.

5.4 Conclusions

The focal theme of the present work is to assess the suitability of the PANI-GO composite, synthesized by the in-situ oxidative polymerization of aniline, as the electrode material for high power supercapacitor applications. From the electrochemical studies of the PANI-GO electrode using 1 M lithium perchlorate dissolved in acetonitrile as the electrolyte, in three electrode configuration, specific capacitance as high as 810 F g^{-1} at a current density of 0.2 A g^{-1} has been realized. This value of specific capacitance of the present work is much higher than the previously reported values for PANI-GO composite electrodes. The in-situ oxidative polymerization of aniline in the presence of GO facilities the ordered growth of PANI having rod like structure, with the GO sheets acting as the templates for the growth, as evidenced from the FESEM studies. The high value of specific capacitance observed in the present studies is a consequence of the increased surface area of the PANI-GO composite due to the ordered growth of PANI over GO sheets. The CV curves of the PANI-GO composite present a combination of both pseudo-capacitance and electrochemical double layer capacitance. The supercapacitor test cells assembled using PANI-GO composite as the electrode show a specific capacitance of 132 F g^{-1} at a current density of 5 A g^{-1}. The cells are found to have remarkable cycling stability with a retention of 84.8 % of the initial capacity after 1000 cycles. The novelty and highlight of the present work are the observation of capacitance around 810 F g^{-1} for the PANI-GO composite electrode in three electrode configuration which is the highest value being reported for this composite electrode, synthesized using the cost-effective and simple technique of in-situ oxidative polymerization. The capacitance around

132 F g^{-1} at a current density of 5 A g^{-1} obtained for the PANI-GO composite based supercapacitor test cells is also a novel result since the previously reported capacitance values for the supercapacitors based on this composite, correspond to much lower current densities and different synthesis routes and electrolytes. The electrochemical analysis of the PANI-GO composite of the present work both in the three electrode and two electrode configurations, brings out the high application prospects of this composite material in the design of high-power supercapacitors using simple and cost effective synthesis routes.

References

[1] Simon, P.; Gogotsi, Y. Materials for Electrochemical Capacitors. *Nat. Mater.* **2008**, *7*, 845–854.

[2] Lewandowski, A.; Galinski, M. Practical and Theoretical Limits for Electrochemical Double-Layer Capacitors. *J. Power Sources* **2007**, *173*, 822–828.

[3] Bohlen, O.; Kowal, J.; Sauer, D. U. Ageing Behaviour of Electrochemical Double Layer Capacitors. *J. Power Sources* **2007**, *172*, 468–475.

[4] Frackowiak, E. Carbon Materials for Supercapacitor Application. *Phys. Chem. Chem. Phys.* **2007**, *9*, 1774–1785.

[5] Stoller, M. D.; Park, S.; Zhu, Y.; An, J.; Ruoff, R. S. Graphene-Based Ultracapacitors. *Nano Lett.* **2008**, *8*, 3498–3502.

[6] Patake, V. D.; Lokhande, C. D.; Joo, O. S. Electrodeposited Ruthenium Oxide Thin Films for Supercapacitor: Effect of Surface Treatments. *Appl. Surf. Sci.* **2009**, *255*, 4192–4196.

[7] Bae, J.; Song, M. K.; Park, Y. J.; Kim, J. M.; Liu, M.; Wang, Z. L. Fiber Supercapacitors Made of Nanowire-Fiber Hybrid Structures for Wearable/Flexible Energy Storage. *Angew. Chem. Int. Ed. Engl.* **2011**, *50*, 1683–1687.

[8] Saravanakumar, B.; Purushothaman, K. K.; Muralidharan, G. Interconnected V_2O_5 Nanoporous Network for High-Performance Supercapacitors. *ACS Appl. Mater. Interfaces* **2012**, *4*, 4484–4490.

[9] Anilkumar, K.M.; Manoj, M.; Jinisha, B.; Pradeep, V.S.; Jayalekshmi, S. Mn_3O_4 /Reduced Graphene Oxide Nanocomposite Electrodes with Tailored Morphology for High Power Supercapacitor Applications. *Electrochim. Acta* **2017**, *236*, 424–433.

[10] Snook, G. A.; Kao, P.; Best, A. S. Conducting-Polymer-Based Supercapacitor Devices and Electrodes. *J. Power Sources* **2011**, *196*, 1–12.

[11] Wang, K.; Wu, H.; Meng, Y.; Wei, Z. Conducting Polymer Nanowire Arrays for High Performance Supercapacitors. *Small* **2014**, *10*, 14–31.

[12] Zhang, K.; Zhang, L. L.; Zhao, X. S.; Wu, J. Graphene/Polyaniline Nanofiber Composites as Supercapacitor Electrodes. *Chem. Mater.* **2010**, *22*, 1392–1401.

[13] Zhou, Y.; Qin, Z.-Y.; Li, L.; Zhang, Y.; Wei, Y.-L.; Wang, L.-F.; Zhu, M.-F. Polyaniline/Multi-Walled Carbon Nanotube Composites with Core–shell Structures as Supercapacitor Electrode Materials. *Electrochim. Acta* **2010**, *55*, 3904–3908.

[14] Kötz, R.; Carlen, M. Principles and Applications of Electrochemical Capacitors. *Electrochim. Acta* **2000**, *45*, 2483–2498.

[15] Chen, W.-C.; Wen, T.-C. Electrochemical and Capacitive Properties of Polyaniline-Implanted Porous Carbon Electrode for Supercapacitors. *J. Power Sources* **2003**, *117*, 273–282.

[16] Fan, W.; Zhang, C.; Tjiu, W. W.; Pramoda, K. P.; He, C.; Liu, T. Graphene-Wrapped Polyaniline Hollow Spheres as Novel Hybrid Electrode Materials for Supercapacitor Applications. *ACS Appl. Mater. Interfaces* **2013**, *5*, 3382–3391.

[17] Liu, C.; Yu, Z.; Neff, D.; Zhamu, A.; Jang, B. Z. Graphene-Based Supercapacitor with an Ultrahigh Energy Density. *Nano Lett.* **2010**, *10*, 4863–4868.

[18] Shao, Y.; Wang, J.; Wu, H.; Liu, J.; Aksay, I. A.; Lin, Y. Graphene Based Electrochemical Sensors and Biosensors: A Review. *Electroanalysis* **2010**, *22*, 1027–1036.

[19] Wang, H.; Hao, Q.; Yang, X.; Lu, L.; Wang, X. Graphene Oxide Doped Polyaniline for Supercapacitors. *Electrochem. commun.* **2009**, *11*, 1158–1161.

[20] Li, X.; Zhong, Q.; Zhang, X.; Li, T.; Huang, J. In-Situ Polymerization of Polyaniline on the Surface of Graphene Oxide for High Electrochemical Capacitance. *Thin Solid Films* **2015**, *584*, 348–352.

[21] Mitchell, E.; Candler, J.; De Souza, F.; Gupta, R. K.; Gupta, B. K.; Dong, L. F. High Performance Supercapacitor Based on Multilayer of Polyaniline and Graphene Oxide. *Synth. Met.* **2015**, *199*, 214–218.

[22] Gui, D.; Liu, C.; Chen, F.; Liu, J. Preparation of Polyaniline/Graphene Oxide Nanocomposite for the Application of Supercapacitor. *Appl. Surf. Sci.* **2014**, *307*, 172–177.

[23] Li, Z.-F.; Zhang, H.; Liu, Q.; Liu, Y.; Stanciu, L.; Xie, J. Covalently-Grafted Polyaniline on Graphene Oxide Sheets for High Performance Electrochemical Supercapacitors. *Carbon N. Y.* **2014**, *71*, 257–267.

[24] Akbar, F.; Kolahdouz, M.; Larimian, S.; Radfar, B.; Radamson, H. H. Graphene Synthesis, Characterization and Its Applications in Nanophotonics, Nanoelectronics, and Nanosensing. *Journal Mater. Sci. Mater. Electron.* **2015**, *26*, 4347–4379.

[25] Marcano, D. C.; Kosynkin, D. V; Berlin, J. M.; Sinitskii, A.; Sun, Z.; Slesarev, A.; Alemany, L. B.; Lu, W.; Tour, J. M. Improved Synthesis of Graphene Oxide. *ACS Nano* **2010**, *4*, 4806–4814.

[26] Varma, S. J.; Xavier, F.; Varghese, S.; Jayalekshmi, S. Synthesis and Studies of Exceptionally Crystalline Polyaniline Thin Films. *Polym. Int.* **2012**, *61*, 743–748.

[27] Prasanna, G. D.; Prasad, V. B.; Jayanna, H. S. Synthesis, Characterization and Low Temperature Electrical Conductivity of Polyaniline/$NiFe_2O_4$ Nanocomposites. *IOP Conf. Ser. Mater. Sci. Eng.* **2015**, *73*, 012072.

[28] Wang, H.; Hao, Q.; Yang, X.; Lu, L.; Wang, X. Effect of Graphene Oxide on the Properties of Its Composite with Polyaniline. *ACS Appl. Mater. Interfaces* **2010**, *2*, 821–828.

[29] Guo, H.-L.; Wang, X.-F.; Qian, Q.-Y.; Wang, F.-B.; Xia, X.-H. A Green Approach to the Synthesis of Graphene Nanosheets. *ACS Nano* **2009**, *3*, 2653–2659.

[30] Li, L.; Song, H.; Zhang, Q.; Yao, J.; Chen, X. Effect of Compounding Process on the Structure and Electrochemical Properties of Ordered Mesoporous Carbon/Polyaniline Composites as Electrodes for Supercapacitors. *J. Power Sources* **2009**, *187*, 268–274.

[31] Wang, L.; Ye, Y.; Lu, X.; Wen, Z.; Li, Z.; Hou, H.; Song, Y. Hierarchical Nanocomposites of Polyaniline Nanowire Arrays on Reduced Graphene Oxide Sheets for Supercapacitors. *Sci. Rep.* **2013**, *3*, 3568.

[32] Wang, J.-G.; Yang, Y.; Huang, Z.-H.; Kang, F. Interfacial Synthesis of Mesoporous MnO_2/Polyaniline Hollow Spheres and Their Application in Electrochemical Capacitors. *J. Power Sources* **2012**, *204*, 236–243.

6

Realizing Li-ion full cells with $LiFePO_4$ cathode and Mn_3O_4-mesoporous carbon composite anode for energy storage applications

This chapter deals with the attempts carried out to assemble and characterize the lithium ion full cells using Mn_3O_4-mesoporous carbon (MnMC) composite anode and $LiFePO_4$ cathode (LFP) for applications in energy storage. As explained in the second chapter, the MnMC nanocomposite is obtained by simple physical mixing of the components. The cathode material, LFP is synthesized via sol-gel method. The structural and morphological details of LFP cathode are investigated using X-ray diffraction (XRD) and field emission scanning electron microscopy (FE-SEM) techniques and the electrochemical performance is evaluated by assembling half cells with lithium metal as the counter electrode. The MnMC nanocomposite is pre-lithiated and combined with LFP cathode for the full lithium ion cell with a cathode limiting capacity. The LFP-MnMC full cells exhibit reversible capacity of the LFP cathode and show good cycling stability with a capacity retention of 66% and the average Coulombic efficiency is found to be 98% after 100 cycles.

6.1 Introduction

The lithium ion batteries (LIBs) based energy storage systems are explored to go beyond powering portable electronic devices including mobile phones and laptops to large scale applications in hybrid electric vehicles and electrical energy storage systems for the efficient utilization of renewable energy sources.[1–3] There is a huge urge for developing LIBs with high energy density, long cycle life and improved safety features. The possibility of replacing the conventional graphitic anode by transition metal oxides owing to their high conversion capacity, low-cost, earth abundance and non-toxic nature is being extensively pursued and one of the most promising transition metal oxides, Mn_3O_4 has been studied in detail as outlined in the second chapter. The inherent limitations that hinder the implementation of Mn_3O_4 are relieved by making the nanocomposite of Mn_3O_4 with mesoporous carbon (MC), which has been identified as an excellent alternative for conventional graphitic anode in LIBs.[4,5] For the practical realization of anode materials, it would be highly desirable to examine the electrochemical responses in a full cell configuration with specific cathodes.[6–8]

When LIBs were commercialized for the first time, $LiCoO_2$ was the primary choice as the cathode material. Over the course of time, different cathode materials including $LiMn_2O_4$, $LiNiO_2$ and $LiFePO_4$ were identified as promising alternatives for the more expensive and toxic material, $LiCoO_2$. The non- toxic nature, high thermal stability, high theoretical capacity of 170 mA h g^{-1} and the comparatively low material cost make the iron based, $LiFePO_4$, superior to other cathode materials. The structural stability during Li ion transport and the long voltage platform make it a promising candidate as the cathode

electrode.[9–11] The $LiFePO_4$ sample obtained by solid-state reaction method usually has large particle size and poor particle size distribution. The large grain size of $LiFePO_4$ causes reduced lithium ion diffusion and leads to poor rate capability. The synthesis technique, suitable for achieving smaller grain size preferably in the nanometer range should be adopted for the enhancing the rate capability performance of $LiFePO_4$. In the present work, sol-gel method is used to synthesize $LiFePO_4$ particles with well controlled size and high purity[12–14] and Li-ion full cell configuration (LFP-MnMC) is investigated with the formerly explored MnMC nanocomposite as anode and $LiFePO_4$ synthesized by sol-gel method as the cathode with a cathode limiting capacity.[15,16] It is expected that this cost-effective, eco-friendly and reliable, LFP-MnMC based full cell configuration will be an attractive aspirant for various applications.

6.2 Experimental

6.2.1 Materials

Lithium nitrate, ferrous oxalate dihydrate, ammonium dihydrogen phosphate, citric acid and nitric acid of analytical grade were purchased from Alpha Chemicals, India. All the synthesis procedures were carried out using distilled water.

6.2.2 Synthesis of $LiFePO_4$

The sol-gel method used to synthesize LFP is outlined: The precursors, ferrous oxalate dihydrate and lithium nitrate were dissolved in 1 M nitric acid solution in stoichiometric amounts into which 20 ml citric acid solution (1 M) was added drop wise with continuous stirring.

A saturated solution of ammonium dihydrogen phosphate was added to the above solution followed by continuous stirring at 50 °C for 4 hours to obtain the mixture in gel form. The gel precursor was dried at 80 °C for a week in an oven and then fired at 700 °C under continuous argon flow for two hours. The citric acid functions as a carbon source and provides the network structure of carbon for electron conduction by preventing the oxidation of ferrous ions to the ferric state. The schematic representation of the synthesis procedure of the LFP cathode is shown in figure 6.1.

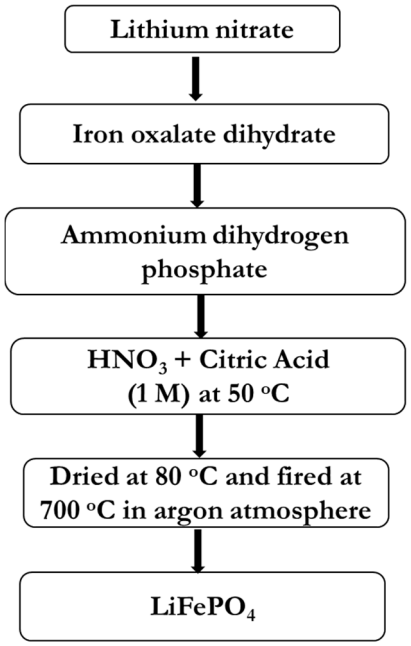

Figure 6.1. The schematic representation of the synthesis of $LiFePO_4$ cathode.

6.2.3 Synthesis of Mn_3O_4-mesoporous carbon (MnMC) nanocomposite

The MnMC nanocomposite obtained by physical mixing of the components as explained earlier (section 2.2) was used as the anode material in full cell configuration.

6.2.4 Pre-lithiation of MnMC based composite anode

During the first cycles of Li-ion cells, certain amount of active lithium loss occurs due to electrolyte decomposition and the formation of solid electrolyte interphase (SEI) layer at the anode surface. To overcome this issue, certain amount of active lithium is stored in the anode electrode by pre-lithiation prior to charge-discharge cycling. This compensates the loss of lithium ions and leads to an increased lithium content after the first cycle, resulting in increased reversible specific capacity and higher energy density. There are different types of techniques for pre-lithiation, which include chemical and electrochemical pre-lithiation, pre-lithiation with the help of electrode additives Li_5FeO_4 and Li_5ReO_6, pre-lithiation with lithium silicide inside the anode containing lithium metal electrode and pre-lithiation by direct contact of the anode and lithium metal.[17–20]

The MnMC nanocomposite anode was pre-lithiated by keeping it in direct contact with lithium metal for 6 hours inside the argon filled glove box, in which the moisture levels are controlled to be less than 1 ppm. The electrolyte used was 1 M solution of $LiPF_6$ in a 1:1 mixture of ethylene carbonate (EC) and dimethyl carbonate (DMC). The potential difference between lithium metal and the electrode material leads to the flow of electrons. Electrons from the lithium metal flow

into the MnMC electrode material and the charge neutrality is maintained by the insertion of the lithium ions of the electrolyte into the electrode material.

The schematic illustration of the pre-lithiation process by direct contact to lithium metal is shown in figure 6.2. The pre-lithiation of the MnMC anode electrode was carried out inside the argon-filled glovebox and once it was completed, the lithium metal foil was removed prior to cell assembly.

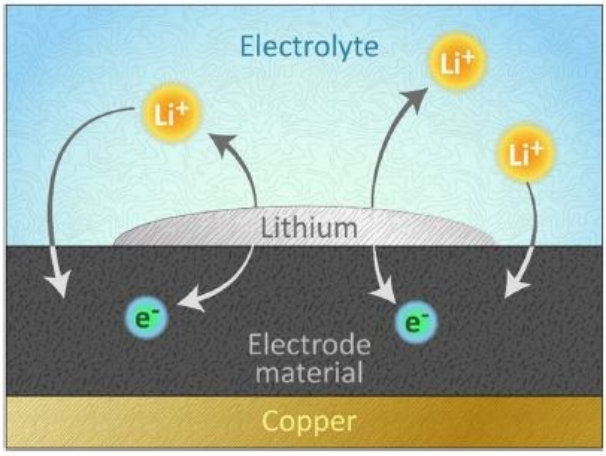

Figure 6.2. Schematic illustration of the pre-lithiation process of the anode material by direct contact to lithium metal.

6.2.5 Structural and morphological characterization

The structural characterization of the synthesized LFP was carried out by X-ray diffraction technique (XRD) employing the PANalytical's X'Pert Pro machine with Cu-Kα radiation of wavelength 1.542 Å. The surface morphological features of the LFP were studied using the Carl Zeiss Sigma, field emission scanning electron microscope (FE-SEM).

6.2.6 Electrochemical studies

The LFP cathode electrodes were made by mixing 80 wt.% of the active material LFP, 10 wt.% of acetylene black as the conducting medium and 10 wt.% of polyvinylidene difluoride (PVDF) in N-methyl-2-pyrrolidone (NMP) solvent as the binder to make a slurry. The slurry was coated on aluminum foil by spray coating and dried at 120°C under vacuum for overnight. The electrochemical behavior of the LFP cathode was investigated by assembling lithium half cells with pure lithium metal as the counter electrode and LFP as the working electrode in an argon-filled glove box. The electrochemical studies of the MnMC anode electrode in half cell configuration are discussed in the second chapter. For the full cell, the pre-lithiated MnMC nanocomposite was used as the anode, LFP as the cathode and Celgard as the separator. The electrolyte used for the half cell and full cell configurations was 1 M solution of $LiPF_6$ in a 1:1 mixture of ethylene carbonate (EC) and dimethyl carbonate (DMC). The active material loading was 1.5 mg for the MnMC composite anode and 2.5 mg for LFP cathode. The cyclic voltammetry (CV) and galvanostatic charge-discharge studies (GCD) of the assembled LFP cathode based half cells and LFP-MnMC based full cells were carried out using the Bio-Logic SP300 workstation and 8 channel battery analyzer (MTI Corporation-USA), respectively.

6.3 Results and discussion

The structural and morphological characterization of the MnMC nanocomposite is already discussed in the second chapter.

6.3.1 X-ray diffraction (XRD) analysis

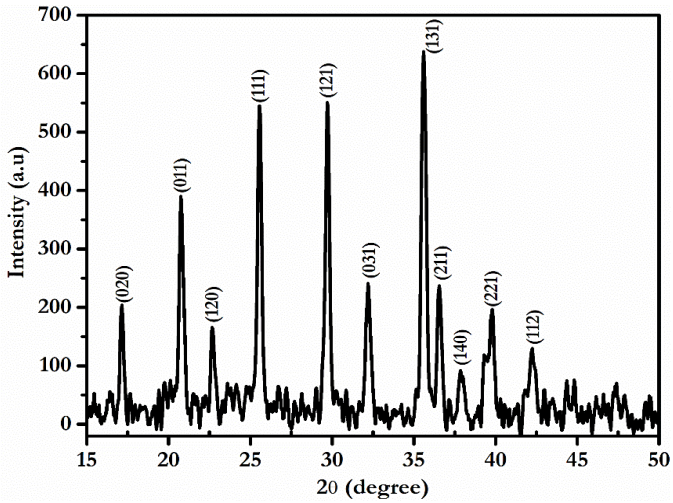

Figure 6.3. XRD pattern of $LiFePO_4$.

The XRD pattern of LFP is shown in figure 6.3. The pattern shows all the characteristic peaks of LFP, which can be assigned to the to the orthorhombic phase $LiFePO_4$ without any impurity.[21] The narrow and symmetric reflection peaks indicate the high crystallinity of the LFP sample obtained by sol-gel synthesis technique.

6.3.2 Field Emission Scanning Electron Microscopy (FE-SEM) analysis

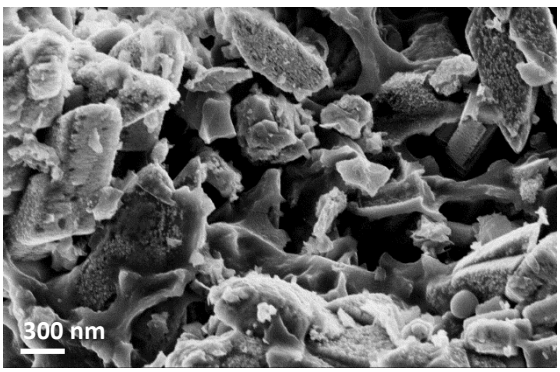

Figure 6.4. FE-SEM image of $LiFePO_4$.

The FE-SEM image of $LiFePO_4$ particles obtained by sol-gel method is shown in figure 6.4. The image shows the irregular morphology of $LiFePO_4$ particles with size less than 100 nm with least agglomeration.

6.3.3 Electrochemical analysis

6.3.3.a Anode material

The cyclic voltammetry, charge- discharge cycling and the rate capability studies of the MnMC nanocomposite anode are detailed in the second chapter. The composite anode is found to exhibit remarkable performance to be considered as a prospective anode electrode for high energy density Li-ion cells.

6.3.3.b $LiFePO_4$ cathode material

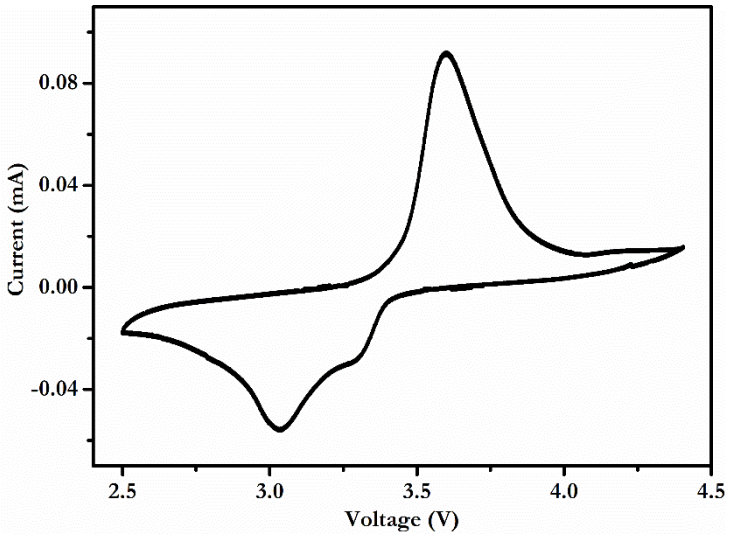

Figure 6.5. CV curve of $LiFePO_4$ in the voltage range of 2.5-4.5 V at a scan rate of 0.1 mV s^{-1}.

The cyclic voltammetry curve of LFP in the voltage range 2.5–4.5 V at a scan rate of 0.1 mV s^{-1} is shown in figure 6.5. The curve shows two peaks, the anodic peak at 3.5 V and the cathodic peak at 3 V. During the anodic sweep, lithium ions are extracted from the LFP structure due to the oxidation of Fe^{2+} to Fe^{3+} and during the cathodic sweep, lithium insertion into the LFP structure occurs due to the reduction of Fe^{3+} to Fe^{2+}. No additional peaks are observed and the well-defined peaks indicate good electrochemical reactivity of LPF and high lithium ion diffusion rate.[22,23]

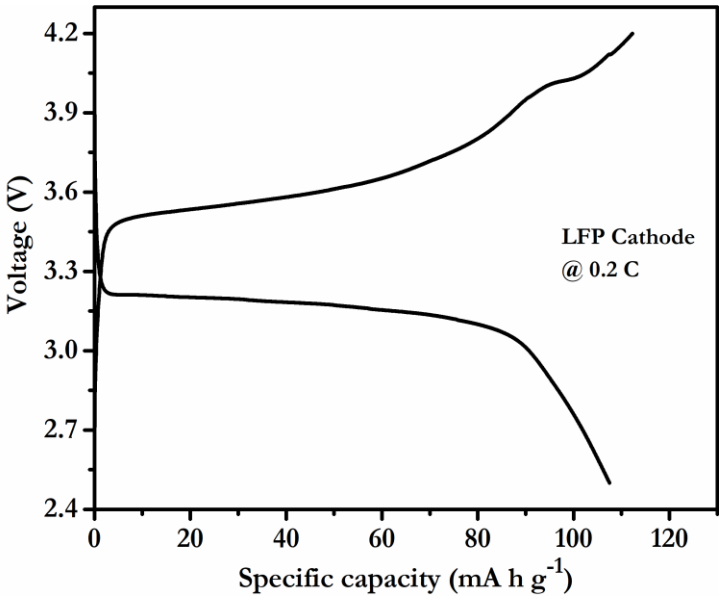

Figure 6.6. Charge-discharge profile of $LiFePO_4$ at 0.2 C.

The initial charge–discharge cycle of LFP cathode cycled between 2.5 V and 4.5 V at 0.2 C (1 C=170 mA g^{-1}) is depicted in figure 6.6. The voltage plateau observed in the profile corresponds to the oxidation/reduction reactions of Fe^{3+}/Fe^{2+} redox couple, which is in

agreement with the CV profile. The LFP cathode exhibits charge, discharge capacities of 112 mA h g^{-1} and 107 mA h g^{-1}, respectively corresponding to the Coulombic efficiency of 97%.

6.3.3.c Li-ion full cell: Charge-discharge and cycling performance studies

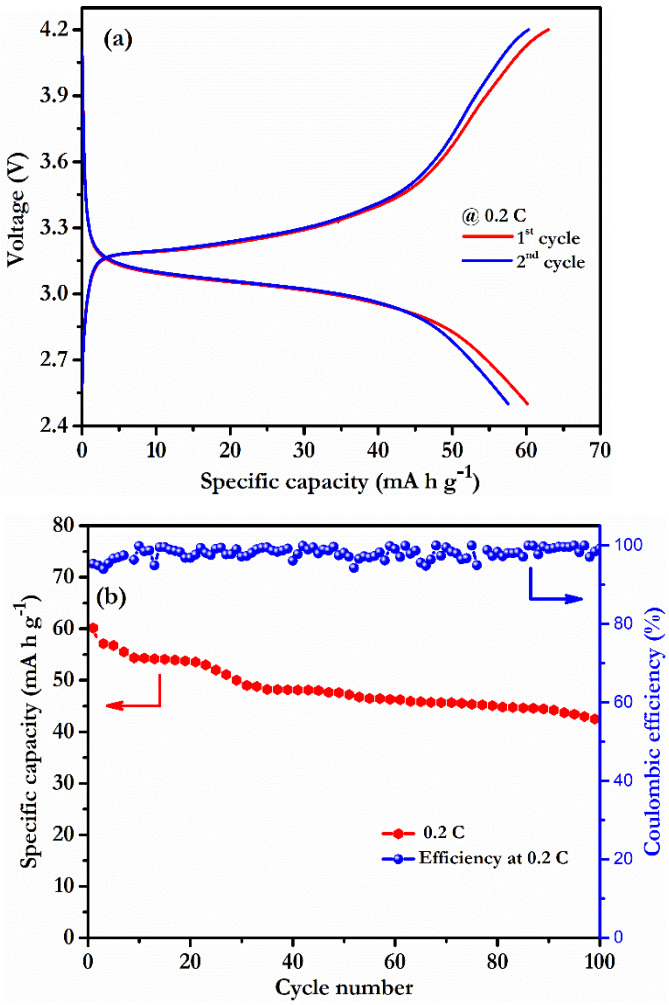

Figure 6.7. (a) Charge-discharge profile of the assembled full cell at 0.2 C (b) Cycling performance and Coulombic efficiency of the full cell at 0.2 C.

The initial two charge-discharge profiles of the LFP-MnMC based, full cell cycled between 2.5 V and 4.2 V at 0.2 C rate are shown in figure 6.7a. The full cell delivers an initial discharge capacity of 63 mA h g^{-1} at 0.2 C. The cycling performance of the full cell at 0.2 C for 100 cycles and the corresponding Coulombic efficiency are shown in figure 6.7b. The discharge capacity gradually fades during the initial stage and then remains almost constant. A discharge capacity of 42 mA h g^{-1} is observed at the end of the 100^{th} cycle with a capacity retention of 66% and the average Coulombic efficiency during the cycling is found to be 98%. The full cell displays lower capacity values compared to both the anode and cathode half cells due to the lower ionic and electronic conductivity of the anode and cathode materials of the full cell compared to lithium metal used as the counter electrode in half cells. The electrochemical behaviour exhibited by the full cell during the initial studies are encouraging and proper optimization of the synthesis conditions of the cathode material are needed to achieve the desired electronic conductivity and ionic transport properties to develop the present full cell configuration as a reliable lithium cell, potentially offering low cost, high capacity and rate capability, and excellent safety features.

6.4 Conclusions

The practical realization of lithium ion full cell has been attempted using MnMC nanocomposite as the anode and LFP as the cathode. The MnMC nanocomposite is pre-lithiated to compensate for the irreversible capacity and the electrochemical properties of the LFP cathode synthesized by sol-gel method are investigated in a half cell configuration with lithium metal as the reference electrode prior to the assembly of full cell. The pre-lithiated MnMC nanocomposite is used as

the anode and the synthesized LFP as the cathode for the lithium ion full cell with a cathode limiting capacity. The LFP-MnMC based full cell delivers an initial discharge capacity of 63 mA h g^{-1} at 0.2 C and good cycling stability over 100 charge discharge cycles. More studies are needed on the optimized synthesis conditions of the cathode material and the cell design to develop the LFP-MnMC based full cell configuration into a reliable Li-ion cell.

References

[1] Taberna, P. L.; , S.Mitra , P.Poizot, P. S. J.-M. T. High Rate Capabilities Fe_3O_4-Based Cu Nano-Architectured Electrodes for Lithium-Ion Battery Applications. *Nat. Mater.* **2006**, *5*, 567–573.

[2] Nitta, N.; Wu, F.; Lee, J. T.; Yushin, G. Li-Ion Battery Materials : Present and Future. *Mater. Today* **2015**, *18*, 252–264.

[3] Scrosati, B.; Garche, J. Lithium Batteries : Status, Prospects and Future. *J. Power Sources* **2010**, *195*, 2419–2430.

[4] Deng, Y.; Wan, L.; Xie, Y.; Chen, G. Recent Advances in Mn-Based Oxides as Anode Materials for Lithium Ion Batteries. *RSC Adv.* **2014**, *4*, 23914–23935.

[5] Goriparti, S.; Miele, E.; De Angelis, F.; Fabrizio, E. Di; Zaccaria, R. P.; Capiglia, C. Review on Recent Progress of Nanostructured Anode Materials for Li-Ion Batteries. *J. Power Sources* **2014**, *257*, 421–443.

[6] Hassoun, B. J.; Panero, S.; Reale, P.; Scrosati, B. A New , Safe , High-Rate and High-Energy Polymer Lithium-Ion Battery. *Adv. Mater.* **2009**, *21*, 4807–4810.

[7] Imazaki, M.; Ariyoshi, K.; Ohzuku, T. An Approach to 12 V "Lead-Free "Batteries : Tolerance toward Overcharge of 2.5 V Battery Consisting of LTO and LAMO. *J. Electrochem. Soc.* **2009**, *156*, 780–786.

[8] Hassoun, J.; Lee, K.; Sun, Y.; Scrosati, B. An Advanced Lithium Ion Battery Based on High Performance Electrode Materials. *J. Am. Chem. Soc.* **2011**, *133*, 3139–3143.

[9] Wu, B.; Ren, Y.; Li, N. $LiFePO_4$ Cathode Material. In *Electric Vehicles – The Benefits and Barriers*; **2011**.

[10] Yuan, L.; Wang, Z.; Zhang, W.; Hu, X.; Chen, J.; Huang, Y. Development and Challenges of $LiFePO_4$ Cathode Material for Lithium-Ion Batteries. *Energy Environ. Sci.* **2011**, *4*, 269–284.

[11] Sun, C. S.; Zhou, Z.; Xu, Z. G.; Wang, D. G.; Wei, J. P.; Bian, X. K.; Yan, J. Improved High-Rate Charge/Discharge Performances of $LiFePO_4$/C via V-Doping. *J. Power Sources* **2009**, *193*, 841–845.

[12] Yang, Z.; Wang, S. High Cycling Performance Cathode Material : Interconnected $LiFePO_4$/Carbon High Cycling Performance Cathode Material : Interconnected $LiFePO_4$/Carbon Nanoparticles Fabricated by Sol-Gel Method. *J. Nanomater.* **2014**, *2014*, 801562.

[13] Hu, Y.; Doeff, M. M.; Kostecki, R.; Fin, R. Electrochemical Performance of Sol-Gel Synthesized $LiFePO_4$ in Lithium Batteries. *J. Electrochem. Soc.* **2004**, *151*, 1279–1285.

[14] Hsu, K.; Tsay, S.; Hwang, B. Synthesis and Characterization of Nano-Sized $LiFePO_4$ Cathode Materials Prepared by a Citric Acid-Based Sol – Gel Route. *J. Mater. Chem.* **2004**, *14*, 2690–2695.

[15] Hassoun, J.; Croce, F.; Hong, I.; Scrosati, B. Lithium-Iron Battery : Fe_2O_3 Anode versus $LiFePO_4$ Cathode. *Electrochem. commun.* **2011**, *13*, 228–231.

[16] Brutti, S.; Hassoun, J.; Scrosati, B.; Lin, C.; Wu, H.; Hsieh, H. A High Power Sn-C/C-$LiFePO_4$ Lithium Ion Battery. *J. Power Sources* **2012**, *217*, 72–76.

[17] Jarvis, C. R.; Lain, M. J.; Yakovleva, M. V; Gao, Y. A Prelithiated Carbon Anode for Lithium-Ion Battery Applications. *J. Power Sources* **2006**, *162*, 800–802.

[18] Holtstiege, F.; Schmuch, R.; Winter, M.; Brunklaus, G.; Placke, T. New Insights into Pre-Lithiation Kinetics of Graphite Anodes via Nuclear Magnetic Resonance Spectroscopy. *J. Power Sources* **2018**, *378*, 522–526.

[19] Holtstiege, F.; Bärmann, P.; Nölle, R.; Winter, M.; Placke, T. Pre-Lithiation Strategies for Rechargeable Energy Storage Technologies : Concepts, Promises and Challenges. *Batteries* **2018**, *4*, 1–39.

[20] Chevrier, V. L.; Liu, L.; Wohl, R.; Chandrasoma, A.; Vega, J. A.; Eberman, K. W.; Stegmaier, P.; Figgemeier, E.; Hampshire, N. Design and Testing of Prelithiated Full Cells with High Silicon Content. *J. Electrochem. Soc.* **2018**, *165*, 1129–1136.

[21] Yu, F.; Zhang, J.; Yang, Y.; Song, G. Up-Scalable Synthesis, Structure and Charge Storage Properties of Porous Microspheres of $LiFePO_4$@C Nanocomposites. *J. Mater. Chem.* **2009**, *4*, 9121–9125.

[22] Zhang, X.; Aravindan, V.; Kumar, P. S.; Liu, H.; Sundaramurthy, J.; Ramakrishna, S.; Madhavi, S. Synthesis of TiO_2 Hollow Nanofibers by Co-Axial Electrospinning and Its Superior Lithium Storage Capability in Full-Cell Assembly with Olivine Phosphate†. *Nanoscale* **2013**, *5*, 5973–5980.

[23] Rajoba, S. J.; Jadhav, L. D.; Kalubarme, R. S.; Patil, P. S.; Varma, S.; Wani, B. N. Electrochemical Performance of $LiFePO_4$/GO Composite for Li-Ion Batteries. *Ceram. Int.* **2018**, *44*, 6886–6893.

7

Conclusions and future outlook

The main focus of the present study is to establish the versatile role of carbonaceous materials in the development of various energy storage systems. The overall summary of the research work carried out is outlined in this chapter, emphasizing the important conclusions drawn from the current investigations. Major achievements of the present study and the scope for future investigations are also highlighted.

7.1 Conclusions

With the enormous increase in energy consumption triggered by the developments in the living standards of the society and the problem of fast depletion of the fossil fuel based energy sources, there have been extensive efforts for harvesting the energy from the sun and the wind. Since these renewable energy sources are intermittent, stable and efficient energy storage systems are mandatory to store the generated energy and release it upon demand. Rechargeable lithium batteries and supercapacitors constitute the most important energy storage devices in terms of efficiency, energy density, power density and long-term cycling stability. In the present Ph.D. thesis, the various strategies and material architectures adopted on different carbonaceous materials to identify the best breed of materials for developing novel and sustainable energy

storage devices are presented. The energy storage devices investigated in the present study include lithium-ion cells (Li-ion), lithium-sulfur (Li-S) cells and supercapacitors. It is also important to note that the novel storage systems developed should be reliable and biocompatible to visualize the ideology of green energy.

As lithium-ion cells have found applications beyond portable electronic devices, the possibility of replacing the graphitic anode by the transition metal oxide, Mn_3O_4 based nanocomposite, to achieve higher capacity and energy density has been pursued and the detailed study is described in the second chapter of the thesis. As pristine Mn_3O_4 faces several issues hindering its practical application as anode in Li-ion cells, the nanocomposite of Mn_3O_4 with mesoporous carbon, MnMC obtained by simple physical mixing method is examined as the anode material. The structural and morphological studies of the MnMC nanocomposite confirm the composite formation and improvement in the structural features of Mn_3O_4 by the presence of mesoporous carbon. The assembled lithium-ion cells with MnMC as the anode deliver an initial discharge capacity of 1601 mA h g^{-1} at a current density of 100 mA g^{-1} and after 100 cycles a discharge capacity of 730 mA h g^{-1} is maintained. The MnMC anode also exhibits excellent rate capability performance and even at a current density of 2000 mA g^{-1} a discharge capacity of 378 mA h g^{-1} has been observed.

Although lithium-ion cells have revolutionized the modern technological society, even the most advanced Li-ion technology cannot fulfill the growing needs for hybrid electric vehicles and large-scale grids which require long operation duration, high storage capacity and long

term stability. New electrochemical storage systems having different reaction mechanisms are expected to go beyond lithium-ion technology. The lithium-sulfur (Li-S) cells are considered as the most promising successors for lithium-ion cells and are widely recognized as the next generation storage devices. However, the commercialization of Li-S technology is hampered by its limitations due to the insulating nature of sulfur cathode, the volume expansion of sulfur during Li intake and the polysulfide shuttle effect. The next two chapters of the thesis are focused on overcoming the above-mentioned limitations of the Li-S technology, which prevent it from becoming a superior battery technology. In the first section, bio-mass derived, steam activated and acid washed carbon (AC) is used to effect surface modification of the sulfur cathode, by making composite with sulfur, termed as the ACS composite. A novel cell configuration is attempted by placing a flexible film of acid functionalized, multi walled carbon nanotubes, termed as the CNTF interlayer, between the modified sulfur cathode (ACS) and the separator to hinder the polysulfide shuttle effect and to improve the overall electrical conductivity of the cathode assembly. The porous nature of the activated carbon (AC) helps in controlling the volume expansion of the sulfur cathode during Li intake. The electrochemical studies show that with the CNTF interlayer, the assembled Li-S cells deliver an initial discharge capacity of 1562 mA h g^{-1} at 0.05 C rate and retain 71% of the initial capacity at 1 C rate after 200 cycles. The next section of the work on Li-S cells establishes the fruitful role of the highly conducting, polyaniline (PANI) coated mesoporous carbon (MC), obtained by in-situ polymerization method, in modifying the sulfur cathode by making the composite with sulfur, termed as SPMC. The

Li-S cells assembled with the SPMC composite cathode having a sulfur content of 80 wt%, together with the flexible interlayer of carbon nanotubes exhibit an initial discharge capacity of 1137 mA h g^{-1} at 0.2 C rate. Furthermore, at 1 C rate the cells deliver a discharge capacity of 968 mA h g^{-1} at the initial cycle and 700 mA h g^{-1} after 200 cycles corresponding to an extremely low capacity decay of 0.14% per cycle. The presence of polyaniline is quite effective in controlling the volume expansion of sulfur during Li intake and the SPMC-CNT interlayer combination is a superb cathode assembly design to achieve excellent capacity retention at higher C rates. The detailed electrochemical studies conducted on the two types of Li-S cells are quite promising and open new vistas in the pursuit towards realizing Li-S cells with impressive performance characteristics for the next generation energy storage applications.

Supercapacitors positioned between capacitors and batteries can store more energy than conventional capacitors. They can be charged quickly, turned on instantaneously, and are endowed with high power density and cycling stability suitable for applications in hybrid electric vehicles and energy harvesting. The fifth chapter of the thesis deals with the studies conducted on polyaniline (PANI)-graphene oxide (GO) based nanocomposite electrodes for developing high quality supercapacitors. The PANI-GO nanocomposite electrode tested in three electrode configuration shows specific capacitance of 810 F g^{-1} at a current density of 0.2 A g^{-1}, which is the highest value reported for PANI-GO composite electrode in three electrode structure. At the device level, in two electrode configuration, the performance of the hybrid supercapacitor is evaluated by carrying out electrochemical studies on the assembled

supercapacitor test cells, which show high specific capacitance of 132 F g^{-1} at a high current density of 5 A g^{-1} with good capacity retention over 1000 cycles.

The practical implementation of a novel, low-cost, environmentally benign full lithium-ion cell based on lithium iron phosphate (LFP) as the cathode and Mn_3O_4-mesoporous carbon (MnMC) nanocomposite, as the anode has been attempted as the final part of the work and the details are given in chapter six of the thesis. The nanostructured LFP cathode is synthesized by sol-gel method and has the advantages of high theoretical capacity, high stability and low cost. The LFP cathode when investigated in the half cell configuration exhibits charge discharge capacities of 112 mA h g^{-1} and 107 mA h g^{-1}, respectively. The LFP-MnMC based full cells with pre-lithaited MnMC composite anode and LFP cathode deliver an initial discharge capacity of 63 mA h g^{-1} at 0.2 C and good cycling stability over 100 charge discharge cycles. The initial studies on the Li-ion full cells are quite promising and although the discharge capacity is low, there is ample scope for improving the capacity substantially by optimizing the synthesis conditions of the LFP cathode.

7.2 Future outlook

The innovative research work included in the thesis highlights the different approaches adopted to employ various carbonaceous materials for the next generation energy storage device applications. The impressive performance characteristics of the investigated carbon materials provide plenty of scope for further investigations in energy related applications. More optimization and innovations in the synthesis techniques can be made to tailor the properties of these carbon materials in the designing

of electrodes for high energy density and power density devices. The future perspective of research will be focused on the following phases.

- Advances in synthesis process, material architecture and cell designing for improving the energy storage properties.
- Optimization of various parameters for the development of the next generation Li-S full cells with suitable anode materials.
- Realization of $LiFePO_4$ -Mn_3O_4-MC based Li-ion full cells meeting commercial standards.